Developing water isotope records from stratigraphically disturbed blue ice: observations, limitations, and insights from the Allan Hills of Antarctica

Lindsey Davidge

A dissertation

submitted in partial fulfillment of the

requirements for the degree of

Doctor of Philosophy

University of Washington

2025

Reading Committee:

Eric J. Steig, Chair

T.J. Fudge

Ed Waddington

Program Authorized to Offer Degree:

Department of Earth and Space Sciences

University of Washington

Abstract

Developing water isotope records from stratigraphically disturbed blue ice: observations, limitations, and insights from the Allan Hills of Antarctica

Lindsey Davidge

Chair of the Supervisory Committee:
Eric J. Steig
Department of Earth and Space Sciences

Polar ice cores contain direct archives of past atmosphere and past precipitation, and water-isotope measurements of polar ice-core samples are used to reconstruct Earth's past climate. Ice cores from stable domes or ice divides – where post-depositional ice flow results primarily from compression of more recently accumulated snowfall – have produced continuous climate records as old as 800 ka. Climate records from older ice cores are of interest due to a notable change in Earth's climatic fluctuations around 1 Ma. Extending the ice-core paleoclimate record beyond 1 Ma likely requires measurements from more complicated depositional environments, such as from blue ice areas at the margins at the Antarctic ice sheet. The Allan Hills blue-ice area contains ice as old as 6 Ma at relatively shallow depths (<200 m below the surface), but cores from this region are typically discontinuous and stratigraphically disturbed. In addition, they have likely experienced orders of magnitude more thinning than more typical ice cores, severely limiting their temporal resolution.

The development and interpretation of ice-core climate records from blue-ice areas is still in nascent stages, and is only possible due to the development of an absolute dating technique by the analysis of atmospheric ^{40}Ar (Bender et al., 2008). Age constraints at discrete depths along the core provide information about the average age of the ice, but significant uncertainty remains about the amount of time represented by each measurement. Here, I

present new water-isotope records from discontinuous blue-ice cores from the Allan Hills blue ice area of Antarctica, and explore the implications and limitations of those data. This thesis uses high-resolution water-isotope data to explore the integrated history of ice recovered from the Allan Hills. This thesis (1) details advancements in high-resolution water-isotope measurement methodology by continuous-flow analysis, which is the preferred method for analyzing many Allan Hills cores, (2) advances our understanding of water-isotope signal preservation and alteration in blue ice by examining the reproducibility of the water-isotope record at lateral distances of 0.22 to 140 m, (3) demonstrates that climate signals are preserved in some disturbed Allan Hills ice and provides insights into ice accumulation and climate history in this area, and (4) explores differences in water-isotope distillation pathways caused by atmosphere and ocean changes between the present-day and a warmer (i.e. 6-Ma) world.

TABLE OF CONTENTS

ACKNOWLEDGMENTS

I am grateful for the professional, personal, and financial support I have received during my time at the University of Washington. Many thanks to my advisor, Eric Steig, for his mentorship and support throughout my academic journey. Thanks to my committee – including T.J. Fudge, Ed Waddington, Peter Blossey, and Jodi Young – for their encouragement, guidance, and insightful suggestions that improved my work. I also thank Andy Schauer for his exceptional technical expertise and support in the lab. I am grateful for the camaraderie of collaborators in IsoLab, in the UW polar science community, and in the broader ice-core community. I thank my former office-mates Emma Kahle, Jess Badgeley, Gemma O'Connor, Mira Berdahl, and Sonja Wahl, whose advice and friendship enriched both my research and my graduate school experience. I am grateful for many opportunities to teach and mentor undergraduate students, some of whom contributed to this work. I acknowledge generous support from the US National Science Foundation Center for Oldest Ice Exploration (NSF 2019719), the Department of Earth and Space Sciences, NSF awards 1841844 and 2019219, the UW Program on Climate Change, the Cooperative Institute for Climate, Ocean, & Ecosystem Studies, and discretionary funding from Eric Steig's Ben Rabinowitz Professorship. I am forever grateful for reliable childcare providers and for many wonderful friends who supported my family throughout my time in graduate school. Finally, I am deeply grateful for the unwavering support of my husband, Nico Quijano, and for the infectious joy and insatiable curiosity of our son.

DEDICATION

for Stellan,

that knowledge of the past might brighten your future

Chapter 1

INTRODUCTION

This thesis explores the intersection of climatic (i.e. atmospheric) and glaciological influence on water-isotope records from shallow, discontinuous, blue-ice cores along the margins of the East Antarctic Ice Sheet. I specifically focus on advancing analytical techniques for the measurement of stable water isotopes in ice and on developing and interpreting water-isotope records from stratigraphically disturbed ice cores from the Allan Hills of Antarctica. This first chapter provides general background information on ice-core science, the water isotope system, motivations for extending ice-core paleoclimate records in time, and shallow ice drilling in the Allan Hills; it also outlines the scope and structure of the thesis, including a brief summary of each subsequent chapter. This thesis is motivated by the research goals of the Center for Oldest Ice Exploration (COLDEX), which has supported this work.

1.1 Ice core drilling and analysis

Polar ice sheets preserve accumulated snowfall, which is compacted over time such that temporally continuous ice samples can be recovered by coring. Polar ice cores contain direct archives of past precipitation and past atmosphere. Because both meteorological and glaciological processes can alter the geochemical composition of ice, ice-core records can provide information about both climate and glacial dynamics (e.g., Craig 1961; Johnsen et al., 1977). Detailed records of Earth's past climate from polar ice cores have provided foundational insights into Earth's climate system (e.g., Dansgaard et al., 1993; Jouzel et al., 1999).

Traditionally, paleoclimate records from ice cores have been developed from sites with relatively straightforward glacier dynamics to facilitate the disentanglement of climate signals and alteration due to glacial deformation (Dansgaard et al., 1973; Raymond, 1983). However, cores retrieved from more dynamic sites can provide qualitative and quantitative insights into local climatic or glaciological processes (e.g., Vimeux et al., 2001; Stenni et al., 2009; Stoll et al., 2022) and can extend the ice-core records in time (e.g., Shackleton et al., submitted; 2024; Peterson et al., 2024). Developing ice-core records from a glaciologically complex site with the goal of extending ice-core records in time is the focus of this thesis.

A brief overview of ice-core drilling and analytical techniques is reprinted from *Past Global Changes* in the following pages. All core samples used in this thesis were recovered by electromechanical drilling, during which rotational cutters bore into polar ice sheets to retrieve cyllindrical core samples. This thesis focuses on ice-core samples retrieved under difficult drilling conditions that led to suboptimal core recovery rates (especially at depth) and fractured or irregularly shaped core sections. In addition, at some sites, only basal ice was returned from the field. Most ice-core samples from the Allan Hills have been measured discretely, with either adjacent, equally-spaced samples (which are referred to by Table 1.2 as "continuous" samples), or irregularly spaced and irregularly sized samples that are not continuous along the depth of the core (which are referred to by Table 1.2 as "grab" samples). Detailed descriptions of all samples are provided later in this introductory chapter.

doi.org/10.22498/pages.30.2.98

From drilling to data: Retrieval, transportation, analysis, and long-term storage of ice-core samples

4

Lindsey Davidge[1], H.L. Brooks[2] and M.L. Mah[3]

Polar and alpine glacial ice is scientifically valuable, but it is logistically challenging to drill, transport, and store. We summarize the process of retrieving and analyzing a new core and identify archived samples that might be available for new research.

Ice cores collected from polar ice sheets and alpine glaciers provide a frozen archive of past atmospheric gases and precipitation that are important to glaciological and climate sciences. Ice-core analyses produce exceptionally well-resolved observations of local, regional, or global changes in the atmosphere over time. This is because as snow falls, a variety of physical processes affect its material properties and composition, and these signals get preserved through time. For example, ice flow direction affects the mineral orientation of frozen water, atmospheric composition determines the particle load and aqueous chemistry of an ice layer, and global and regional temperatures change the isotopic composition of the precipitation falling at an ice-core site; further, atmospheric gases trapped in the pore spaces between ice crystals are preserved and can be measured directly from ice-core samples (Banerjee et al. p. 104). Consequently, there are dozens of analyses that may be desirable to perform on a single ice-core sample. Drilling and preserving ice-core samples is challenging because cores are retrieved from frozen, often remote, and sometimes very deep (i.e. thousands of meters) sites. Despite this, cores are routinely recovered from scientifically advantageous locations, and ice samples are typically archived in storage facilities, where they may be available to support future research.

Drilling an ice core

Though the ice drilling process is similar at most sites, scientific objectives dictate the desired ice volume and depth, and cargo restrictions and site temperature may constrain equipment choices. Most core segments are about 10 cm in diameter and 1 m long, though the exact dimensions are determined by the size of the drill. Most core samples are retrieved by electromechanical drills; these drills contain a hollow cylinder, called the core barrel, that is equipped with rotational cutting teeth at the bottom (see Johnsen et al. 2007). Above the core barrel, an anti-torque device stabilizes the drill within the borehole while the cutters are spinning, and the entire drill assembly is suspended from a tripod or tower by an armored electrical cable (Fig. 1a). The rotating cutters pulverize a ring of ice, leaving a cylindrical pillar intact to enter the core barrel, while the remnant ice chips are removed from the cutting interface by circulating fluid and/or by helical flights (Fig. 1b). Each time the drill has progressed far enough to fill the core barrel, the ice pillar is broken off at its base, and the entire assembly is winched up to the surface. For electromechanical drills, the cutting force is supplied by electric motors, and the rate of penetration can be controlled by changing the weight above the bit. When drilling in ice warmer than -10°C, mechanical cutters tend to stick, and ice chip transport becomes difficult; at such sites, a ring-shaped heater is typically used to incise the ice instead in a process called thermal drilling (see Zagorodnov and Thompson 2014).

Glaciers and ice sheets are particularly inhospitable drilling environments. At the surface, heavy winds scour and redistribute recent snowfall, often burying scientific equipment or causing large snow drifts. Deeper in the ice sheet, ice flows under its own weight, causing deep boreholes to deform and close over time. Choices about infrastructure and equipment typically balance labor and cargo requirements with drilling efficiency and core quality. For example, drilling within covered trenches is the best way to avoid the impacts of drifting snow and bad weather, but a windscreen or tent might be a preferred alternative at sites where cargo capacity is limited or where the planned drilling season is short. Small drills or hand augers are used in alpine environments, where transporting personnel, equipment, and cores is often done by small aircrafts or even by foot or pack animal (Matoba et al. 2014; Schwikowski et al. 2014). However, deep ice-drilling projects in Greenland and Antarctica—which must penetrate multiple kilometers into the ice sheet—can utilize longer drill barrels, longer and stronger winch cables, and taller towers to minimize the number of trips up the borehole and accelerate the field campaign (Bentley and Koci 2007; Zhang et al. 2014). Boreholes deeper than about 300 m need to be backfilled with drilling fluid to prevent the borehole from collapsing (Talalay et al. 2014), though drilling fluid can also contaminate fractures within the core, which limits possible analyses.

Field storage and transportation

Once at the surface, cores are labeled with orientation and depth information and packaged carefully for transportation. Ice-core samples are susceptible to breakage, alteration, and melt, which means that preserving cores in the field and during transportation requires significant preparation; deep ice cores can be particularly fragile as they are removed from the ice sheet and rapidly decompress at the surface (Neff 2014). To inhibit physical, chemical, and biological alteration, it is desirable to store core samples at temperatures that are comparable to the in-situ temperature of the ice or at a maximum

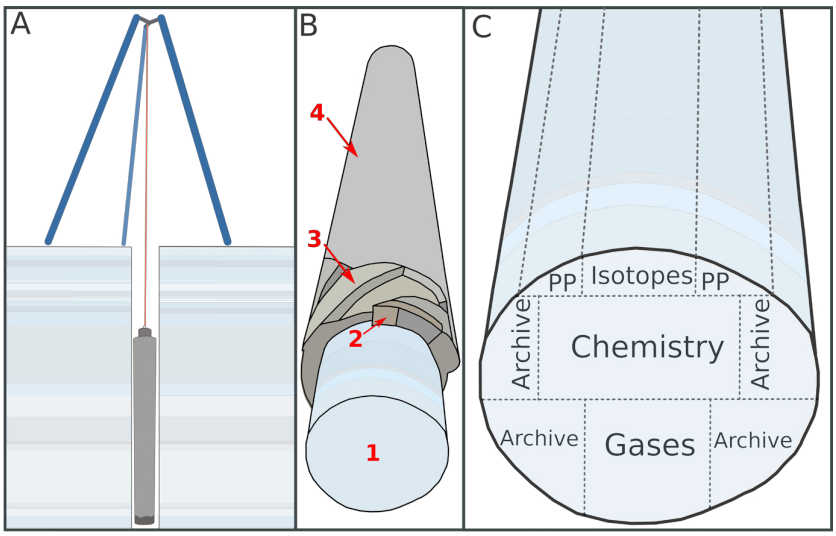

Figure 1: (A) Simplified cross section of an ice-drilling operation (not to scale). **(B)** Stylized drawing of an electromechanical drill, showing the retrieved core (1), cutters (2), helical flights (3), and core barrel (4). **(C)** An example of a cut diagram used to specify the target analyses for each portion of the core (PP = physical properties).

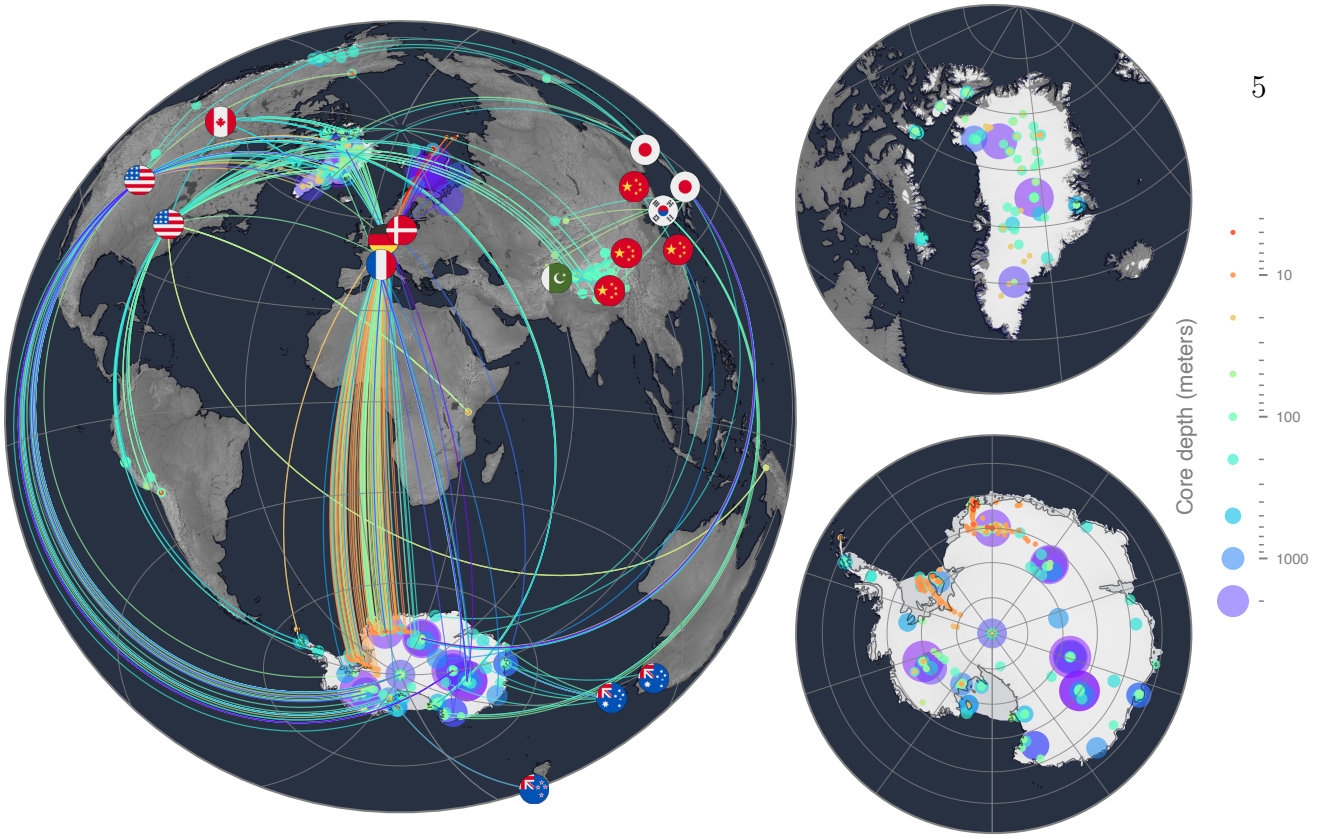

Figure 2: Map of selected ice drilling sites and storage locations, including details of Greenland (top right) and Antarctica (bottom right). Lines link the drill site and ice-storage location for each core (left). Many other archived samples exist in repository facilities around the world. Complete details are available in a corresponding database (Davidge et al. 2022).

of about -20°C. Cores are typically placed in insulated shipping boxes for protection during field storage and transportation. At polar drilling sites that remain frozen at the surface year-round, a shallow, covered trench dug into the snow is often enough to insulate the boxed cores for months or years. Storage at alpine glacier sites can be more complicated because these sites tend to be warmer and wetter than polar locations (e.g. Tsushima et al. 2021). Because of this, drilling at alpine sites is often seasonally constrained, and it is important to remove cores from these temperate sites as quickly as possible and place them in freezer storage.

The availability of onsite storage and field access limitations determine the method and frequency of transportation. Because ice cores from many polar sites can be safely stored at the drilling location—and because polar sites are often accessed by fixed-wing aircraft with substantial capacity for cargo—there is typically less urgency around transporting these cores, and their transportation can be scheduled similarly to other field-site cargo (e.g. Slawny et al. 2014). These cores are sometimes moved into temporary freezer storage at permanent research stations before being shipped to their destination country in refrigerated shipping containers aboard cargo ships or in smaller refrigerators aboard large aircrafts. For ground transport, temperature-controlled containers are transported by truck to national archive facilities or university laboratories for analysis.

Distribution and analysis of ice-core samples

Obtaining diverse measurements on an ice core typically requires that core samples be partitioned and distributed to multiple laboratories (Fig. 1c; as in Souney et al. 2014). Core samples are processed in one of two ways: discretely, by cutting the ice into small pieces and measuring the average properties of each subsample; or continuously, by melting one-meter "sticks" of the core from top to bottom and analyzing the resulting melt stream. It is desirable to make continuous measurements from ice-core samples when possible, because this method produces high-resolution timeseries while also minimizing sample handling and the potential for contamination (e.g. Osterberg et al. 2006; Röthlisberger et al. 2000). The volume of ice that is sent to each collaborating laboratory depends on analytical method requirements and project objectives.

Long-term ice-core storage

Notably, a portion of many cores has been archived in long-term storage facilities for use by future investigators. Ice from hundreds of field sites is stored in ice-core repositories within national research centers or universities (Hinkley 2003). Many of these samples are available for future research – and, indeed, many ice-core studies were conceptualized long after the ice core was originally retrieved. We provide a map of selected ice archives in Figure 2. Many core samples can be accessed by contacting the repository and proposing new strategies to leverage existing core samples to answer outstanding research questions.

AFFILIATIONS

[1]Department of Earth and Space Science, University of Washington, Seattle, USA
[2]School of Earth and Climate Sciences & Climate Change Institute, University of Maine, Orono, USA
[3]Department of Electrical and Computer Engineering, University of Minnesota, Minneapolis, USA

CONTACT

Lindsey Davidge: ldavidge@uw.edu

REFERENCES

Bentley CR, Koci BR (2007) Ann Glaciol 47: 1-9

Davidge L et al. (2022) Zenodo, doi:10.5281/zenodo.7076469

Hinkley T (2003) EOS 84: 549

Johnsen SJ et al. (2007) Ann Glaciol 47: 89-98

Matoba S et al. (2014) Ann Glaciol 55: 83-87

Neff PD (2014) Ann Glaciol 55: 72-82

Osterberg EC et al. (2006) Environ Sci Technol 40: 3355-3361

Röthlisberger R et al. (2000) Environ Sci Technol 34: 338-342

Schwikowski M et al. (2014) Ann Glaciol 55: 131-136

Slawny KR et al. (2014) Ann Glaciol 55: 147-155

Souney JM et al. (2014) Ann Glaciol 55: 15-26

Talalay P et al. (2014) Cold Reg Sci Technol 98: 47-54

Tsushima A et al. (2021) Ann Glaciol 62: 353-359

Zagorodnov V, Thompson LG (2014) Ann Glaciol 55: 322-330

Zhang N et al. (2014) Ann Glaciol 55: 88-98

1.2 Water-isotope measurements from polar ice cores

The stable water isotope composition from ice cores has been used as a paleothermometer since the advent of ice-core science (i.e. Langway, 1958; Gonfiantini and Picciotto, 1959; Dansgaard, 1964) and continues to be a key target for nearly all ice-core projects. Water-isotope data are reported as the fractional difference from an internationally accepted standard water:

$$\delta = \frac{\mathrm{R}_{sample}}{\mathrm{R}_{standard}} - 1 \tag{1.1}$$

where δ is given in parts per thousand (‰, or "permille"), and R refers to the ratio of heavy to light isotopologues (e.g., $^{18}\mathrm{R}{=}n(^{1}\mathrm{H}_2^{18}\mathrm{O})/n(^{1}\mathrm{H}_2^{16}\mathrm{O})$ for $\delta^{18}\mathrm{O}$ and $^{2}\mathrm{R}{=}n(^{2}\mathrm{H}_2^{16}\mathrm{O})/n(^{1}\mathrm{H}_2^{16}\mathrm{O})$ for $\delta\mathrm{D}$) where n is the abundance of either the sample or the standard. By convention, stable water isotope concentrations are calibrated against both Vienna Standard Mean Ocean Water (VSMOW) and Standard Light Antarctic Precipitation (SLAP) (see, e.g., Schoenemann et al., 2013).

During phase changes throughout the hydrologic cycle, water isotopologues undergo mass-dependent equilibrium fractionation, wherein heavy and light isotopologues are redistributed between phases in the way most thermodynamically favorable (Criss, 1999). The fractionation factor α quantifies the degree of separation by relating R for the initial phase to R in the second phase. For a liquid-vapor system at equilibrium described by A⇔B, the isotope fractionation factor is defined as:

$$\alpha_{B/A} = \frac{R_B}{R_A} \tag{1.2}$$

where R_B and R_A are the ratios of heavy to light isotopologues in the liquid and vapor phases, respectively. Equilibrium fractionation factors across a range of temperatures have been determined empirically for each phase of water and exhibit a characteristic temperature dependence (e.g., Majoube, 1970; Lehmann and Siegenthaler, 1991; Ellehoj et al., 2013; Casado et al., 2016).

Fractionation continuously modifies the isotopic signature of a parcel of water as it moves through Earth's hydrologic cycle, but isotope partitioning is rarely as straightforward as indicated by 1.2. That is because phase changes in Earth's atmosphere rarely occur at true equilibrium: relative humidity in the atmosphere is typically only 80% (Hartmann, 2015), not at saturation (i.e., not at equilibrium). This means that the partitioning of water isotopologues from a liquid ocean into atmospheric vapor that is described by Equation 1.2 does not reach completion, occurring instead in a steady-state dis-equilibrium that causes notable non-equilibrium fractionation. Non-equilibrium (or kinetic) fractionation is defined by the following equation from Merlivat and Jouzel, 1979:

$$\alpha_{\text{diff}} = (\frac{D}{D*})^n \tag{1.3}$$

where α_{diff} is the diffusive fractionation factor and D and D* are the effective diffusivities of the light and heavy isotopologues, respectively. The exponent n is a value between 0 and 1 that reflects environmental conditions such as wind speed and turbulence at the point of phase change (e.g., during evaporation from the ocean surface) (Merlivat and Jouzel, 1979). Because the diffusivities are different for each isotopologue (i.e., $^1H_2^{16}O$, $^2H_2^{16}O$, $^1H_2^{17}O$, $^1H_2^{18}O$, etc.), kinetic fractionation yields second-order differences between $\delta^{17}O$, $\delta^{18}O$, and δD; this gives rise to second-order water isotope quantities "^{17}O excess" ($\Delta^{17}O$) and "deuterium excess" (d_{excess}), which are both defined below (as in Barkan and Luz, 2010, and Dansgaard, 1964, respectively):

$$\Delta^{17}O = \ln(1 + \delta^{17}O) - 0.528 \cdot \ln(1 + \delta^{18}O) \tag{1.4}$$

$$d_{\text{excess}} = \delta D - 8 \times \delta^{18}O \tag{1.5}$$

$\Delta^{17}O$ is measured in per meg, and d_{excess} is measured in ‰, so care must be taken to ensure unit are consistent when using Equations 1.4 and 1.5, which are unitless expressions. Both $\Delta^{17}O$ and d_{excess} are defined as the excess of the relevant δ value (i.e. $\delta^{17}O$ or δD, respectively) from the global meteoric water line. While Equation 1.5 provides the most widely adopted

definition for d_{excess}, the linear slope of 8 is an approximation of a relationship that arises from nonlinear processes (Uemera et al., 2012; Markle et al., 2017; Markle and Steig, 2021). An alternative definition of the excess of δD is given by the non-linear formulation of Uemera et al., 2012 (which was corrected by Markle et al., 2017):

$$d_{ln} = \ln(1 + \delta D) - \left(A \times \ln(1 + \delta^{18}O)^2 + B \times \ln(1 + \delta^{18}O)\right) \tag{1.6}$$

a unitless expression where the coefficients A and B are -28.5 and 8.47, respectively. Because d_{excess} is more widely reported than d_{ln} and because the linear approximation is adequate for most applications, this thesis primarily considers d_{excess}, except in Chapter 5, where d_{ln} is more appropriate and is denoted accordingly.

In the atmosphere, the isotopic composition of meteoric water is distilled as it is carried from an evaporative source region to its precipitation site. This distillation can be modeled by simple Rayleigh equations, which provide a first-order approximation to observed isotope-temperature relationships, which are nearly linear at high latitudes (Lorius et al., 1969; Johnsen et al., 1989). Consequently, stable isotopes of oxygen (δ^{18}O) and hydrogen (δD) have been foundational to ice-core paleoclimate science (Jouzel et al., 1997). Water-isotope measurements from ice, used as a temperature proxy, alongside corresponding, direct measurements of past atmospheric composition from the bubbles contained in the ice, enables the study of how the atmosphere has changed with temperature through at least the last 800,000 years of Earth's history (Berner et al., 1980; Petit et al., 1999). Measurements of d_{excess} and, more recently, Δ^{17}O, provide more complete information about the integrated history of moisture that is archived in polar ice sheets (e.g., Merlivat and Jouzel, 1979; Landais et al., 2008; Schoenemann et al., 2014; 2015; Markle and Steig, 2021).

Although the initial isotope composition in a snow-accumulation area is determined by atmospheric thermodynamics, alteration and deformation in both firn (i.e., compacted snow) and ice can alter the water-isotope signal that is recovered from deep ice cores. For example, vapor exchange with surface snow can bias the water isotope signal in recent snowfall (e.g. Casado et al., 2016; Wahl et al., 2021), interstitial vapor transport within the firn column

can smooth the water isotope record through diffusion (e.g. Whillans and Grootes, 1985; Cuffey and Steig, 1998; Johnsen et al., 2000; Gkinis et al., 2014; Jones et al., 2017a), and ice flow dynamics can cause thinning and internal deformation (Dahl-Jensen et al., 1997; Alley et al., 1997; Bell et al., 2011). Characterizing the effects of these processes on the climate signal is important for interpreting the water-isotope record as a climate history (Casado et al., 2018).

In fact, interpreting water-isotope records from any ice-core site requires an understanding of the combined history of both atmospheric distillation and post-depositional changes. Early work to develop the water-isotope temperature proxy relied upon a conceptual model of atmospheric distillation that allowed qualitative interpretations of isotopic fluctuations as temperature cycling (Dansgaard, 1964); simple quantitative approaches rely on the modern isotope-temperature relationship of modern, spatially distributed snowfall (Petit et al., 1999; Johnsen et al., 2001). Most computational approaches model distillation with Rayleigh equations to yield quantitative estimates of temperature, most commonly at the precipitation site (e.g., Merlivat and Jouzel, 1979; Ciais and Jouzel, 1994; Kavanaugh and Cuffey, 2003; Markle and Steig, 2021). Because polar ice cores comprise snowfall that has been metamorphosed into ice, conceptual or computational models of snow (firn) densification and ice flow are also necessary for disentangling climatic information from post-depositional changes. Most paleoclimate records are developed from ice cores retrieved from high-accumulation ice divides, where ice archival and deformation processes are straightforward and can be accounted for with simple models of thinning and diffusion (Dansgaard and Johnsen, 1969; Johnsen et al., 1995; Cuffey and Steig, 1998). At sites with more complicated histories, building a conceptual model that accounts for the cumulative history of the archived precipitation is necessary for quantitative or qualitative interpretation of the water-isotope record. This thesis examines water-isotope data from glaciologically disturbed ice-core samples and leverages information retained by those samples to build a conceptual model of climate and glacial processes affecting a 6-million-year-old water-isotope history from the Allan Hills of Antarctica.

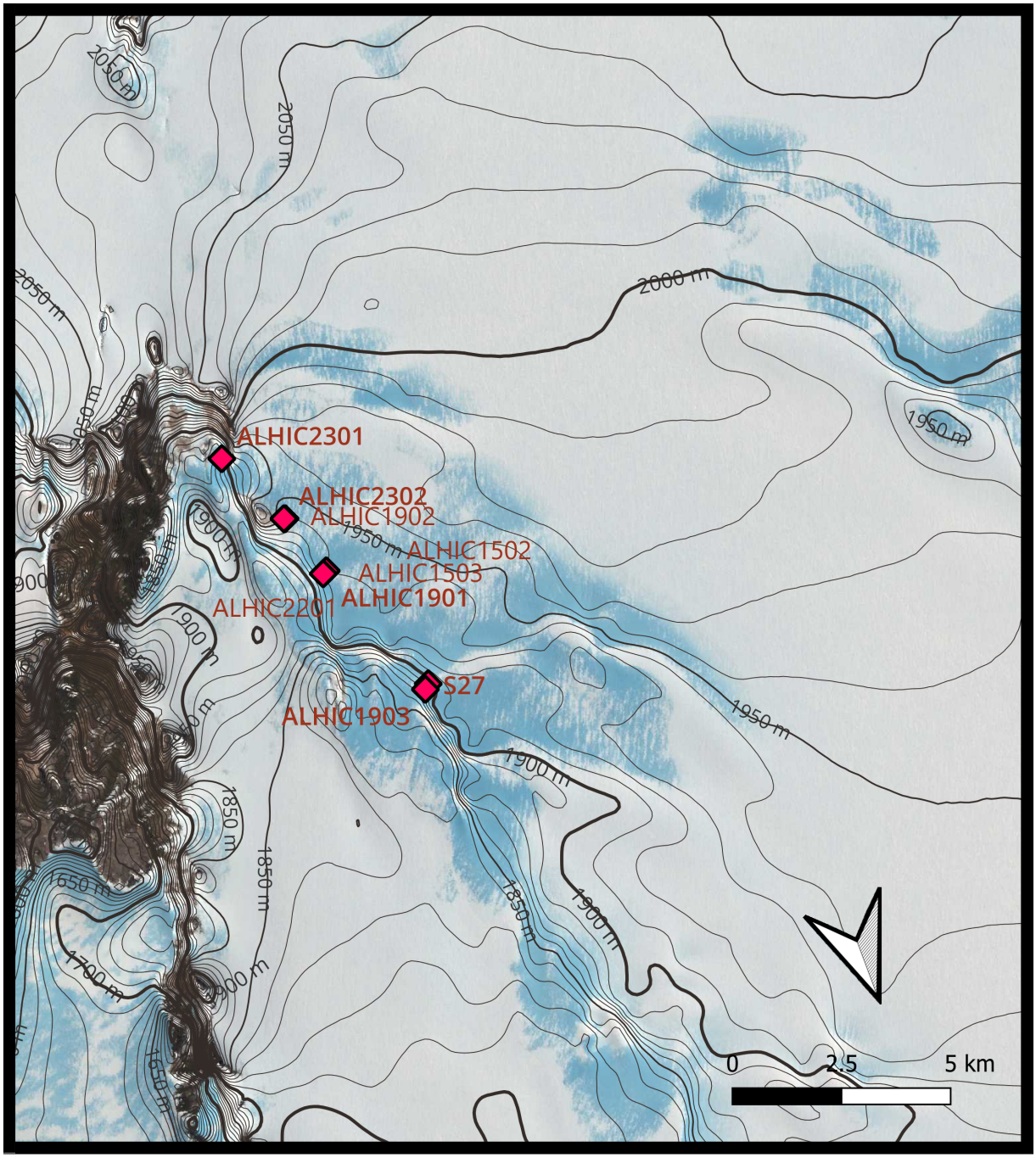

Figure 1.1: Distribution of Allan Hills core sites discussed by this thesis. Satellite imagery is from the Landsat Image Mosaic of Antarctica (LIMA; British Antarctic Survey and others, 2007) and the surface contours are from the Reference Elevation Map of Antarctica (REMA; Howat et al., 2019). Modern ice flow is from a local accumulation area in the south (not shown) towards the nunatak.

Site ID	Latitude	Longitude	Depths Recovered	Age range
S27	-76.70330	159.30647	1-224 m	114-254 ka
ALHIC1502	-76.73286	159.35507	1-197 m	0.3-2.7 Ma
ALHIC1503	-76.7324	159.3562	126-147 m	0-1.1 Ma
ALHIC1901	-76.732376	159.356125	136-160 m	0.4-4 Ma
ALHIC1902	-76.745357	159.374108	134-206 m	0.5-6+ Ma
ALHIC1903	-76.702435	159.310603	77-144 m	0-216 ka
ALHIC2201	-76.732027	159.359551	0-90 m	0.3-1.1 Ma
ALHIC2301	-76.761446	159.408303	2-89 m	Not available
ALHIC2302	-76.745432	159.375134	0-143 m	Not available

Table 1.1: **List of Allan Hills ice cores discussed in this thesis.** Each core used in this thesis is listed alongside geographical data and the depths of returned samples. Details about dating can be found in Spaulding et al., 2013 (for S27), Higgins et al., 2015 and Yan et al., 2019 (for ALHIC1502 and ALHIC1503), and Shackleton et al., submitted (for ALHIC1901, ALHIC1902, and ALHIC1903). ALHIC2201 dates were produced by ^{40}Ar dating at Scripps Institute of Oceanography and Princeton University and are not yet published (personal correspondence).

1.3 The mid-Pleistocene transition and extending ice-core records in time

The oldest published continuous ice-core records are from the European Project for Ice Coring in Antarctica (EPICA) Dome C core (EDC), which is a 3.2-km-long core that contains an 800-ky history of precipitation and gases in East Antarctica (EPICA Community Members, 2004; Jouzel et al., 2007). Data from EDC establish high-resolution observations of the timing and magnitude of temperature (Jouzel et al., 1997), chemistry (Wolff et al., 2010), dust (Lambert et al., 2008), and greenhouse gases (Lüthi et al., 2008; Loulergue et al., 2008) over the last eight glacial cycles. These observations were instrumental in identifying the direct relationship between atmospheric composition and global temperature (Petit et al., 1999; Shakun et al., 2012).

Sediment-core records extend further back in time, but are limited in temporal resolution and contain only indirect archives of past climatic conditions. Oceanic δ^{18}O composition fluctuates over time as a function of ice-sheet volume, which leads to enrichment of oceanic δ^{18}O; the incorporation of δ^{18}O into the calcite shells of benthic foraminifera depends on the composition and temperature of the ocean (Hays et al., 1976; Farmer et al., 2023). Marine sediment cores recover chronological deposits of benthic δ^{18}O extending back millions of years (i.e. Lisiecki and Raymo, 2005). Observations of glacial cycling with 100-ky regular intervals were first detected in benthic δ^{18}O (Hays et al., 1976). This observation confirmed theorized climate sensitivity to orbital variations in Earth's eccentricity, obliquity, and precession, which have characteristic periods of 100,000, 41,000, and 22,000 years, respectively. However, the cause for the apparent dominance of the eccentricity forcing was not clear (Hays et al., 1976); even more, a separate benthic record identified a change in periodicity from 41-kyear cycles to 100-kyear cycles between 1250 and 700 ka despite no apparent change in forcing (Shackleton and Opdyke, 1976; Clark et al., 2006; Lisiecki and Raymo, 2005). This observed shift in the climate's response to orbital forcings is referred to as the mid-Pleistocene transition (MPT), and represents a fundamental gap in our knowledge of Earth's climate sensitivity (Roe and Allen, 1999; Clark et al., 2006). Investigating the cause of the

MPT is the focus of ongoing, international research efforts.

Possible explanations for the MPT rely upon ice-sheet growth feedbacks or instabilities (e.g., Gregoire et al., 2012; Bintanja and van de Wal, 2008; Marshall and Clark, 2002), erosion of subglacial regolith (Clark and Pollard, 1998), changes in sea-ice extent (Gildor and Tziperman, 2000; 2001), or changes in ocean circulation and greenhouse gases (Willeit et al., 2019; Kohler and Bintanja, 2008). Ice cores that extend beyond 1 Ma could provide additional evidence needed to evaluate the cause or causes of the MPT because they contain a direct archive of past atmospheric gases and meteoric water, and can therefore be used to generate corresponding histories of temperature, greenhouse gases, and other observations that could elucidate causes of this climatic shift.

1.4 COLDEX and shallow coring in the Allan Hills, Antarctica

In 2022, the Center for Oldest Ice Exploration (COLDEX) was established within the U.S. ice coring community. COLDEX aims to retrieve >1-Ma ice from Antarctica in order to study Earth's climate during the MPT. Following earlier work by Spaulding et al. (2013), Higgins et al. (2015), and Yan et al. (2019; 2021), COLDEX has retrieved several shallow (<200-m) ice cores from the margins of the East Antarctic ice sheet over the last few years. These cores, which were recovered from the Allan Hills blue ice area (BIA), have ages as old as 6 Ma near the bed (Shackleton et al., submitted; Table 1.1), with many recovered intervals that span the ages of the MPT.

Blue ice areas typically form near the margins of the ice sheets in mountainous locations where a combination of local topography and katabatic winds cause net ablation of ice and movement of older layers towards the surface (Bintanja, 1999). This complex ice flow causes internal deformation on scales that are not known and often results in stratigraphically disordered layers and complex age-depth relationships (Sinisalo and Moore, 2010; Shackleton et al., submitted). Developing paleoclimate records from blue ice is facilitated by the absolute dating of noble gases trapped in bubbles within the ice; specifically, measuring atmospheric ^{40}Ar – which is accumulated in the atmosphere over time due to the continuous crustal

outgassing of ^{40}K – provides an age constraint (Bender et al., 2008). However, the analysis is volume-intensive (200-300g minimum; Shackleton et al., submitted), and a lack of theoretical or observational information about layer thinning in blue ice adds uncertainty to the amount of time represented by each dating constraint and the continuity of the age-depth relationship between sampled intervals.

COLDEX researchers across several institutions are working collaboratively to study ice-core geochemical records and the geophysical context of ice in the Allan Hills. Records of mean ocean temperature reconstructed from noble gas ratios (Shackleton et al., 2024) and greenhouse gases (Peterson et al., in review) provide discontinuous snapshots of earth's climate over the last few million years. Shackleton et al. (submitted) also demonstrates that water-isotope data combined from three different core sites imply temperature changes similar in timing and magnitude to marine records over the last 6 million years. Despite this, significant uncertainty in interpreting the water-isotope data arises from a fundamental lack of information about the meteorological and glaciological origins of ice in the Allan Hills over long timescales.

In this thesis, I present new water-isotope data from a combination of dated and undated Allan Hills ice cores drilled prior to the 2024-2025 drilling season, and use those data to infer a conceptual model of water-isotope distillation and preservation controls over multimillion-year timescales. Locations and age information for cores discussed in this thesis are provided in Table 1.1 and are included in Figure 1.1. Note that this is not an exhaustive list of ice retrieved from the Allan Hills, but rather a summary of cores and records that are relevant to the research reported in this thesis. The cores shown in Table 1.1 and Figure 1.1 are locations from which water-isotope measurements have been made. Specific datasets that are referred to by subsequent thesis chapters are summarized by Table 1.2.

1.5 Scope and structure of this thesis

Building a conceptual model for the the climatic and glaciological origins of the ice recovered from the Allan Hills is important for developing and interpreting water-isotope data

Site ID	H_2O isotope data	Resolution	Type	Depth range	Source
S27	δD	0.15±0.07 m	C	1-224 m	Spaulding (2013)
ALHIC1502	δD, δ^{18}O	0.10±0.01 m	C	1-191 m	Yan (2019)
ALHIC1503	δD, δ^{18}O	0.33±0.60 m	C	32-147 m	Higgins (2015), Yan (2019)
ALHIC1901	δD, δ^{18}O	0.46±0.51 m	G	134-160 m	Shackleton (submitted)
	δD, δ^{18}O, δ^{17}O	0.010±0.001 m	X	135-142 m	this study
	δD, δ^{18}O	0.010±0.001 m	X	155-160 m	this study
ALHIC1902	δD, δ^{18}O	3.82±3.56 m	G	141-207 m	Shackleton (submitted)
	δD, δ^{18}O	0.48±0.34 m	C	135-162 m	this study
	δD, δ^{18}O	0.010±0.001 m	X	206-207 m	this study
ALHIC1903	δD, δ^{18}O	0.83±0.45m	G	77-143 m	Shackleton (submitted)
	δD, δ^{18}O	1.1±1.4 m	G	75-145 m	Carter (2024)
ALHIC2201	δD, δ^{18}O	0.78±0.29 m	C	0-90 m	this study
	δD, δ^{18}O, δ^{17}O	$\leq$0.05 m	C	0-68 m	this study*
ALHIC2301	δD, δ^{18}O	0.66±0.31 m	C	2-89 m	this study
ALHIC2302	δD, δ^{18}O	0.46±0.37 m	C	0-143 m	this study

Table 1.2: **List of water isotope datasets from the Allan Hills that are used in this thesis.** While only δ values are listed, note that d_{excess} and Δ^{17}O can be derived from corresponding measurements of δ^{18}O and δD or δ^{18}O and δ^{17}O, respectively. The resolution is provided for all discrete samples as the mean$\pm\sigma$ of the interval between samples. The resolution for data produced by continuous-flow analysis is an estimate. Continuous type (C) samples are primarily spatially continuous between depth intervals. Grab type (G) samples are primarily discontinuous, and are likely not representative of the full interval between samples. Datasets marked as X are a combination of types, where continuous measurements have been made along samples that are not fully representative of the indicated depth interval. An asterisk denotes measurements made in collaboration with others. Published isotope data are listed by the first author and publication year.

from these sites. This thesis builds on earlier work to add new constraints on climate and ice histories in the Allan Hills from water-isotope data. Subsequent chapters establish measurement protocols, climate and ice-flow history inferences, and preservation constraints for water-isotope composition at the Allan Hills over the last 6 million years using a combination of water-isotope observations from the Allan Hills and simple isotope modeling of glaciological and atmospheric processes. While many questions remain about processes governing signal preservation in this region, this thesis lays important groundwork for interpreting water-isotope data from disordered Allan Hills ice. This document contains four additional chapters, which are briefly described below.

Chapter 2. This chapter establishes measurement protocols for simultaneous measurement of all stable water isotopes (i.e. δ^{17}O, δ^{18}O, δD, Δ^{17}O, and d_{excess}[1]) from ice cores. I designed, constructed, and implemented a continuous-flow sample processing line that is combined with a laser spectrometer to measure water isotopes in ice cores. Measurements of δ^{18}O, δD, and d_{excess} are routine in many ice-core laboratories; continuous measurements of Δ^{17}O (and δ^{17}O) are less common, in part due to uncertainty in the error imparted by the continuous-flow line. I use the continuous-flow line to make replicate measurements from a Greenland ice core, quantify the Δ^{17}O error, and establish best practices for the calibration of Δ^{17}O. A modified version of the instrumentation described in this chapter is now installed at the COLDEX laboratory in Corvallis, Oregon.

Chapter 3. This chapter leverages the likeness of the water-isotope composition from ice with similar spatiotemporal origins to infer details about ice flow at large and small scales in the Allan Hills. Because the scale of distortion in blue ice is not known a priori and ice-flow history is poorly constrained, it is possible that core samples have different spatial or temporal origins, or that same-depth measurements in a single core are not temporally synchronous. I evaluate the reproducibility of water-isotope data along geographically distinct depth profiles, both by examining the overall distribution of data logged at each

[1]Note that because both are derived from direct measurements of δ^{18}O and δD, d_{excess} is analytically equivalent to d_{ln}, so this method can be used to determine either or both quantities.

core site and by cross-correlating 1) meter-scale climatic information between cores and 2) centimeter-scale climatic information from two sides of a 24-cm ice core. I show that meter-scale water-isotope measurements are significantly correlated at distances up to 140 m along a flowline ($0.27 < r < 0.80$). We show that centimeter-scale measurements within a core are reproducible on both sides with minor distortion, and that they exhibit similar dip angles and thinning asymmetry as the meter-scale averages. These results imply a conceptual flow model of extensional thinning with internal deformation along the flowline as ice is ablated from the downstream ice surface.

Chapter 4. This chapter confirms that high-frequency information preserved in a well-dated, stratigraphically disturbed blue-ice core is consistent with climatic information that has undergone dramatic extensional thinning (with layers likely 10^3 to 10^5 times thinner than at deposition) and moderate diffusion. I develop a refined age scale for new, 1-cm vertically resolved water-isotope data and compare the data with results from a synthetic core diffusion experiment based on Dome C climate. I show that measured isotope values are well-approximated by diffusion of layers with an approximately seven-fold interglacial accumulation increase. I find a local decrease in δD, δ^{18}O, and d_{excess} since 725 ka in all Allan Hills isotope records, and speculate that a combination of upstream elevation changes and sublimation of blowing snow could cause this change in the observed isotopic relationship since the MPT.

Chapter 5. In this chapter, I consider changes to earth's water cycle over multimillion-year timescales. I use a simple water isotope model to explore the impact of warmer ocean temperature, enriched ocean isotopic composition, and changed conditions at the ocean-atmosphere boundary on the water-isotope composition (especially d_{ln}) of polar snow. I present new water-isotope data from basal ice in ALHIC1902 that is older than (and stratigraphically beneath) ice with dates of 5-6 Ma, and demonstrate that the direction of isotopic changes observed in Miocene ice from the Allan Hills is consistent with distillation in a warmer world. This work provides initial insight into the temperature-isotope relationship of polar snow during a warmer climate state.

Chapter 2

CONTINUOUS-FLOW METHODOLOGY FOR STABLE WATER ISOTOPES BY LASER SPECTROSCOPY

2.1 Overview

In this chapter I detail the development of a continuous-flow measurement method for all stable isotopes of water (δ^{17}O, δ^{18}O, δD, d, and Δ^{17}O) by laser spectroscopy. Continous-flow analysis (CFA) is more efficient than discrete sampling and can be integrated with other measurements to generate synchronized high-resolution records of multiple analytes. For this reason, CFA is an ideal analytical method for COLDEX cores[1]. Measuring all stable-water isotopes (i.e. including δ^{17}O and Δ^{17}O) provides the most information about the combind history of an ice sample, but inclusion of δ^{17}O and Δ^{17}O is less common for CFA and errors associated with CFA implemntation are not well characterized. While CFA for water-isotope measurements has been widely adopted since its original implemenation by Gkinis et al. (2011), the South Pole Ice Core (SPC14) was the first ice core to be analyzed by CFA including δ^{17}O and Δ^{17}O (Steig et al., 2021); uncertainty remained as to the nature of fluctuations in calibrated values of Δ^{17}O over time. The following section addresses this uncertainty by quantifying the relative and absolute performance of the method on replicate sections of an ice core from Summit, Greenland, and by identifying improvements to the calibration technique that can be used to reduce error.

This chapter includes an article reprinted from *Atmospheric Measurement Techniques* in Section 2.2 and from *Past Global Changes* in Section 2.3. Section 2.4 describes the deployment of this technology for COLDEX research.

2.2 Improving continuous-flow analysis of triple oxygen isotopes in ice cores: insights from replicate measurements

The following article is reprinted from *Atmospheric Measurement Techniques*.

---

[1]In practice, many cores from the Allan Hills are not continuous – that is, not all depth intervals are recovered as intact cyllindrical core samples, and the quality of core in regards to shape, internal fracture, and section length is highly variable. Nevertheless, CFA is the most efficient way to generate high-resolution datasets from core of sufficient quality, and is a desirable tool to have available for COLDEX analysis.

Atmos. Meas. Tech., 15, 7337–7351, 2022
https://doi.org/10.5194/amt-15-7337-2022

Atmospheric Measurement Techniques
Open Access
EGU 20

Improving continuous-flow analysis of triple oxygen isotopes in ice cores: insights from replicate measurements

Lindsey Davidge, Eric J. Steig, and Andrew J. Schauer

Department of Earth and Space Sciences, University of Washington, Seattle, WA 98195, USA

Correspondence: Lindsey Davidge (ldavidge@uw.edu)

Received: 17 March 2022 – Discussion started: 25 April 2022
Revised: 2 November 2022 – Accepted: 9 November 2022 – Published: 22 December 2022

Abstract. Stable water isotope measurements from polar ice cores provide high-resolution information about past hydrologic conditions and are therefore important for understanding earth's climate system. Routine high-resolution measurements of $\delta^{18}O$, δD, and deuterium excess are made by continuous-flow analysis (CFA) methods that include laser spectrometers. Cavity ring-down laser spectroscopy (CRDS) allows for simultaneous measurements of all stable water isotopes, including $\delta^{17}O$ and ^{17}O excess ($\Delta^{17}O$); however, the limitations of CFA methodologies for $\Delta^{17}O$ are not well understood. Here, we describe a measurement methodology for all stable water isotopes that uses a CFA system coupled with a CRDS instrument. We make repeated measurements of an ice-core section using this method to explore the reproducibility of CFA–CRDS measurements for $\Delta^{17}O$. Our data demonstrate that the CFA–CRDS method can make high-precision measurements of $\Delta^{17}O$ (< 5 per meg at averaging times > 3000 s). We show that the variations within our CFA ice-core measurements are well matched in magnitude and timing by the variations within the discrete CRDS measurements; we find that calibration offsets generate most of the variability among the replicate datasets. When these offsets are accounted for, the precision of CFA–CRDS ice-core data for $\Delta^{17}O$ is as good as the precision of $\Delta^{17}O$ for continuous reference water measurements. We demonstrate that this method can detect seasonal variability in $\Delta^{17}O$ in Greenland ice, and our work suggests that the measurement resolution of CFA–CRDS is largely defined by the melt and measurement rate. We suggest that CFA–CRDS has the potential to increase measurement resolution of $\delta^{17}O$ and $\Delta^{17}O$ in ice cores, but also highlight the importance of developing calibration strategies with attention to $\Delta^{17}O$.

1 Introduction

Records of water isotopologues from ice cores are fundamental to the study of past climate processes (Dansgaard, 1964). Oxygen ($\delta^{18}O$) and hydrogen (δD) isotope ratios have been measured routinely in ice-core samples and in other natural waters due to their well-understood, first-order equilibrium fractionation relationship to atmospheric temperature (Jouzel et al., 1997). Additionally, deuterium excess (d) is commonly used as an indicator of kinetic fractionation processes within the hydrologic cycle (Merlivat and Jouzel, 1979; Jouzel and Merlivat, 1984). Deuterium excess is conventionally defined as

$$d = \delta D - 8 \times \left(\delta^{18}O\right). \quad (1)$$

Barkan and Luz (2005) showed that measuring $\delta^{17}O$ and $\delta^{18}O$ at a sufficiently high precision allows for the determination of ^{17}O excess ($\Delta^{17}O$), a quantity that, like d, also reflects nonequilibrium fractionation processes such as sea-surface humidity (Uemura et al., 2010; Barkan and Luz, 2007) and supersaturation effects during snow formation (Schoenemann et al., 2014; Schoenemann and Steig, 2016). $\Delta^{17}O$ is defined by Luz and Barkan (2010) as the deviation in $\delta^{17}O$ from the global meteoric water line:

$$\Delta^{17}O = \ln\left(\delta^{17}O + 1\right) - 0.528 \ln\left(\delta^{18}O + 1\right), \quad (2)$$

where δ ("delta") values are expressed as a unitless fractional deviation from Vienna Standard Mean Ocean Water (VSMOW; see, e.g., Schoenemann et al., 2013, for a complete discussion of nomenclature).

Measurements of $\delta^{18}O$, δD, and d by laser spectroscopy have been demonstrated by many laboratories (e.g., Kerstel

et al., 1999; Iannone et al., 2010; Steen-Larsen et al., 2014; Schauer et al., 2016; Jones et al., 2017a); for water isotope measurements of ice cores, it is increasingly common to couple a laser spectrometer with a continuous-flow analysis (CFA) system. CFA processing reduces sample handling and can produce very high depth resolution (originally described by Gkinis et al., 2010, 2011). Highly resolved water isotope measurements are advantageous for a variety of studies, such as those that use the water isotope diffusion length to infer information about firn processes or to reconstruct temperature histories (e.g., Gkinis et al., 2014; Kahle et al., 2018, 2021; Jones et al., 2017b). It is desirable to obtain measurements of $\delta^{17}O$ and $\Delta^{17}O$ at a resolution comparable to that for $\delta^{18}O$, δD, and d. Corresponding measurements of both $\Delta^{17}O$ and d – which have differing sensitivities to kinetic fractionation processes – could help to disentangle the various processes that influence water isotope values during evaporation, atmospheric transportation, and snow formation (Angert et al., 2004; Uemura et al., 2010). However, measurements of $\Delta^{17}O$ require much higher precision than the other water isotope ratios and have therefore generally been obtained by isotope-ratio mass spectrometry (IRMS) (Luz and Barkan, 2010; Landais et al., 2008, 2012a, b; Schoenemann et al., 2013, 2014). Because the IRMS method is relatively expensive and time-consuming, $\Delta^{17}O$ measurements from ice cores are limited in spatial and temporal resolution (e.g., Schoenemann et al., 2014; Aron et al., 2021). CFA for $\Delta^{17}O$ has the potential to address this limitation.

Laser spectroscopy enables simultaneous measurements of $\delta^{17}O$, $\delta^{18}O$, and δD (and therefore d and $\Delta^{17}O$). Steig et al. (2014) developed a cavity ring-down laser spectrometer (CRDS) for $\Delta^{17}O$ analysis, sold commercially as the Picarro L2140-*i*; other instruments with different spectroscopic methods have also been developed for $\Delta^{17}O$ analysis (e.g., Berman et al., 2013; Tian et al., 2016). Schauer et al. (2016) demonstrated that the L2140-*i* CRDS configured with an autosampler can routinely measure $\Delta^{17}O$ from discrete water samples with precision and accuracy comparable to IRMS methods. Steig et al. (2021) obtained continuous measurements of all water isotope quantities ($\delta^{17}O$, $\delta^{18}O$, δD, d, and $\Delta^{17}O$) on an ice core from the South Pole by using the L2140-*i* CRDS coupled with the CFA system developed by Jones et al. (2017a). However, despite the potential shown by these studies, the adoption of CFA–CRDS for $\Delta^{17}O$ faces two primary challenges. First, the integration time required for high-precision $\Delta^{17}O$ measurements by CRDS – approximately 1000 s to achieve precision of 10 per meg (Steig et al., 2014) – is much greater than the integration time required to achieve meaningful precision for $\delta^{18}O$, δD, or d. Second, the CFA system – i.e., the melting and vaporization process used to introduce an ice-core sample into the CRDS – may further degrade the measurement quality by processes that are not yet well understood. For example, Steig et al. (2021) identified occasional large (> 20 per meg) offsets in CFA–CRDS $\Delta^{17}O$ in their measurements of the South Pole ice core; the cause of these offsets was unclear. It is our goal to characterize the reproducibility of replicate ice-core measurements of $\Delta^{17}O$ by CFA–CRDS.

Here, we describe a CFA–CRDS measurement methodology that was designed for high-resolution measurements of $\Delta^{17}O$. We take advantage of archived ice-core samples from Summit, Greenland, to make repeated CFA–CRDS measurements of $\Delta^{17}O$. These samples (collected by Hastings et al., 2009) provide an opportunity to explore the potential and limitations of $\Delta^{17}O$ measurements by CFA–CRDS more fully. We use replicate measurements made by CFA–CRDS and discrete CRDS methods to assess the reproducibility of CFA–CRDS $\Delta^{17}O$ data and to identify sources of measurement error.

2 CFA–CRDS design and configuration

We use a CFA processing line in combination with a CRDS laser spectrometer (L2140-*i*, Picarro Inc., as in Steig et al., 2014) to measure $\Delta^{17}O$ of ice-core samples. The function of the CFA line is to generate a continuous supply of constant-humidity sample vapor to the CRDS analyzer; to achieve this, we have built a custom vaporizer unit that is described below. A constant stream of vaporized sample is important because errors in isotope-ratio measurements can arise from inconsistent vapor pressure at the CRDS inlet (Gkinis et al., 2011; Schauer et al., 2016). Finally, we aim to reduce diffusion and mixing within the CFA system to avoid smoothing the resulting measurements.

2.1 Custom vaporizer design

Continuous and complete vaporization is critical to reducing errors in all CRDS stable water isotope measurements, and it is especially important for attaining the per-meg precision necessary to detect meaningful variations in $\Delta^{17}O$. Previous studies have achieved continuous vaporization by heating sample water in the presence of dry air, either within an insulated stainless-steel tee (e.g., Gkinis et al., 2010, 2011) or within a concentric glass nebulizer with a vaporizing tube (e.g., Emanuelsson et al., 2015; Jones et al., 2017a). Gkinis et al. (2010, 2011) designed a flash vaporization process to instantaneously vaporize a continuous stream of sample water; the flash vaporization process involves a continuous stream of water that is combined with a continuous stream of dry air inside a 0.50 mm internal diameter stainless-steel tee that is maintained at near-ambient pressure. Steig et al. (2021) measured $\Delta^{17}O$ by CFA–CRDS with the CFA configuration of Jones et al. (2017a): a continuous stream of water sample at 1030 kPa (150 psi) is aerosolized within a concentric glass nebulizer; the aerosolized sample droplets then evaporate completely within a 1.8 cm internal diameter, 20 cm long glass vaporizing tube that is heated to 200 °C. In this configuration, the CRDS analyzer draws vaporized sample from the

vaporizing tube, and excess sample vapor is vented to the laboratory air (Jones et al., 2017a; Steig et al., 2021). Two critical differences between the Gkinis et al. (2010, 2011) and Jones et al. (2017a) methods are the volume of the vaporization chamber and the volume of vapor that is generated. The smaller volume of the flash vaporizer should limit signal smoothing between the vaporizer and the analyzer. However, the flash vaporization method described by Gkinis et al. (2010, 2011) generates vapor at approximately the rate that is required by the analyzer, whereas the nebulizer method of Jones et al. (2017a) produces an excess of vapor that is vented prior to reaching the analyzer. Producing excess vapor is another way to limit the signal smoothing upstream of the vapor vent because it increases the velocity of sample through the system.

For this study, we built a custom vaporizer unit that benefits from both the small volume of the flash vaporizer and also from the production of excess sample vapor; we also adopted additional monitoring techniques to ensure that there are stable flow conditions within the system during analysis. We use a 0.50 mm stainless-steel tee like Gkinis et al. (2010, 2011) but instead operate our vaporizer at a high mixing pressure (typically 200 kPa) to produce excess vapor. A small system volume combined with a high volumetric flow rate leads to a short retention time within the vaporizer that limits mixing of adjacent ice-core layers. An additional benefit of the small vaporizer volume is that flow inconsistencies (i.e., changes in sample flow rate caused by flow obstructions or bubble interruptions) that may occur within the vaporizer can be observed by the 1 Hz CRDS measurement values; patterns in water vapor concentration or instantaneous isotope readings provide information about vaporization conditions that is important for identifying and avoiding water isotope fractionation. We use CRDS observations of water concentration and uncalibrated water isotope values as well as electronic pressure sensors to infer vaporization conditions that may affect $\Delta^{17}O$. This information is used to tune the CFA–CRDS system prior to analysis, with the goal of reducing possible isotope fractionation that may cause errors in $\Delta^{17}O$; this process is described more fully in Sect. 3.1.

2.2 CFA–CRDS system configuration

The CFA process from the ice-core melter to the vaporizer and vapor analyzer is described below and illustrated in Fig. 1. Glacial ice is melted on a 30 mm × 30 mm aluminum melt head that is fitted with four resistance heater cartridges and held at constant temperature by a PID controller (Bigler et al., 2011). Sample melt is drawn away from the melt head and through an automated selector valve (VICI, p/n C25Z-3186EMH) by a dedicated peristaltic pump, PUMP-1 (MasterFLex L/S 7535-04). The automated valve is configured to select a rotating sequence of calibration standards when ice cores are not being measured. Sample melt is carried by 0.5 mm internal diameter PFA conveyance tubing between all system components prior to the vaporizer; PFA tubing was chosen because its transparency is advantageous for identifying bubbles and investigating flow instability issues. From PUMP-1, water flows through a Darwin Microfluidics gas-permeable membrane bubble trap (44 µL internal volume, p/n LVF-3526) where bubbles are removed and vented into the laboratory air. Excess water pressure is relieved at a vent. Sample water is drawn away from the vent by PUMP-2 (same model as PUMP-1), whose flow rate is set to match the demand of the downstream vaporizer. The vent accommodates the difference between PUMP-1, which controls the melt rate, and PUMP-2, which controls the vaporization rate. Water flows through 2 and 1 µm in-line filters in series to restrict the flow of particulates into the vaporizer. PUMP-2 is also preceded and followed by electronic pressure sensors PI-1 (Elveflow PS3-Small) and PI-2 (Elveflow PS4-Small) to monitor injection pressure conditions and pump and filter performance. Typically, the pressurized dry air entering the vaporizer adds back pressure on the liquid sample injection line, which damps the cyclic pressure fluctuations of the peristaltic pump and stabilizes flow into the vaporizer. The system also includes a flow valve (FV-1) that can be used to adjust the back pressure on PUMP-2 before making a measurement.

At the vaporizer, filtered sample water is mixed and heated with dry air to produce a constant-humidity stream of vaporized sample. Immediately before entering the vaporizer, the liquid sample line is reduced to a 100 µm fused silica capillary tube. The 100 µm capillary provides sufficient flow restriction that is important for efficient vaporization while also performing well for periods of several days without clogging. The custom vaporizer includes a 0.50 mm internal diameter tee heated to 170 °C using a PID-controlled resistance heater cartridge, similar to Gkinis et al. (2010, 2011). The vaporizer combines pressurized dry air with liquid sample, and it is set within an aluminum enclosure that is lined with 3.175 cm of calcium silicate insulation. After the sample is vaporized, the vapor is drawn into the optical cavity where it is measured, and excess vapor is vented into the laboratory. Vapor is carried from the vaporizer to the optical cavity within insulated tubing to prevent condensation.

2.3 Design choices to mitigate memory effects

Design choices for the CFA system are intended to reduce and characterize the memory between measurements. Because our automated selector valve is positioned immediately after the ice-core melt head, reference waters pass through all components of the sample handling system except the melt head and its tubing; by design, the mixing length expected between measured ice-core layers with differing isotopic compositions can be approximated by the mixing length represented by transitions in reference waters if all other system conditions are identical. Mixing length within the system is reduced by increasing the flow velocity and therefore

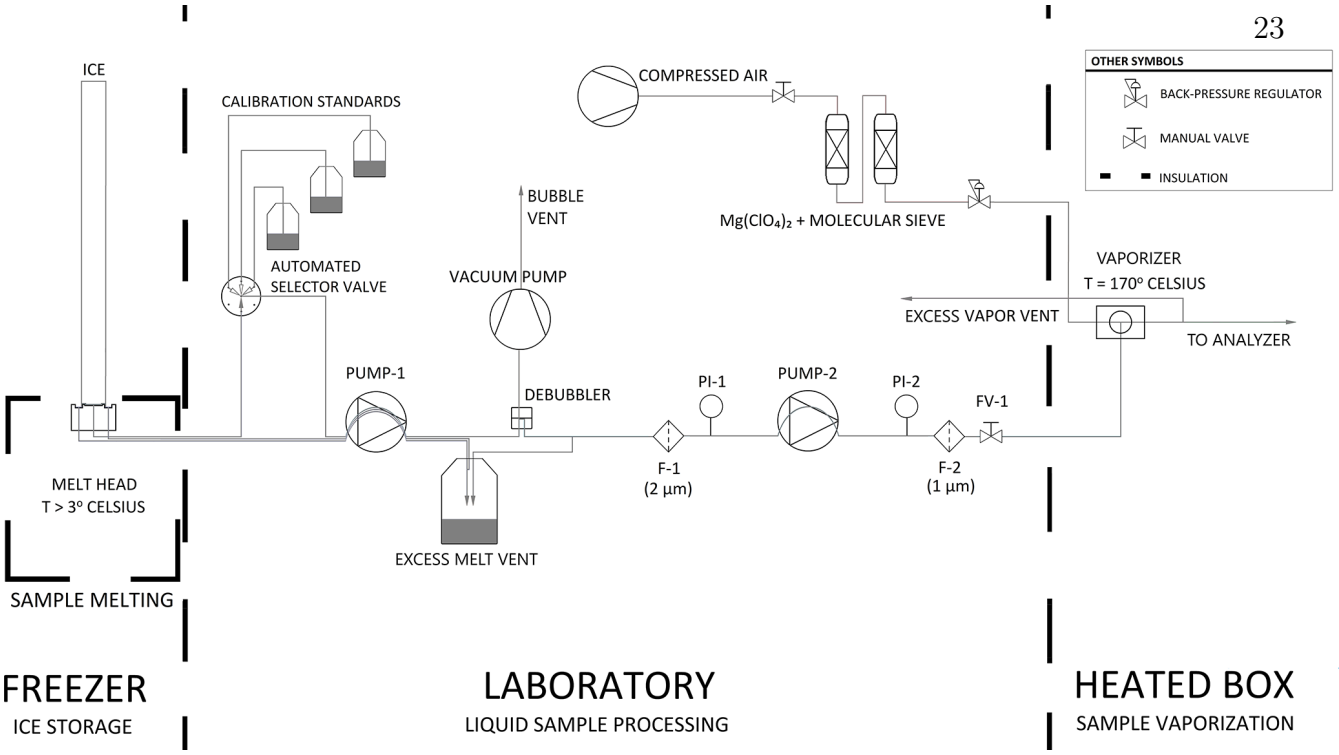

Figure 1. Process flow diagram of the CFA system. Thick dashed lines indicate transitions between temperature-controlled process spaces. Note that F-1 and F-2 are filters, PI-1 and PI-2 are pressure sensors, and FV-1 is a flow valve.

limiting the sample retention time in two ways: overall sample handling system volume and tubing diameters are minimized where possible, and excess sample volume is drawn through the entire system during ice-core analysis. Approximately 6 times more water is handled by PUMP-1 than is sent by PUMP-2 into the vaporizer; excess liquid volume is vented before PUMP-2. Similarly, approximately 30 times more vapor is generated than is analyzed; excess vapor is driven by the differential between PUMP-2 and the L2140-*i* inlet pump, and it is vented to laboratory air immediately before vapor enters the optical cavity. In this way, the liquid and vapor tubing is flushed with many times more sample volume than is required for analysis.

3 CFA–CRDS operations and measurements

We designed an operational sequence for reference water and ice-core measurements during a period when lab work was intermittent due to the COVID-19 pandemic. The CFA system was configured to automatically measure an alternating sequence of three in-house reference waters over a period of approximately 7 weeks; reference waters included Seattle tap water (SW2), West Antarctic Ice Sheet Divide snow (CW), and South Pole snow (SPS2), as shown in Table 1 and indicated in Fig. 2. Measuring reference waters continuously allows us to explore the long-term changes in system calibration while also informing maintenance requirements over long timescales. When available, an operator prepared and measured an ice-core section between reference water measurements. The need for frequent calibration of CRDS data for $\Delta^{17}O$ has been well documented (e.g., Schauer et al., 2016), and continuous reference water measurements ensured that there were calibration data available adjacent in time to each intermittent ice-core analysis.

We operated the CFA–CRDS system to measure nine repeated sections of an ice core and a repeated sequence of internal reference waters that we used to calibrate the ice-core measurements. We also measured a replicate ice-core section by discrete CRDS for comparison. Repeated reference water measurements are used to develop a calibration for the ice-core data. We compare our calibrated CFA–CRDS $\Delta^{17}O$ data with the discrete measurements to evaluate this method.

3.1 Operational considerations to maintain efficient vaporization

Because the vaporizer is sensitive to small fluctuations in sample flow rate, a careful balance of system pressures is required to control sample flow (Gkinis et al., 2010, 2011); specifically, the pressure of the sample at the vaporizer inlet must be slightly greater than the pressure of the dry air within the vaporizer. Maintaining a balance between the air pressure and sample pressure within the vaporizer requires

Table 1. Isotopic values of reference waters. SW2 is Seattle deionized tap water, CW is melt water from the WDC06A core (i.e., West Antarctic Ice Sheet precipitation), and SPS2 is South Pole snow. These three waters were normalized to the VSMOW-SLAP scale using other in-house reference waters that were analyzed against VSMOW, SLAP, and GISP. The calibrated $\delta^{17}O$ values are calculated from the combination of $\Delta^{17}O$ and $\delta^{18}O$ and are therefore reported to four significant digits (see Schoenemann et al., 2013, for additional details).

Reference water (origin location)	$\delta^{17}O$	$\delta^{18}O$	δD	d	$\Delta^{17}O$
	‰ vs. VSMOW				per meg vs. VSMOW
SW2 (Seattle)	−5.7107	−10.85	−77.96	8.84	33
CW (West Antarctica)	−17.8807	−33.64	−265.95	3.17	25
SPS2 (South Pole)	−25.1210	−47.07	−365.20	11.36	15

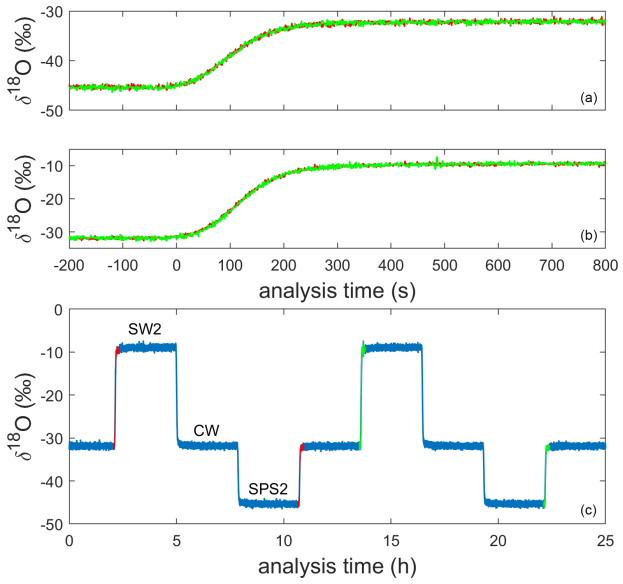

Figure 2. Uncalibrated 1 Hz measurements of $\delta^{18}O$ for the alternating sequence of reference waters during a full analysis day **(c)**. The 200 s preceding and 800 s following four reference water transitions are shown in the other panels; two transitions (shown in orange and green) from SPS2 to CW are stacked in panel **(a)** and two transitions from CW to SW2 are stacked in panel **(b)**.

knowledge of both pressure conditions. We monitor pressures at PI-1 and PI-2 so that it is possible to diagnose the source of system pressure changes when they occur; we also fix the pressure of the dry air line with the back pressure regulator (typically 200 kPa). Vacuum conditions at PI-1 indicate particulate loading across the filter screen at F-1; the filter screen will clog over time, and if the filter screen is not replaced, suction from the inlet of PUMP-1 can draw a vacuum at PI-1. Vacuum conditions at PI-1 can impact the downstream peristaltic pump (PUMP-2) performance, ultimately causing inconsistent flow into the vaporizer and analyzer. Under optimal analysis conditions, the pressure is near ambient at PI-1. A decrease in pressure at PI-2 indicates upstream vacuum conditions or worn peristaltic pump tubing at PUMP-2. An increase in pressure at PI-2 indicates clogging downstream, which can occur as particulate loading within F-2 or as mineral precipitation within the capillary or vaporizer. The pressure at PI-2 generally varied between 200 and 400 kPa, depending on the injection air pressure and the precipitate levels within the vaporizer or capillary tubing. High-pressure vaporizer conditions allow sample to flow despite the inevitable accumulation of precipitate within the vaporizer, which enables the system to operate in balance for days or even weeks. However, over time, precipitate accumulation within the vaporizer can restrict the flow of air, water, or both; this typically requires re-balancing of system flow conditions, but it can occasionally require removing and cleaning the vaporizer fittings with soap, water, and physical agitation.

During operation of the CFA–CRDS, intermittent reductions in water vapor concentration can occur within the vaporizer, which can produce perturbations in the isotope data. Gkinis et al. (2010, 2011) described sample flow inconsistencies at their CFA flash vaporizer that caused extreme outliers in isotope data, though the cause of the fluctuations was unclear. We observe similar fluctuations, and the pressure sensor data provide insight into their cause. We find that the most common causes of such variations are microbubbles entering the vaporizer owing to particulate loading, which can cause poor debubbler performance and can also cause blockages to form within the small tubing fittings. Microbubbles that remain suspended in the fluid stream after the debubbler cause volumetric flow rate reductions at the vaporizer inlet. Blockages within fittings upstream of PUMP-2 can cause extreme vacuum conditions before the pump (i.e., pressure observations associated with blockages were as low as −140 kPa before PUMP-2 instead of the typical ambient conditions); this can lead to the contamination of system tubing with small bubbles that also cause temporary flow reductions. To avoid these inconsistencies, we find that it is important to periodically clean the debubbler unit and to maintain ambient pressure at the PUMP-2 inlet by replacing clogged filter screens or tubing fittings. Although data outliers could be systematically removed (as done in Gkinis et al., 2011), occasional bubbles do not substantially impact the isotopic mean value of our ice-core measurements and are retained here. We do exclude some reference-water calibration data, where bubble

interruptions are most frequent due to limited operator oversight during the automated reference water measurements. Calibration measurement criteria are discussed in Sect. 3.4.

In addition to monitoring pressure evolution across the system, we can also observe the quality of vapor at the CRDS analyzer via characteristic patterns that arise in the CRDS data. Specific patterns in water vapor concentration and $\delta^{18}O$ that emerge from unstable flow into the vaporizer are shown in Fig. 3. We observe that pulsating flow conditions can cause incomplete vaporization, identified by anticorrelated fluctuations in water vapor concentration and $\delta^{18}O$. When a pulse of water overwhelms the vaporizer, the isotopic composition becomes lighter as $H_2^{16}O$ preferentially evaporates into the vapor stream; as the vaporizer dries out between pulses, the isotopic composition becomes heavier, exhibiting an evaporation signal. Pulsating flow conditions are caused by pressure fluctuations from the peristaltic pump (> 70 kPa) when insufficient back pressure is applied on PUMP-2. The resulting patterns have a large amplitude (up to 10 000 ppm for water vapor and several ‰ for $\delta^{18}O$) and a frequency that mirrors that of the peristaltic pump (e.g., Fig. 3a). The observed fractionation that occurs during these vaporization conditions leads to large calibration bias for $\Delta^{17}O$, causing errors of tens to hundreds of per meg. If there is sufficient back pressure at PUMP-2, the pressure readings at PI-2 are typically < 40 kPa. We attribute small fluctuations in $\delta^{18}O$ that are anticorrelated with water vapor concentration to the incomplete vaporization of individual droplets (e.g., Fig. 3b). Because inconsistent flow into the vaporizer can cause isotope fractionation and because it is important to measure calibration standards under the same conditions as the ice-core samples, we tune the system to maintain steady pressure readings at the vaporizer inlet prior to calibration standard and ice-core analysis, as discussed in Sect. 3.2; vapor concentration data that are typical of a well-maintained CFA system are shown in Fig. 3d.

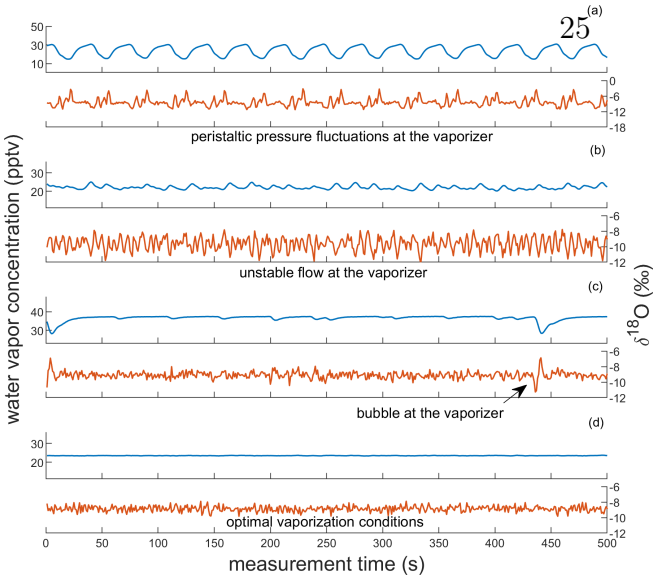

Figure 3. Observations of vapor quality as real-time indicators of vaporizer performance. Each panel shows corresponding observations of water vapor concentration and $\delta^{18}O$ of SW2, reported in parts per thousand vapor (pptv) and ‰, respectively. Panels **(a)** and **(b)** show observations indicative of imbalanced vaporizer conditions for large and small pressure imbalances, respectively. Panels **(c)** and **(d)** show observations indicative of acceptable vaporizer performance. Though both include low-variability observations of $\delta^{18}O$ ($\sigma < 0.3$ ‰) and of water vapor concentration, **(c)** also includes microbubble interruptions at the vaporizer (e.g., at 5 and 440 s). Panel **(d)** indicates optimal vaporizer performance. Note that the vertical scaling of **(a)** is different from the other panels.

3.2 Measuring $\Delta^{17}O$ by CFA–CRDS in ice-core samples

Approximately 12 to 24 h before making an ice-core measurement, an operator maintained the CFA system to balance the flow rate into the vaporizer. For example, when indicated by anomalously high or low pressure sensor data, the filter screens, peristaltic pump tubing, or capillary tubing were replaced. When indicated by CRDS data trends as in Fig. 3, the vaporizer components were cleaned. Returning the CFA system to a balanced state before making measurements of all reference waters increases the likelihood of having usable, high-quality calibration data against which to calibrate the ice-core samples. At other times when ice-core measurements were not made, the system occasionally drifted out of balance and was not actively maintained such that some of the reference water measurements are of lower quality than those used to calibrate the ice-core measurements. This is discussed in more detail in Sect. 3.4.

We cut an 87.5 cm ice-core sample from ~ 92 m depth beneath the surface at Summit, Greenland, into nine 26 mm square slices to prepare them for continuous analysis. After preparing these nine CFA sticks, a 10th section of core was cut into 63 discrete depth intervals. Discrete ice samples were melted in sealed polyethylene sample bottles in a refrigerator at 4 °C. We measured the 87.5 cm section of ice 10 times: the nine replicate slices were measured by the CFA–CRDS configuration described above, and the 10th measurement was made by a discrete injection of 63 melt samples from the core using the commercially available vaporizer unit (Picarro p/n A0211) and automated injections as in Schauer et al. (2016). The depth resolution of the discretely measured ice is 1.39 cm.

For all CFA measurements, we made visual observations of the core height to monitor the melt rate during analysis, then later assigned a high-resolution depth equivalent for each analysis time that is based on the value of $\delta^{18}O$ and the measured depth of discrete samples. Previous work has monitored core depth with electronic distance meters (e.g., Bigler et al., 2011; Jones et al., 2017a), and such measurements are

critical for depth registration for routine CFA measurement campaigns. Here, we forego electronic depth registration and instead adjust initial depth estimates for each core section by aligning the seasonal cycle of $\delta^{18}O$ for all core samples. Assigning depths by aligning the $\delta^{18}O$ variations should largely eliminate depth-registration errors, since the strong seasonal $\delta^{18}O$ variations must be essentially identical in each replicate sample, and the signal-to-noise ratio for $\delta^{18}O$ is very high. Summit, Greenland, has a modern annual accumulation rate of 24 ± 5 cm (ice equivalent) per year (Meese et al., 1994; Dibb and Fahnestock, 2004; Hawley et al., 2008, 2020), and we expect to see 2 to 3 years represented by the core sample that we measured in replicate (Hastings et al., 2009). We compressed the timescale of each CFA time series to maximize the cross-correlation of $\delta^{18}O$ ($0.93 < r < 0.99$) between the CFA measurements and the discrete measurements. We then assigned each CFA time a depth equivalent based on the depth of the corresponding discrete $\delta^{18}O$ data. We note that the amplitude of the seasonal variations in $\delta^{18}O$ is somewhat compressed in the lower ~ 30 cm of this core sample, so the depth designations for this interval are likely a greater source of error than in the rest of the ice. Nevertheless, we are confident that our depth registration is precise to within 1 cm or better, determined by assessing the variance in depth assignments at inflection points.

3.3 Operational choices to mitigate memory effects

Mitigating memory effects is important for both ice-core and reference water measurements; in addition to the design choices highlighted in Sect. 2.3, there are several operational choices that were made to reduce the memory between isotopically distinct waters. For example, increasing the pump rates at PUMP-1 during ice-core analysis should drive shorter retention times within the tubing upstream of the liquid vent, which should reduce system mixing. In this way, the transition times for reference waters (shown in Fig. 2) are a conservative estimate of mixing effects. The transition time between measurements of reference waters generally varied between 180 and 360 s. We therefore assume a conservative mixing time of 360 s during reference water transitions, and we ignore the 360 s that initiate and conclude each reference water measurement. Before measuring each section of ice (which is typically ~ 1 m long), we also condition the system with at least 10 min of water with similar isotopic composition to prevent mixing between isotopically disparate reference waters and ice-core samples at the beginning of the analysis. Finally, the replicate CFA–CRDS measurements that are the focus of this study provide a practical evaluation of the effects of memory on measurement fidelity in this configuration.

3.4 Calibrating CFA–CRDS $\Delta^{17}O$ data

26

To achieve an accurate calibration, similar treatment of reference waters and sample melt during vaporization is critical. For this study, we measured the calibration standards immediately before and after measuring an ice-core section; this ensures the most comparable treatment of reference waters and sample melt. Achieving similar treatment also requires that the system is stable during the entire measurement period, including reference water measurements and ice sample measurements. Because an individual ice-core measurement takes a few hours at the melt rates that we employ, we limit our reference water measurements to 3 h each to increase the likelihood that the complete sequence of reference waters and ice-core samples is measured under similar CFA and CRDS conditions.

To calibrate our measurements, we create a two-point linear calibration from the nearest measurements of our internal reference waters, SW2 and SPS2; a third reference water (CW) is used as an independent verification of the calibration. The values of SW2, CW, and SPS2 have been measured independently and are normalized to the VSMOW-SLAP scale as in Schoenemann et al. (2013). An alternating sequence of the three reference waters was measured between ice core analyses; the selector valve was programmed to automatically switch between the reference water containers every 3 h. Automated reference water measurements were typically unsupervised. Reference water measurements were automated and typically unsupervised. Because measurement conditions evolve over time due to particulate loading and mineral precipitation within the CFA components and because there were periods of time during the analysis window when no operator was available to monitor system conditions, there were periods of time during which the water vapor concentration was outside the ideal range, during which large bubbles or other flow inconsistencies degraded the quality of reference water data, or during which the CFA system was not operating; consequently, only about 50 % of the data within the study period is included in this analysis, as described below and in Table 2. We automatically reject calibration data and measurements of CW that were generated from water vapor concentrations beyond the targeted range (i.e., $< 20\,000$ or $> 50\,000$ ppm) or data with insufficient vaporizer operations, indicated by $\sigma_{\delta^{18}O} > 0.5$ ‰ across the measurement window. Typical variability of water vapor concentration within a single 3 h period is 0.5 % to 5 %. We identify transitions from one reference water to the next in the data by the second derivative of δD and assign known standard values based on the uncalibrated measurement values of δD. We include measurements of SW2 and SPS2 that contain at least 6000 s of analysis time, and we trim 360 s of data from the beginning and end of each measurement interval to avoid memory effects. The mean and standard deviation of the analysis time for calibration standard data are 9350 ± 660 s. To calibrate all ice-core and CW measure-

Table 2. Sequence of CFA–CRDS measurements, including calibration information and calibration offset determined by Eq. (5) for 1.39 cm resolved data. Note that the long reference water measurement of SW2 used to generate Fig. 7 was made on 18 September 2020. Also note that none of the reference water measurements on 8 September were acceptable to use for calibration and that the large calibration offset for this measurement may be attributed to instrument drift or a change in CFA conditions between 8 and 9 September. Notable flow instabilities led to vaporizer cleaning on 14 September and 8 October 2020, and no measurements were made between 27 September and 8 October 2020.

JEMS2 (91.28–92.15 m) measurement date	SW2, CW, SPS2 measurement date	m_{17} (unitless)	m_{18} (unitless)	b_{17} (‰)	b_{18} (‰)	Δ^{17}O offset (per meg)
1 September 2020	1 September 2020	1.0163	1.0068	4.5250	−1.6133	−13
1 September 2020	2 September 2020	1.0094	0.9999	4.4551	−1.6766	−9
2 September 2020	2 September 2020	1.0094	0.9999	4.4551	−1.6766	−6
4 September 2020	4 September 2020	1.0089	0.9996	4.4396	−1.6892	1
8 September 2020	9 September 2020	1.0132	1.0040	4.5910	−1.5211	−25
15 September 2020	15 September 2020	1.0065	0.9971	4.2982	−1.9084	8
25 September2020	25 September 2020	1.0058	0.9966	4.4130	−1.6878	19
9–10 October 2020	10 October 2020	0.9983	0.9908	4.2542	−1.8581	9
10 October 2020	10 October 2020	1.0054	0.9967	4.4621	−1.5888	5

ments made during this study, we use 47 continuous 3 h measurements of SW2 and 40 continuous 3 h measurements of SPS2. All analyses include measurements for δ^{17}O, δ^{18}O, and δD. Calculations of d and Δ^{17}O were obtained from the calibrated δ values as given in Eqs. (1) and (2), respectively. Calibration for Δ^{17}O is more completely described below.

The calibration data used for all measurements are generated from adjacent measurements of SW2 and SPS2 that meet the screening criteria above; calibration data and the sequence of CFA–CRDS measurements are provided in Table 2. For each calibration of CW or ice-core data, we employ the nearest measurements of SW2 and SPS2 for the calibration. The calibration is performed separately for δ^{17}O and δ^{18}O: using a least-squares approach, we fit a linear equation to the uncalibrated average measurements so that the calibrated SW2 and SPS2 measurements match their known values. The calibration equation therefore becomes

$$\delta_{\text{calibrated}} = m \times \delta_{\text{uncalibrated}} + b, \tag{3}$$

where δ represents either δ^{17}O or δ^{18}O. An account of m and b for both δ^{17}O and δ^{18}O is shown for all measurements in Table 2. Finally, Δ^{17}O is calculated from the calibrated values of δ^{17}O and δ^{18}O:

$$\Delta^{17}\text{O}_{\text{calibrated}} = \ln\left(\delta^{17}\text{O}_{\text{calibrated}} + 1\right) - 0.528 \ln\left(\delta^{18}\text{O}_{\text{calibrated}} + 1\right). \tag{4}$$

The mean and standard deviation of all CW measurements of Δ^{17}O during the analysis period are 25 ± 12 per meg ($n = 53$). The subset of CW measurements with the most consistent CFA operations – and therefore the lowest variability for δ^{18}O ($\sigma < 0.06$ ‰) – had corresponding Δ^{17}O values of 25 ± 6 per meg ($n = 36$). Low variability among reference water measurements gives confidence in the use of this system for this study of replicate ice-core measurements.

3.5 Processing CFA–CRDS Δ^{17}O data

After assigning approximate depth values and calibrating the ~ 1 Hz data, we discretize the CFA–CRDS data by binning the calibrated data into prescribed depth intervals and averaging across the entire interval. This enables a direct comparison between the continuous CFA–CRDS time series and the discrete CRDS measurements. Small differences in the instantaneous melt rate cause some variability in the data-averaging duration for each reported measurement; the typical instantaneous melt rate was ~ 0.3 cm min^{-1}, but rates ranged from ~ 0.1 to ~ 0.4 cm min^{-1} during analysis. We report our CFA–CRDS measurements with 1.39 cm resolution to match the resolution of our discrete CRDS measurements. We also explore the effects of depth resolutions that range from 0.5 to ~ 40 cm, given that increasing the averaging window of the ~ 1 Hz spectroscopic measurements reduces instrumental noise (e.g., Werle et al., 1993; Gkinis et al., 2010, 2011; Steig et al., 2014, 2021; Schauer et al., 2016; Jones et al., 2017a).

4 Results and analysis

Our isotope measurements capture a period of approximately 2 years of precipitation, as expected for a Greenland ice core from the depth we analyzed (discussed in Sect. 3.2). The seasonal cycle of δ^{18}O is shown in Fig. 4. We estimate that our depth assignments are accurate to < 7 mm throughout the core by determining the variability in depth assignments at all inflection points; this allows us to compare CFA–CRDS measurements of Δ^{17}O at the $\sim$cm scale, an appreciably finer resolution than has previously been reported. Our comparison quantifies the reproducibility of our measurements and identifies sources of variability among these CFA–CRDS Δ^{17}O data.

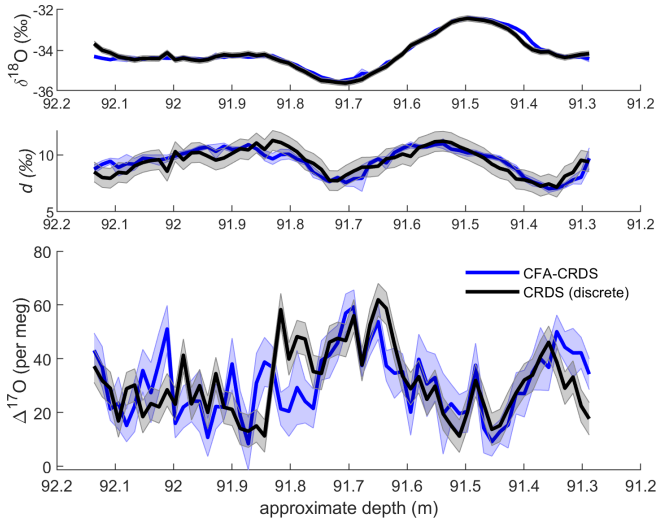

Figure 4. Comparison of discrete CRDS ice-core measurements (black) with calibrated CFA–CRDS data averaged over 1.39 cm intervals (blue). Corresponding δ^{18}O and d data are shown for seasonal context. Discrete CRDS measurements are shown with the root mean square error of corresponding reference water measurements (grey shading), and CFA–CRDS measurements are shown as the mean of nine measurements with the standard error (blue shading). Note that δ^{18}O and d are reported in ‰ and that Δ^{17}O is measured in per meg; each vertical axis uses different scaling.

4.1 Seasonal Δ^{17}O variations in replicated CFA and discrete measurements

We compare our CFA–CRDS data for Δ^{17}O with discrete CRDS measurements to evaluate the CFA–CRDS method. We present the mean value and standard error of all replicate measurements in Fig. 4 with 1.39 cm averaging (representing approximately 270 s of data per interval for each individual CFA–CRDS replicate); Fig. 4 also shows the discrete CRDS measurements with the root mean square error of the corresponding discrete reference water measurements. The mean of all CFA–CRDS measurements (representing more than 2000 s of data per interval) is well correlated with the discrete measurements ($r = 0.52$, where $0.28 \leq r \leq 0.69$ with 95 % confidence), especially in the upper 50 cm of the core ($r = 0.74$, where $0.54 \leq r \leq 0.88$ with 95 % confidence). Both the CFA–CRDS data and the discrete CRDS data show clear seasonal Δ^{17}O variations at this measurement resolution that are matched in magnitude and timing.

4.2 Error attribution for CFA–CRDS Δ^{17}O measurements

Next, we characterize the variability observed among our nine CFA–CRDS measurements. In addition to the depth alignment errors discussed above, sources of variability introduced by the CFA–CRDS method may include high-frequency instrumental noise, calibration errors, and smoothing or bias generated by mixing within the CFA system. High-frequency, high-amplitude noise (~ 1 ‰) in the uncalibrated CRDS data is inherent to the instrument and can cause large aberrations from the true value of Δ^{17}O, especially over short averaging times; long averaging times (> 1000 s) are typically used when measuring Δ^{17}O by CFA–CRDS to minimize instrumental noise. Calibration errors in Δ^{17}O occur when measurement treatment differs between calibration standards and samples or between calibration standards; this can cause fractionation to occur in the uncalibrated δ^{17}O and δ^{18}O measurements, leading to biased calibration slope and intercept information. Despite efforts to stabilize vaporizer system conditions prior to ice-core sample analysis and to measure ice-core samples with the same treatment, it is likely that some calibration errors persist in our ice-core data because it is not possible to measure the standards and the sample at the same time. Finally, CFA measurement error for Δ^{17}O may result from mixing isotopically distinct waters during CFA processing or from other processing issues that affect the internal variability (i.e., perceived seasonality) of the continuous ice-core measurement.

Typical CRDS characterization studies have used repeated measurements of reference waters to identify measurement error; for this study, we instead use repeated measurements of an ice core to characterize the sources of the measurement error. By measuring reference waters, it is possible to approximate the precision of the uncalibrated measurements by determining the effect of averaging time on the intrinsic noise of the measurement; it is also possible to quantify the variance of the calibrated, averaged data. Our best data for CW were measured at 25 ± 6 per meg, but without additional information, it is not straightforward to identify whether the error associated with this measurement is caused by instrumental limitations, calibration bias, or other CFA processing effects. Our replicate CFA–CRDS measurements provide an opportunity to identify the source of CFA–CRDS errors because we can separately analyze the variability internal to each time series (e.g., due to the seasonal cycle of Δ^{17}O or due to CFA errors) and the variability between the mean values for each ice-core replicate (e.g., due to calibration offsets); further, we can compare this variability with instrument expectations at different averaging times

To isolate the error imparted by the calibration strategy, we processed the data in two ways: first, we calibrated the data as described in Sect. 3.4, and second, we set the mean values of all calibrated CFA measurements equal to the mean value of the discrete CFA measurements in order to consider only the variability internal to each measurement. Steig et al. (2021) demonstrated that making a linear adjustment to the calibration intercept for δ^{17}O and δ^{18}O could reduce the noise of their CFA–CRDS measurements for Δ^{17}O in the SPC14 core. They exploited additional reference water information taken before or after the CFA measurement to define an adjusted calibration intercept value. Here, we can instead use the mean value of the CFA–CRDS measurements

themselves, further eliminating uncertainty around this correction by setting the mean of each calibrated CFA–CRDS time series equal to the mean value of our discrete ice-core measurements; in this way, we are able to eliminate offsets in calibration and examine the variability within each continuous measurement. We define the calibration-adjusted $\Delta^{17}O$ data as below:

$$\Delta^{17}O_{\text{adjusted CFA}} = \Delta^{17}O_{\text{calibrated CFA}} + \frac{1}{n} \times \sum_{i=1}^{n} \Delta^{17}O_{\text{calibrated discrete}}(i) - \frac{1}{n} \times \sum_{i=1}^{n} \Delta^{17}O_{\text{calibrated CFA}}(i), \quad (5)$$

where the value of n, which represents the number of data points per meter, varies as a function of the depth resolution.

The calibration offset error is therefore $\Delta^{17}O_{\text{adjusted CFA}} - \Delta^{17}O_{\text{calibrated CFA}}$. Equivalently, $\Delta^{17}O_{\text{adjusted CFA}}$ can be expressed in terms of $\delta^{17}O$ and $\delta^{18}O$ using calibration correction information that is based on the differences between average $\delta^{17}O$ and $\delta^{18}O$ values for the discrete and continuous datasets. That is,

$$\Delta^{17}O_{\text{adjusted CFA}} = \ln\left(m_{17} \times \delta^{17}O_{\text{uncalibrated CFA}} + b_{17} + b_{17\_\text{corr}} + 1\right) - 0.528 \ln\left(m_{18} \times \delta^{18}O_{\text{uncalibrated}} + b_{18} + b_{18\_\text{corr}} + 1\right), \quad (6)$$

where the correction values b_{17_corr} and b_{18_corr} are defined by the difference in mean δ for CFA and discrete measurements. This calibration adjustment method is analogous to that used in Steig et al. (2021).

Evaluating both $\Delta^{17}O_{\text{calibrated CFA}}$ and $\Delta^{17}O_{\text{adjusted CFA}}$ allows us to disentangle the calibration offset error from other sources of measurement error. We discretized the CFA–CRDS data to a series of depth-resolution schemes that ranged from 1.39 to 43.75 cm; the data are provided for three different depth resolutions in Fig. 5. We calculated the standard error for all depth intervals across all measurement resolutions. The total error for the $\Delta^{17}O_{\text{calibrated CFA}}$ and the error for the $\Delta^{17}O_{\text{adjusted CFA}}$ are approximated by the blue and red lines in Fig. 6, respectively. The region between the two solid lines is the fraction of the total error that can be attributed to the calibration offset. Figures 5 and 6 indicate that the calibration offset noise is essentially indistinguishable from the instrumental noise at short averaging times, so the calibration offset adjustment does little to improve the measurement for the best-resolved data. The results show that the total error is < 10 per meg for all data. The total error is ~ 5 per meg at averaging times longer than ~ 3000 s, which corresponds to depth averages of ~ 15 cm at the melt rates we used. Figure 6 also shows that the error that arises from differences in internal variability (i.e., the CFA error) for the CFA–CRDS data is < 2 per meg by ~ 3000 s and that the total error is dominated by calibration offset error at long averaging times.

Finally, we directly compare the variability of our CFA–CRDS data with the variability of reference waters measured by CFA–CRDS, which is determined by an Allan variance analysis. An Allan variance analysis quantifies the relationship between signal noise and integration time (Allan, 1966; Werle et al., 1993); for CRDS data, this analysis of reference water measurements is commonly used to approximate the measurement precision of the system for any given measurement duration (Gkinis et al., 2010; Steig et al., 2014). We determine the Allan deviation (square root of the Allan variance) from a long continuous analysis (~ 8.5 h) of the SW2 reference water made during our analysis window (see Table 2); the result is shown in Fig. 7. Differences between the Allan deviation and the standard deviation of our measurements should confirm whether the magnitude and timing of the variability are as precise as during reference water measurements, or if there are other changes imparted by the CFA system or calibration that may degrade CFA–CRDS data quality. We find the standard deviation $\sigma_{\text{calibrated\_CFA}-\Delta^{17}O}$ among all nine $\Delta^{17}O_{\text{calibrated CFA}}$ datasets averaged over integration windows that vary from 5 mm to 43.75 cm. This analysis compares the variability of the final, calibrated measurements along the depth of the core sample with the variability of the reference water measurement, and ultimately quantifies the reproducibility of our CFA–CRDS measurements. We track the analysis time associated with each averaging interval and overlay the measured $\sigma_{\text{calibrated\_CFA}-\Delta^{17}O}$ with the corresponding mean integration time for each depth interval on Fig. 7a.

Figure 7a shows generally good agreement between $\sigma_{\text{calibrated\_CFA}-\Delta^{17}O}$ and $\sigma_{\text{Allan}-\Delta^{17}O}$ at integration times less than 400 s, but the $\sigma_{\text{calibrated\_CFA}\Delta^{17}O}$ data asymptotically approach a limit of 10 per meg at longer averaging times instead of following the stability trend expected by the Allan variance analysis. To evaluate to what extent this mismatch between expected and observed σ can be attributed to errors arising from the calibration offset (as shown in Fig. 6), we repeat this analysis for the $\Delta^{17}O_{\text{adjusted CFA}}$ data. Figure 7b shows excellent agreement between $\sigma_{\text{adusted\_CFA}-\Delta^{17}O}$ and $\sigma_{\text{Allan}-\Delta^{17}O}$at all integration times; this demonstrates that the drift in $\sigma_{\text{calibrated\_CFA}-\Delta^{17}O}$ shown in Fig. 7a can be entirely attributed to calibration effects and not to the CFA process directly. Figure 7 suggests that reducing the error of calibrated CFA–CRDS measurements is not limited by the CFA process – nor by the CRDS instrument – but rather by the quality of the calibration information, which depends on the treatment and frequency of reference water measurements.

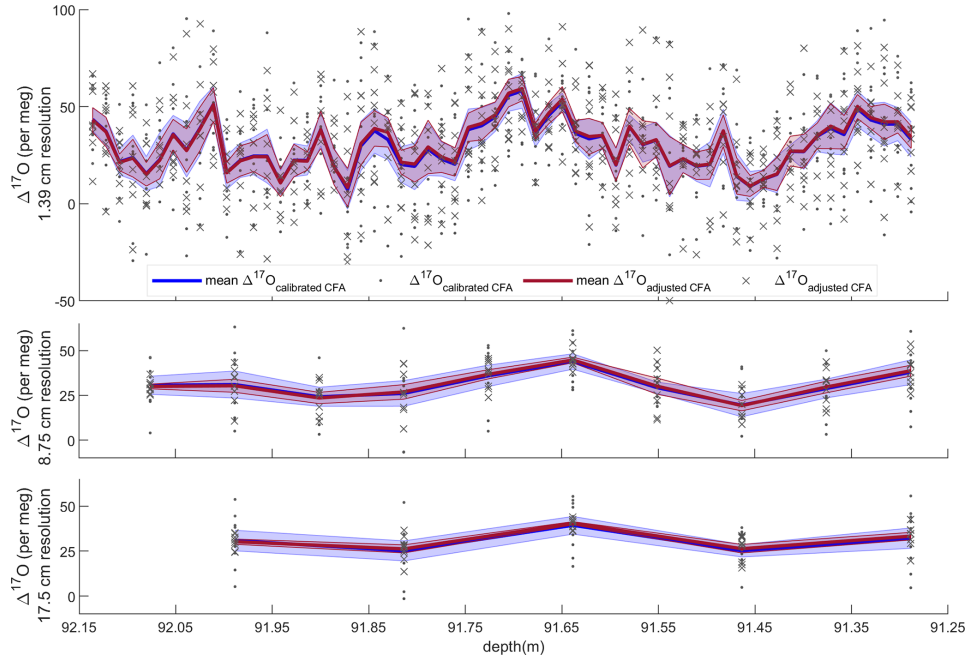

Figure 5. Average $\Delta^{17}O$ with standard error and all CFA–CRDS measurements, shown for three different depth resolutions. Dots and blue error envelopes indicate $\Delta^{17}O_{\text{calibrated CFA}}$, and X symbols and red error envelopes indicate $\Delta^{17}O_{\text{adjusted CFA}}$. All data are plotted at the upper depth of the depth interval that they represent. Note that the upper panel is expanded such that all three vertical scales are identical.

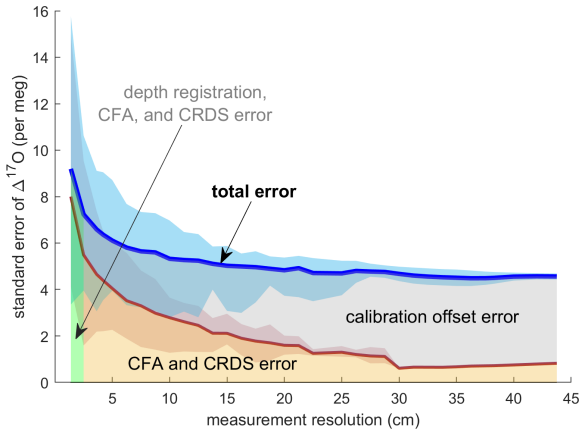

Figure 6. Standard error of all replicate CFA measurements as a function of measurement integration depth. The blue line shows the mean of the standard error of $\Delta^{17}O_{\text{calibrated CFA}}$ as calculated for each depth interval; the shaded blue area indicates the minimum and maximum values of the standard error across all depth intervals. The red line and shaded area show the relationship between the standard error in $\Delta^{17}O_{\text{adjusted CFA}}$ and the measurement resolution. The area beneath the total error line is highlighted to indicate error attribution.

5 Discussion and conclusions

5.1 Comparison of CFA–CRDS $\Delta^{17}O$ measurements with other $\Delta^{17}O$ measurements from Greenland

Our work complements previous studies that have examined the seasonal cycle of $\Delta^{17}O$ in the polar regions, and good agreement with earlier work validates our measurements. Consistent with previous measurements from Greenland, the $\Delta^{17}O$ signal in our data is anticorrelated with d and anticorrelated with the seasonal cycle in $\delta^{18}O$ (Landais et al., 2008). The measurements presented here were made from a core that represents approximately 2 years of ice accumulation from the 1760s (Hastings et al., 2009). The measured magnitude (peak to trough) of the seasonal cycle in $\Delta^{17}O$ is $\sim$ 45 per meg at 1.39 cm resolution in our data (Fig. 4), which is in excellent agreement with the magnitude of the seasonal cycle reported previously for Greenland. Specifically, Landais et al. (2012b) reported seasonal magnitudes of $\sim$ 25 per meg from a shallow firn core at NEEM (in northwestern Greenland) that represented accumulation periods between 1962–1963 and between 2003–2005; when we coarsen our measurement resolution to 3.6 cm – which approximates the $\sim$ monthly (5 cm) measurement resolution in the NEEM core (detailed in Steen-Larsen et al., 2011) – the magnitude of the seasonal cycle in our data is $\sim$ 30 per meg. Low errors between replicate values and the good agreement with previous studies strengthen confidence in the CFA–CRDS approach for high-resolution $\Delta^{17}O$.

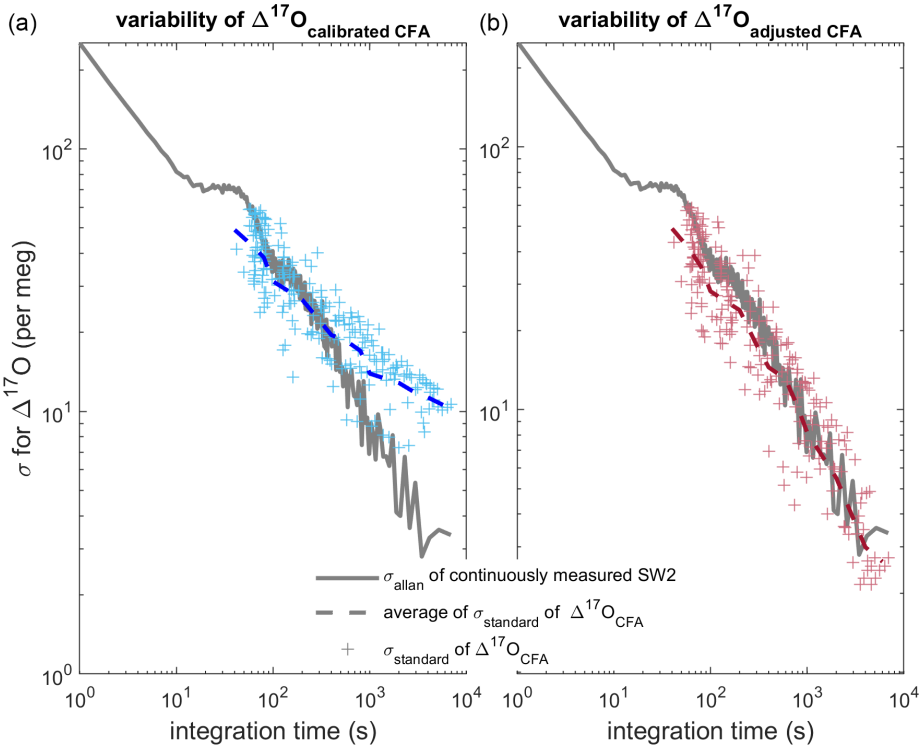

Figure 7. Comparison of Allan deviation of continuous reference water measurements and standard deviation of nine duplicate CFA ice-core measurements. In both panels **(a)** and **(b)**, the Allan deviation line (solid grey) for a long measurement of SW2 is overlain by the standard deviation of the CFA–CRDS ice-core measurements (crosses) and the mean of the standard deviations for each integration time (dashed line). The $\Delta^{17}O_{calibrated\,CFA}$ and $\Delta^{17}O_{adjusted\,CFA}$ data are shown in blue and red similarly to Figs. 5 and 6. The standard deviation on the left is calculated from calibrated replicate CFA–CRDS measurements and shows the total variability between CFA–CRDS replications along the depth of the core. The standard deviation information in the right plot is calculated from calibration-adjusted datasets so that the effect of the calibration offset error is removed; this analysis is still dependent upon instrumental noise, CFA errors, depth registration errors, and natural variability within the core.

Our results reinforce the use of the CFA–CRDS method for high-precision, high-resolution measurements of $\Delta^{17}O$ in ice cores. CFA–CRDS methods are valuable for detecting detail in $\Delta^{17}O$ variations in deep ice layers, for measuring $\Delta^{17}O$ in ice from sites with low accumulation rates, or for measuring $\Delta^{17}O$ in any glacial ice where high depth resolution is desired.

5.2 Addressing CFA–CRDS calibration errors in $\Delta^{17}O$

Because the error of all $\Delta^{17}O$ measurements by CRDS depends on the calibration, the importance of establishing a robust calibration strategy for CFA–CRDS cannot be understated. We iteratively revised our CFA–CRDS system and designed our calibration strategy as recommended below.

First, the CFA–CRDS configuration must be capable of stable operations that span the total duration of the ice-core and reference water measurements. System stability for a given CFA system should be characterized with an Allan variance analysis. We have chosen to measure calibration standards immediately before and after ice-core measurements to improve the likelihood of measuring the calibration standard under the same system conditions as the ice-core sample. Additionally, limiting system memory and reducing the transition time between reference waters maximize the useful fraction of reference water data, allowing measurements of longer duration or measurements of more reference waters to be made within a period of consistent CFA operations.

Next, quantifying the drift in calibration information over time can allow an operator to determine the physical controls on fractionation within a CFA–CRDS system. The change in calibration information can be used to inform system maintenance schedules or operational sequences. For example, we have observed that after operating our CFA–CRDS system for several weeks, the fractionation responses for $\delta^{17}O$ and $\delta^{18}O$ diverge, degrading the quality of calibration data for $\Delta^{17}O$. Cleaning the vaporizer fittings appears to "reset" the calibration response, suggesting that the fractionation that occurs over long timescales is a result of physical effects within the vaporizer itself, likely owing to visible precipitate formation.

Though our system is capable of high-precision measurements for $\Delta^{17}O$, our analysis suggests that calibration bias persists in our data, which is unsurprising when considering previously published work on similar methods. The largest offsets (shown in Table 2) were associated with poor CFA stability due to a dirty vaporizer chamber. Large errors in $\Delta^{17}O$ were occasionally observed during the analysis of the South Pole ice core (SPC14); Steig et al. (2021) attributed these errors to calibration differences and performed a correction by shifting the mean value of their measurements based on the offset identified by a calibrated reference water measurement, similarly to Eq. (6). Our work supports the attribution of these errors to the calibration, and it also supports the calibration adjustment method. We recommend the use of additional reference water measurements to account for calibration offsets in $\Delta^{17}O$, and we also recommend that CFA systems are designed to ensure complete vaporization with flow conditions that are stable over long timescales. In our vaporizer, we observe that precipitate coatings can change the geometry of the vaporizer chamber and lead to incomplete vaporization over time, which degrades the quality of the calibration over time. When there is clear evidence of inconsistent vaporization (as in Fig. 3), we observe large calibration errors in $\Delta^{17}O$ by this method (tens to hundreds of per meg). Such issues likely also influence the vaporization process in other CFA systems, though they will not be readily detected in measurements of $\delta^{18}O$ or δD if the water vapor has homogenized before reaching the analyzer.

Finally, though it is perhaps impractical to measure replicate ice-core samples as we have done here, the average of our nine CFA–CRDS measurements shows that, like dual-inlet IRMS operations, stacking the CFA–CRDS data effectively averages over calibration inconsistencies. The results are comparable to highly resolved discrete CRDS or IRMS measurements. While CFA–CRDS measurements resolved to the centimeter scale still require long measurement times to achieve precise $\Delta^{17}O$ data (> 1000 s for 10 per meg precision), stacking CFA–CRDS measurements is an effective way to increase analysis time. Typically, achieving long measurement times while maintaining high depth resolution necessitates a reduction of melt rates. In practice, reduced melt rates may be incompatible with other measurement goals (such as trace gases) during an ice-core measurement campaign; reduced melt rates may also prevent the measurement of both ice-core samples and calibration standards within a period of stable system operations. We show that stacking multiple CFA–CRDS measurements provides a viable alternative strategy; stacking replicate CFA–CRDS measurements improves the accuracy of the measurement by averaging over the calibration offset noise, and it improves the measurement precision or measurement resolution by increasing the total analysis time for a given depth interval.

6 Summary

32

We measured $\Delta^{17}O$ in nine replicate ice-core samples using a continuous-flow analysis (CFA) system combined with a cavity-ring down laser spectrometer (CRDS). We measured a 10th replicate sample by discrete CRDS methods. We show that CFA–CRDS can reliably capture centimeter-scale variability of $\Delta^{17}O$ in ice-core samples; we identified seasonal fluctuations of ~ 45 per meg in $\Delta^{17}O$ from an ice core representing the preindustrial period in Greenland that agree with the discrete CRDS data and also with previously published measurements of seasonal $\Delta^{17}O$ variability in Greenland.

Our work shows that using CFA–CRDS methods can be valuable when high-precision and highly resolved measurements are desired. Our results show that mixing within the CFA system does not jeopardize CFA–CRDS measurements of $\Delta^{17}O$, even at centimeter-scale resolution. The mean of our stacked measurements exhibits neither a time lag nor any amplitude smoothing in comparison to the discretely prepared CRDS measurements. Rather, we show that the total error (~ 5 per meg for analysis times > 3000 s) is dominated by calibration bias. We note the importance of developing robust calibration strategies for $\Delta^{17}O$ when making measurements by CFA–CRDS, but we demonstrate that when calibration is accounted for, CFA–CRDS for $\Delta^{17}O$ is highly reproducible and can be tailored for high-resolution and high-precision measurements.

Data availability. Data generated for this study are available from the corresponding author upon reasonable request.

Author contributions. EJS, AJS, and LD conceived of the study. LD developed the measurement method, made the measurements, and completed the analysis with the support of AJS and EJS. All authors contributed to the paper.

Competing interests. The contact author has declared that none of the authors has any competing interests.

Disclaimer. Publisher's note: Copernicus Publications remains neutral with regard to jurisdictional claims in published maps and institutional affiliations.

Acknowledgements. This work was partially funded by the Hercules Dome Ice Core project and the Center for Oldest Ice Exploration. We are grateful to the two anonymous reviewers for their thoughtful improvements to this paper. Finally, making continuous measurements during the COVID-19 pandemic would not have been possible without the support of University of Washington undergraduate students Jacob Childers and Shana Edouard, who assisted with system maintenance and measurements.

Financial support. This research has been supported by the National Science Foundation (grant nos. 1841844 and 2019719).

Review statement. This paper was edited by Christof Janssen and reviewed by two anonymous referees.

References

Allan, D.: Statistics of atomic frequency standards, Proc. IEEE, 52, 221–230, https://doi.org/10.1109/PROC.1966.4634, 1966.

Angert, A., Cappa, C. D., and DePaolo, D. J.: Kinetic ^{17}O effects in the hydrologic cycle: Indirect evidence and implications, Geochim. Cosmochim. Ac., 68 , 3487–3495, https://doi.org/10.1016/j.gca.2004.02.010, 2004.

Aron, P. G., Levin, N. E., Beverly, E. J., Huth, T. E., Passey, B. H., Pelletier, E. M., Poulsen, C. J., Winkelstern, I. Z., and Yarian, D. A.: Triple oxygen isotopes in the water cycle, Chem. Geol., 565, 120026, https://doi.org/10.1016/j.chemgeo.2020.120026, 2021.

Barkan, E. and Luz, B.: High precision measurements of ^{17}O / ^{16}O and ^{18}O / ^{16}O ratios in H_2O, Rapid Commun. Mass Spectrom., 19, 3737–3742, https://doi.org/10.1002/rcm.2250, 2005.

Barkan, E. and Luz, B.: Diffusivity fractionations of H216O/H217O and $H_2^{16}O$ / $H_2^{18}O$ in air and their implications for isotope hydrology, Rapid Commun. Mass Spectrom., 21, 2999–3005, https://doi.org/10.1002/rcm.3180, 2007.

Berman, E. S. F., Levin, N. E., Landais, A., Li, S., and Owano, T: Measurement of δ^{18}O, δ^{17}O, and ^{17}O-excess in water by Off-Axis Integrated Cavity Output Spectroscopy and Isotope Ratio Mass Spectrometry, Anal. Chem., 85, 10392–10398, https://doi.org/10.1021/ac402366t, 2013.

Bigler, M., Svensson, A., Kettner, E., Vallelonga, P., Nielsen, M. E., and Steffensen, J. P.: Optimization of High-Resolution Continuous Flow Analysis for Transient Climate Signals in Ice Cores, Environ. Sci. Technol., 45, 4483–4489, https://doi.org/10.1021/es200118j, 2011.

Dansgaard, W.: Stable isotopes in precipitation, Tellus, 16, 436–468, https://doi.org/10.1111/j.2153-3490.1964.tb00181.x, 1964.

Dibb, J. E. and Fahnestock, M.: Snow accumulation, surface height change, and firn densification at Summit, Greenland: Insights from 2 years of in situ observation, J. Geophys. Res., 109, D24113, https://doi.org/10.1029/2003JD004300, 2004.

Emanuelsson, B. D., Baisden, W. T., Bertler, N. A. N., Keller, E. D., and Gkinis, V.: High-resolution continuous-flow analysis setup for water isotopic measurement from ice cores using laser spectroscopy, Atmos. Meas. Tech., 8, 2869–2883, https://doi.org/10.5194/amt-8-2869-2015, 2015.

Gkinis, V., Popp, T. J., Johnsen, S. J., and Blunier, T.: A continuous stream flash evaporator for the calibration of an IR cavity ring-down spectrometer for the isotopic analysis of water, Isotop. Environ. Health Stud., 46, 463–475, 2010.

Gkinis, V., Popp, T. J., Blunier, T., Bigler, M., Schüpbach, S., Kettner, E., and Johnsen, S. J.: Water isotopic ratios from a continuously melted ice core sample, Atmos. Meas. Tech., 4, 2531–2542, https://doi.org/10.5194/amt-4-2531-2011, 2011.

Gkinis, V., Simonsen, S. B., Buchardt, S. L., White, J. W. C., and Vinther, B. M.: Water isotope diffusion rates from the NorthGRIP ice core for the last 16 000 years-Glaciological and paleoclimatic implications, Earth Planet. Sc. Lett., 405, 132–141, 2014.

Hastings, M. G., Jarvis, J. C., and Steig, E. J.: Anthropogenic Impacts on Nitrogen Isotopes of Ice core Nitrate, Science, 324, 1288–1288, https://doi.org/10.1126/science.1170510, 2009.

Hawley, R. L., Morris, E. M., and McConnell, J. R.: Rapid techniques for determining annual accumulation applied at Summit, Greenland, J. Glaciol., 54, 839–845, https://doi.org/10.3189/002214308787779951, 2008.

Hawley, R. L., Neumann, T. A., Stevens, C. M., Brunt, K. M., and Sutterly, T. C.: Greenland Ice Sheet elevation change: Direct observation of process and attribution at summit, Geophys. Res. Lett., 47, e2020GL088864, https://doi.org/10.1029/2020GL088864, 2020.

Iannone, R. Q., Romanini, D., Cattani, O., Meijer, H. A. J., and Kerstel, E. R. T.: Water isotope ratio (d^2H and d^{18}O) measurements in atmospheric moisture using an optical feedback cavity enhanced absorption laser spectrometer, J. Geophys. Res., 115, D10111, https://doi.org/10.1029/2009JD012895, 2010.

Jones, T. R., White, J. W. C., Steig, E. J., Vaughn, B. H., Morris, V., Gkinis, V., Markle, B. R., and Schoenemann, S. W.: Improved methodologies for continuous-flow analysis of stable water isotopes in ice cores, Atmos. Meas. Tech., 10, 617–632, https://doi.org/10.5194/amt-10-617-2017, 2017a.

Jones, T. R., Cuffey, K. M., White, J. W. C., Steig, E. J., Buizert, C., Markle, B. R., McConnell, J. R., and Sigl, M.: Water isotope diffusion in the WAIS Divide ice core during the Holocene and last glacial, J. Geophys. Res.-Earth, 122, 290–309, https://doi.org/10.1002/2016JF003938, 2017b.

Jouzel, J. and Merlivat, L.: Deuterium and oxygen 18 in precipitation: Modeling of the isotopic effects during snow formation, J. Geophys. Res.-Atmos., 89, 11749–11757, https://doi.org/10.1029/JD089iD07p11749, 1984.

Jouzel, J., Froehlich, K., and Schotterer, U.: Deuterium and oxygen-18 in present-day precipitation: Data and modelling, Hydrolog. Sci. J., 42, 747–763, https://doi.org/10.1080/02626669709492070, 1997.

Kahle, E. C., Holme, C., Jones, T. R., Gkinis, V., and Steig, E. J.: A Generalized Approach to Estimating Diffusion Length of Stable Water Isotopes From Ice-Core Data, J. Geophys. Res.-Earth, 123, 2377–2391, https://doi.org/10.1029/2018JF004764, 2018.

Kahle, E. C., Steig, E. J., Jones, T. R., Fudge, T. J., Koutnik, M. R., Morris, V. A., Vaughn, B. H., Schauer, A. J., Stevens, C. M., Conway, H., Waddington, E. D., Buizert, C., Epifanio, J., and White, J. W. C.: Reconstruction of Temperature, Accumulation Rate, and Layer Thinning From an Ice Core at South Pole, Using a Statistical Inverse Method, J. Geophys. Res.-Atmos., 126, e2020JD033300, https://doi.org/10.1029/2020JD033300, 2021.

Kerstel, E. R. T., van Trigt, R., Dam, N., Reuss, J., and Meijer, H. A. J.: Simultaneous determination of the ^{2}H / ^{1}H, ^{17}O / ^{16}O and ^{18}O / ^{16}O isotope abundance ratios in water by means of laser spectrometry, Anal. Chem., 71, 5297–5303, 1999.

Landais, A., Barkan, E., and Luz, B.: Record of δ^{18}O and ^{17}O-excess in ice from Vostok Antarctica during the last 150 000 years, Geophys. Res. Lett., 35, L02709, https://doi.org/10.1029/2007GL032096, 2008.

Landais, A., Ekaykin, A., Barkan, E., Winkler, R., and Luz, B.: Seasonal Variations of ^{17} O-Excess and d-Excess in Snow Precipita-

tion at Vostok Station, East Antarctica, J. Glaciol., 58, 725–733, https://doi.org/10.3189/2012JoG11J237, 2012a.

Landais, A., Steen-Larsen, H. C., Guillevic, M., Masson-Delmotte, V., Vinther, B., and Winkler, R.: Triple isotopic composition of oxygen in surface snow and water vapor at NEEM (Greenland), Geochim. Cosmochim. Ac., 77, 304–316, https://doi.org/10.1016/j.gca.2011.11.022, 2012b.

Luz, B. and Barkan, E.: Variations of $^{17}O/^{16}O$ and $^{18}O/^{16}O$ in meteoric waters, Geochim. Cosmochim. Ac., 74, 6276–6286, https://doi.org/10.1016/j.gca.2010.08.016, 2010.

Meese, D. A., Gow, A. J., Grootes, P., Stuiver, M., Mayewski, P. A., Zielinski, G. A., Ram, M., Taylor, K. C., and Waddington, E. D.: The Accumulation Record from the GISP2 Core as an Indicator of Climate Change Throughout the Holocene, Science, 266, 1680–1682, https://doi.org/10.1126/science.266.5191.1680, 1994.

Merlivat, L. and Jouzel, J.: Global climatic interpretation of the deuterium-oxygen 18 relationship for precipitation, J. Geophys. Res., 84, 5029, https://doi.org/10.1029/JC084iC08p05029, 1979.

Schauer, A. J., Schoenemann, S. W., and Steig, E. J.: Routine High-Precision Analysis of Triple Water-Isotope Ratios Using Cavity Ring-down Spectroscopy, Rapid Commun. Mass Spectrom., 30, 2059–2069, 2016.

Schoenemann, S. W. and Steig, E. J.: Seasonal and spatial variations of $^{17}O_{excess}$ and d_{excess} in Antarctic precipitation: Insights from an intermediate complexity isotope model, J. Geophys. Res.-Atmos., 121, 11215–11247, https://doi.org/10.1002/2016JD025117, 2016.

Schoenemann, S. W., Schauer, A. J., and Steig, E. J.: Measurement of SLAP2 and GISP $\delta^{17}O$ and proposed VSMOW-SLAP normalization for $\delta^{17}O$ and ^{17}O excess, Rapid Commun. Mass Sp., 27, 582–590, https://doi.org/10.1002/rcm.6486, 2013.

Schoenemann, S. W., Steig, E. J., Ding, Q., Markle, B. R., and Schauer, A. J.: Triple water-isotopologue record from WAIS Divide, Antarctica: Controls on glacial-interglacial changes in $^{17}O_{excess}$ of precipitation: WAIS LGM-Holocene ^{17}O excess Record, J. Geophys. Res.-Atmos., 119, 8741–8763, https://doi.org/10.1002/2014JD021770, 2014.

Steen-Larsen, H. C., Masson-Delmotte, V., Sjolte, J., Johnsen, S. J., Vinther, B. M., Bréon, F.-M., Clausen, H. B., Dahl-Jensen, D., Falourd, S., Fettweis, X., Gallée, H., Jouzel, J., Kageyama, M., Lerche, H., Minster, B., Picard, G., Punge, H. J., Risi, C., Salas, D., Schwander, J., Steffen, K., Sveinbjörnsdóttir, A. E., Svensson, A., and White, J.: Understanding the Climatic Signal in the Water Stable Isotope Records from the NEEM Shallow Firn/Ice Cores in Northwest Greenland., J. Geophys. Res., 116, D06108, https://doi.org/10.1029/2010JD014311, 2011.

Steen-Larsen, H. C., Masson-Delmotte, V., Hirabayashi, M., Winkler, R., Satow, K., Prié, F., Bayou, N., Brun, E., Cuffey, K. M., Dahl-Jensen, D., Dumont, M., Guillevic, M., Kipfstuhl, S., Landais, A., Popp, T., Risi, C., Steffen, K., Stenni, B., and Sveinbjörnsdottír, A. E.: What controls the isotopic composition of Greenland surface snow?, Clim. Past, 10, 377–392, https://doi.org/10.5194/cp-10-377-2014, 2014.

Steig, E. J., Gkinis, V., Schauer, A. J., Schoenemann, S. W., Samek, K., Hoffnagle, J., Dennis, K. J., and Tan, S. M.: Calibrated high-precision ^{17}O-excess measurements using cavity ring-down spectroscopy with laser-current-tuned cavity resonance, Atmos. Meas. Tech., 7, 2421–2435, https://doi.org/10.5194/amt-7-2421-2014, 2014.

Steig, E. J., Jones, T. R., Schauer, A. J., Kahle, E. C., Morris, V. A., Vaughn, B. H., Davidge, L., and White, J. W. C.: Continuous-Flow Analysis of $\delta^{17}O$, $\delta^{18}O$, and δD of H_2O on an Ice Core from the South Pole, Front. Earth Sci., 9, 640292, https://doi.org/10.3389/feart.2021.640292, 2021.

Tian, C., Wang, L., and Novick, K. A.: Water vapor δ^2H, $\delta^{18}O$ and $\delta^{17}O$ measurements using an off-axis integrated cavity output spectrometer – sensitivity to water vapor concentration, delta value and averaging-time, Rapid Commun. Mass Spectrom., 30, 2077–2086, https://doi.org/10.1002/rcm.7714, 2016.

Uemura, R., Barkan, E., Abe, O., and Luz, B.: Triple isotope composition of oxygen in atmospheric water vapor: the ^{17}O-excess of water vapor, Geophys. Res. Lett., 37, L04402, https://doi.org/10.1029/2009GL041960, 2010.

Werle, P., Miicke, R., and Slemr, F.: The limits of signal averaging in atmospheric trace-gas monitoring by tunable diode-laser absorption spectroscopy (TDLAS), Appl. Phys. B-Photo., 57, 131–139, https://doi.org/10.1007/BF00425997, 1993.

2.3 Advances in triple oxygen isotope analysis and applications for ice-core paleoclimate science

A brief publication resulting from the work presented in Section 2.2 is reprinted from *Past Global Changes*, below.

doi.org/10.22498/pages.31.2.102

Advances in triple oxygen isotope analysis and applications for ice-core paleoclimate science [36]

Lindsey Davidge

Stable water-isotope measurements from ice cores reflect paleo-atmospheric thermodynamics along upstream moisture pathways. New analytical methods simplify the measurement of triple oxygen isotopes, which will improve measurement resolution and provide more complete information about the past atmosphere.

Water isotopes in ice cores ($\delta^{17}O$, $\delta^{18}O$, δD, deuterium excess, and ^{17}O excess) reflect past climate conditions

Stable water-isotope measurements (e.g. $\delta^{18}O$ and δD) from ice cores reflect temperature and other thermodynamic conditions of the past atmosphere. As atmospheric moisture moves poleward from evaporative source regions to eventual precipitation sites, mass-dependent fractionation processes progressively distill its isotopic composition. First-order, temperature-dependent equilibrium fractionation during precipitation is the dominant control on the observed ratio of heavy-to-light isotope abundance (i.e. $\delta^{17}O$, $\delta^{18}O$, or δD) at the ice-core site, and the water-isotope paleothermometer has consequently been a cornerstone of ice-core paleoclimate science for decades (e.g. Dansgaard 1964).

However, even these conventional applications of the water-isotope temperature proxy rely on quantitative models of upstream fractionation pathways. In other words, even though the condensation temperature exhibits large control on the water-isotope signal of the precipitation, the isotopic composition of the air parcel that condenses is predetermined by all upstream thermodynamic processes (e.g. Merlivat and Jouzel 1979). Modeling many unknown upstream fractionation processes (e.g. evaporation, atmospheric transport, and precipitation) is improved by the inclusion of additional water isotope observations that reflect those processes.

Second-order water-isotope quantities like deuterium excess (d) or ^{17}O excess ($\Delta^{17}O$) – which are defined by the relationships between δD and $\delta^{18}O$ (d) or $\delta^{17}O$ and $\delta^{18}O$ ($\Delta^{17}O$) as indicated in Figure 1a–b –, are dominated by these upstream kinetic fractionation events, and they can therefore provide information about the integrated history of an air parcel that has reached an ice-core site. While d and $\Delta^{17}O$ both depend on temperature and humidity variations in the atmosphere, the sensitivities of d and $\Delta^{17}O$ during fractionation are different, e.g. the relative effect of evaporation temperature is more important for d, and the relative effect of evaporation humidity is more important for $\Delta^{17}O$ (e.g. Uemura 2010). Therefore, measuring d and $\Delta^{17}O$ together should provide the most complete information about the past hydrosphere. The differences between d and $\Delta^{17}O$ are highlighted in Figures 1c–f, which show seasonally resolved measurements of d and $\Delta^{17}O$ from three ice-core sections from Greenland.

Despite the theoretical potential for $\Delta^{17}O$ to be a complementary tracer to d, traditional ice-core work has not included $\delta^{17}O$ or $\Delta^{17}O$ due to measurement limitations. Most commonly, $\delta^{18}O$ and d have been used to reconstruct past condensation-site and evaporation-source temperatures, but this method is imperfect because, in addition to the evaporation temperature, d is also influenced by other thermodynamic conditions during evaporation, atmospheric transport, and precipitation (Merlivat and Jouzel 1979). Including corresponding measurements of $\Delta^{17}O$ would provide an additional constraint for reconstructing the water-isotope fractionation pathways, and it is therefore desirable to produce records of $\Delta^{17}O$ and to develop climate models that account for $\Delta^{17}O$ (e.g. Markle and Steig 2022; Schoenemann and Steig 2016). The following sections describe recent improvements to $\Delta^{17}O$ measurement methodology and present existing ice-core records of $\Delta^{17}O$.

Recent advances in instrumentation improve temporal resolution of $\Delta^{17}O$ from ice cores

Although d has routinely been measured on ice cores for decades, measuring $\Delta^{17}O$ has only been possible for about 20 years (e.g. Barkan and Luz 2005), and observations of $\Delta^{17}O$ are limited in spatial and temporal resolution. However, new analytical methods have the potential to simplify the measurement of $\Delta^{17}O$ – which, when measured at all, is typically determined separately from other water-isotope quantities by discrete isotope-ratio mass spectrometry (e.g. Barkan and Luz 2005). Unlike d or $\delta^{18}O$, which vary in meteoric water by several or tens of "per mil" (‰, or parts per thousand), respectively, the natural variability of $\Delta^{17}O$ in precipitation is

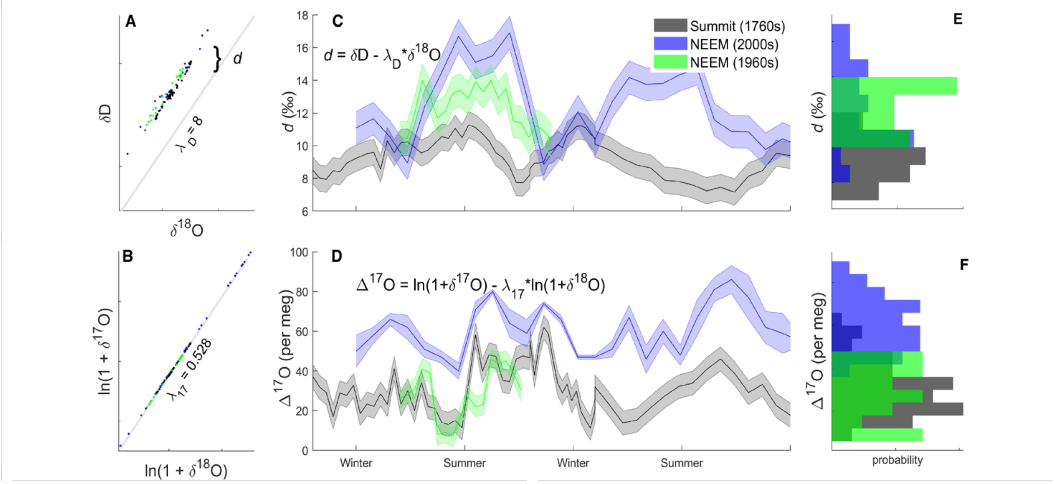

Figure 1: The relationships between δD or $\delta^{17}O$ and $\delta^{18}O$ – which define d and $\Delta^{17}O$ – are provided in **(A)** and **(B)**, respectively. Formal definitions of d and $\Delta^{17}O$ are given by the equations in **(C)** and **(D)**. (C) and (D) provide seasonally resolved records of d and $\Delta^{17}O$ from NEEM (Landais et al. 2012a) and Summit (Davidge et al. 2022), both ice-core sites in Greenland. The decade of the measured ice-core layers is provided in the legend – see the original publications for dating methodologies. All data were aligned to the seasonal cycle of corresponding $\delta^{18}O$ measurements to highlight seasonal patterns in d and $\Delta^{17}O$. Corresponding histograms of these same data are binned by the typical analytical uncertainty and highlight the differences in d **(E)** and $\Delta^{17}O$ **(F)** distribution observed at these sites.

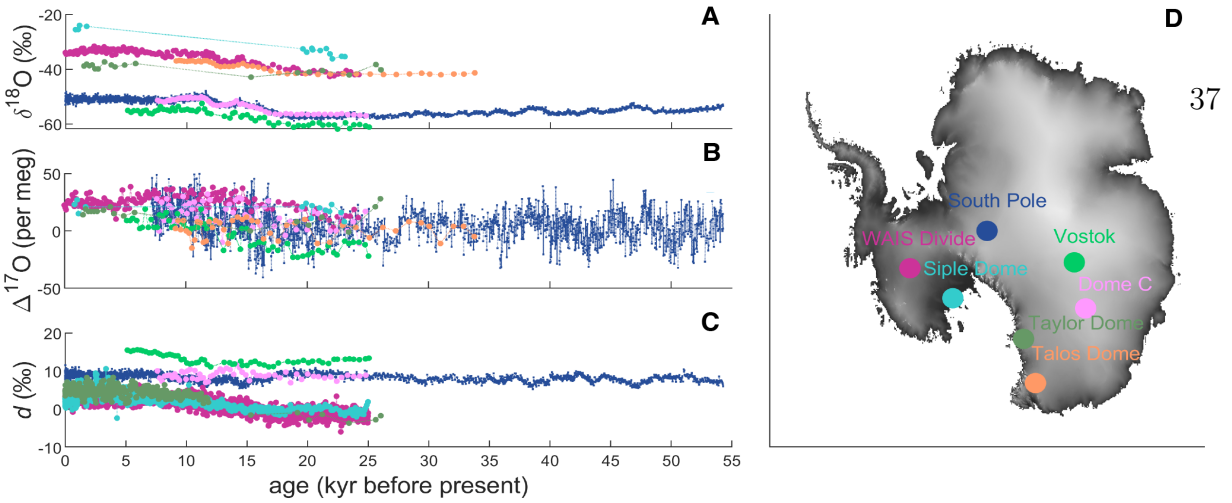

Figure 2: Corresponding measurements of $\delta^{18}O$ **(A)** , $\Delta^{17}O$ **(B)**, and *d* **(C)** for available Antarctic ice-core sites, whose locations are mapped in **(D)**. Continuously measured data from the South Pole is averaged to show 50 cm resolution for all isotope values (from Steig et al. 2021). All discrete data are shown at their measured resolutions. Details about data normalization protocols for $\Delta^{17}O$, and source information for all discretely measured data, are available from Schoenemann et al. (2013) and Schoenemann et al. (2014), respectively.

only tens of "per meg" (or parts per million), which exacerbates measurement difficulties. However, recent advances in cavity ring-down laser spectroscopy (CRDS) enable the simultaneous measurement of all stable water isotopes (i.e. $\delta^{17}O$, $\delta^{18}O$, δD, $\Delta^{17}O$, and *d*) with precision that meets or exceeds that of traditional methods (see Steig et al. 2014). CRDS is an appealing method not only because it can measure all water isotopes at once, but also because it can be combined with continuous sample melting strategies that are already in use for other ice-core analyses. Over the last 10 years, continuous-flow analysis (CFA) has been widely adopted by ice-core laboratories, and measurements of $\delta^{18}O$, δD, and *d* by CFA-CRDS are already routine for ice-core measurement campaigns (e.g. Emanuelsson et al. 2015). Recent work (Davidge et al. 2022; Steig et al. 2021) demonstrates that CFA-CRDS for all stable water isotopes can greatly reduce the analysis time for $\Delta^{17}O$ and it can therefore improve the time resolution of $\Delta^{17}O$ measurements. CFA-CRDS methods will be useful for improving the temporal and spatial resolution of $\Delta^{17}O$ to characterize the natural variability of meteoric $\Delta^{17}O$.

Recent work demonstrates that CFA-CRDS for $\Delta^{17}O$ can indeed improve the resolution of $\Delta^{17}O$ observations with high precision (<10 per meg), especially when CFA for $\Delta^{17}O$ is developed with specific attention to calibration strategies (Davidge et al. 2022; Steig et al. 2021). Steig et al. (2021) measured the lower 1200 m of the South Pole ice core by CFA-CRDS for all stable water isotopes, revealing significant millennial-scale variability in $\Delta^{17}O$ that is not observed in coarser records of $\Delta^{17}O$ from other ice-core sites, but that is coincident with other climatic events recorded by *d* and $\delta^{18}O$ (Figs. 2a–c). However, they also identify the importance of frequent (i.e. daily) data calibration against multiple reference waters, adopting a new calibration method that utilizes more reference water measurements than typical CRDS strategies. Davidge et al. (2022) demonstrated that CFA-CRDS for $\Delta^{17}O$ performs as well as discrete methods by measuring replicate sections of an ice core from Greenland; annually resolved data from that study are provided in Figure 1c–d. They also found that, though small, the greatest source of uncertainty for $\Delta^{17}O$ by CFA-CRDS is the calibration technique. Both studies suggest that the measurement resolution depends on the desired precision for $\Delta^{17}O$ and the rate of the continuous melter. Continuing to develop and implement CFA-CRDS methods so that more existing ice cores can be measured for $\Delta^{17}O$ will improve the spatial and temporal resolution of $\Delta^{17}O$, which is a critical step for studying atmospheric controls on second-order water-isotope quantities and refining interpretations of the paleoclimate record.

$\Delta^{17}O$ data varies on seasonal, millennial, and glacial timescales

Utilizing CFA-CRDS to characterize the full range of variability in both *d* and $\Delta^{17}O$ – and the differences between them – should allow the decoupling of equilibrium and kinetic fractionation during evaporation, which will improve reconstructions made from water-isotope measurements. Because the signal-to-noise ratios for both *d* and $\Delta^{17}O$ are generally quite small, quantifying the relationship between them will be most straightforward on timescales and at locations where variability is greatest. Existing ice-core records of $\Delta^{17}O$ from both Greenland and Antarctica are provided in Figures 1 and 2. Figure 1c–d shows the seasonality of $\Delta^{17}O$ and *d* in Greenland glacial ice and indicates a seasonal magnitude of 40–50 per meg for $\Delta^{17}O$. Similar seasonal magnitudes have been observed over Antarctica (e.g. Landais et al. 2012b; Schoenemann and Steig 2016). Figure 2 presents deep ice-core records of $\Delta^{17}O$, *d*, and $\delta^{18}O$ from Antarctica, where the observed increase in $\Delta^{17}O$ between the last glacial period and the Holocene range from four to five per meg at some coastal sites (e.g. Taylor Dome or Siple Dome) to more than 20 per meg at inland locations like Vostok. The amplitude of millennial-scale variations observed in the CFA-CRDS record from the South Pole is more than 30 per meg (Steig et al. 2021). Efforts to pinpoint the specific controls on *d* and $\Delta^{17}O$ by comparing measurements with climate reanalysis products (e.g. Landais et al. 2012a) or isotope-enabled climate simulations (e.g. Dütsch et al. 2019; Schoenemann et al. 2014) will be facilitated by corresponding, high-resolution measurements of all first- and second-order water-isotope quantities, and CFA-CRDS techniques provide a method for developing those data.

ACKNOWLEDGEMENTS

Special thanks to Spruce Schoenemann, Andrew Schauer, and Eric Steig for their thoughtful improvements to this article.

AFFILIATION

Department of Earth and Space Sciences, University of Washington, USA

CONTACT

Lindsey Davidge: ldavidge@uw.edu

REFERENCES

Barkan E, Luz B(2005) Rapid Commun Mass Spectrom 19: 3737-3742

Dansgaard W (1964) Tellus 16: 436-468

Davidge L et al. (2022) Atmos Meas Tech 15: 7337-7351

Dütsch M et al. (2019) Quantifying different climatic controls on *d*-excess and ^{17}O-excess in Antarctic ice cores with the isotope-enabled Community Atmosphere Model (iCAM). 2019 AGU Fall Meeting, San Francisco, USA

Emanuelsson BD et al. (2015) Atmos Meas Tech 8: 2869-2883

Landais A et al. (2012a) Geochim Cosmochim Acta 77: 304-316

Landais A et al. (2012b) J Glaciol 58: 725-733

Markle BR, Steig EJ (2022) Clim Past 18: 1321-1368

Merlivat L, Jouzel J (1979) J Geophys Res 84: 5029-5033

Schoenemann SW, Steig EJ (2016) J Geophys Res: Atmos 121: 11215-11247

Schoenemann SW et al. (2013) Rapid Commun Mass Spectrom 27: 582

Schoenemann SW et al. (2014) J Geophys Res Atmos 119: 8741-8763

Steig EJ et al. (2014) Atmos Meas Tech 7: 2421

Steig EJ et al. (2021) Frontiers in Earth Sci 9: 640292

Uemura R (2010) Geophys Res Let 37: L04402-L04406

2.4 Implementation of CFA for water isotopes for COLDEX

Research from this chapter was critical in the development of the integrated continuous-flow analysis (CFA) system that has been operational in the COLDEX collaborative laboratory space at Oregon State University since 2024. In the COLDEX laboratory, a Picarro L2140-i laser spectrometer measures water isotopes from a sample processing line which is similar to the system described in Section 2.2. Additional streams of water from the continuous melter are partitioned into other instrument lines that measure CH_4, CO, and dust; a final meltwater stream is sampled by a discrete fraction collector for asynchronous, discrete water chemistry analysis (see Hudak et al., 2024, for additional details on the combined CFA instrumentation).

Integrating multiple CFA lines enables the simultaneous measurement of water isotopes alongside atmospheric gases and other ice-core proxies. However, because operational demands differ between analyses, some key differences exist between the water-isotope CFA instrumentation described in Section 2.2 and the CFA instrumentation installed in the COLDEX lab. Critically, the COLDEX CFA melt system must operate at a rate that is high enough to prevent gas loss at the melt head, which is important for obtaining accurate measurements of CH_4 and CO. COLDEX CFA operations in 2024 used a melt rate of about 3.7cm/min, which is similar to other integrated CFA systems (e.g. Chappellaz et al., 2013) but notably faster than the 0.3cm/min rate used in Section 2.2. The effect of this change is reduced residence time within the spectrometer and a lower-resolution water-isotope record – especially for $\Delta^{17}O$, which requires a long data integration time (>17 minutes) to produce a sufficient signal-to-noise ratio. With minor changes related to these operating conditions, a duplicate CFA system in the COLDEX lab measured 68 m of Allan Hills core ALHIC2201 in 2024, and it will continue to be used to measure COLDEX cores in coming years. A plot highlighting the improved detail of the CFA record relative to the sub-meter-resolved drilling chips data for ALHIC2201 is shown in Figure 2.1.

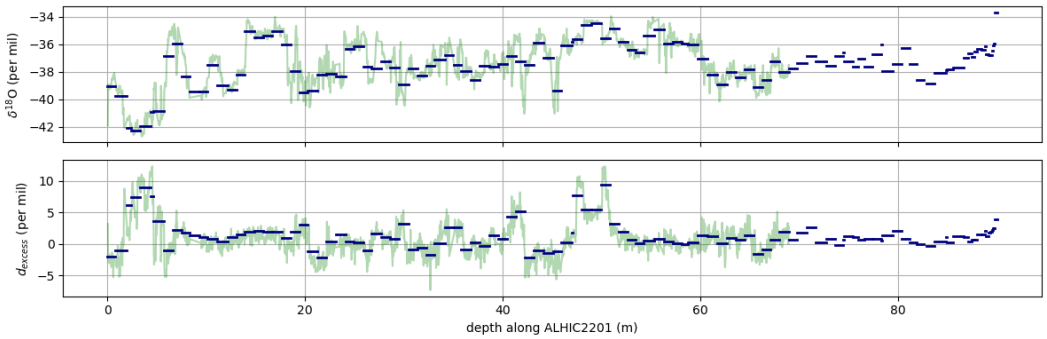

Figure 2.1: δ^{18}O and d_{excess} of drilling chips recovered from ALHIC2201 (blue) and the CFA record from ALHIC2201 (green; Hudak et al., in prep.) All CFA data are shown at 1-cm resolution.

Chapter 3

REPRODUCIBILITY OF WATER-ISOTOPE SIGNALS AT KILOMETER AND CENTIMETER SCALES IN THE ALLAN HILLS

3.1 Overview

Ice as old as 6 Ma has been recovered from the Allan Hills BIA, thus extending the ice-core record by several million years. However, existing records from the Allan Hills rely on absolute dating of stratigraphically disturbed layers; neither the scale of stratigraphic disturbance nor the amount of time represented by any individual sample is known, which complicates both the selection of new core sites and the interpretation of data produced from disturbed ice. Here, I investigate the scale of stratigraphic disturbance both between core sites and within a single core by examining the reproducibility of stable water-isotope records. Recent work has demonstrated that over long timescales, the water-isotope record in the Allan Hills is correlated with age, likely owing to the cooling trend in Earth's climate over the last several million years (Shackleton et al., submitted); I leverage this direct relationship between water isotopes and age to investigate large-scale stratigraphic disturbances in the Allan Hills with new and published water-isotope data from seven core sites. I evaluate the repeatability of water-isotope values at all sites, and I cross-correlate four water-isotope records from cores along a flow-line transect up to distances of 140 m. Significant correlations among these isotope records ($0.27 < r < 0.80$) demonstrate that meter-scale averages contain isotopically similar packets of ice along this transect, but with notably dipping layers and asymmetrical thinning. Furthermore, evidence of layer thickness changes between core sites indicates nonlinear thinning along the modern flow line, including additional material at the top of the ALHIC1503 column and approximately 20 m of ablated materials missing from the top of the ALHIC2201 column.

In addition, I present new 1-cm vertically resolved data for a 24-cm-diameter ice core with disturbed stratigraphy; these measurements indicate the first evidence of isotopic patterning akin to glacial-interglacial fluctuations in disturbed blue ice. A replicate dataset from the same sections, but laterally separated by 17-24 cm, demonstrates that this high-frequency patterning is reproducible across the core ($0.46 < r < 0.99$). We find evidence of steeply dipping internal layers (up to 43°) and asymmetrical layer thicknesses. Layer dip and

asymmetry is similar at both centimeter and 100-meter scales, and could reflect the bedrock topography and thinning along the flowline.

Parts of this chapter were completed collaboratively with former undergraduate researcher Haley Lowes-Bicay, whom I mentored through the COLDEX REU program and as an independent study student from 2022-2024.

3.2 Introduction

Paleoclimate records from marine sediments show that there was a transition in the characteristic timescale of climate variations from 40,000 year to 100,000 year periods during the mid-Pleistocene (approximately 1250-700 ka), although the cause of this transition ("the MPT") is unclear (Roe and Allen, 1999; Clark et al., 2006). Possible explanations rely upon ice-sheet growth feedbacks or instabilities (e.g., Gregoire et al., 2012; Bintanja and van der Wiel, 2008; Marshall and Clark, 2002), erosion of subglacial regolith (Clark and Pollard, 1998), changes in sea-ice extent (Gildor and Tziperman, 2000; 2001), or changes in ocean circulation and greenhouse gases (Willeit et al., 2019; Köhler and Bintanja, 2008). Ice cores that extend beyond 1 Ma could provide additional evidence needed to evaluate the cause or causes of the MPT because they contain a direct archive of past atmospheric gases and meteoric water, and can therefore be used to generate corresponding histories of temperature, greenhouse gases, and other observations that could elucidate causes of this climatic shift.

In the Allan Hills blue ice area (BIA) of Antarctica, exhumation of very old ice is caused by ablation and net vertical advection (Sinisalo and Moore, 2010; Spaulding et al., 2013; Higgins et al., 2015; Shackleton et al., submitted; Yan et al., 2021). Several cores have been retrieved from the Allan Hills in the last decade, including cores with ice that is 4-6 Ma at the bed (Shackleton et al., submitted). Shackleton et al. (submitted; 2024) and Marks Peterson et al. (2024)) produced composite ice-core records from multiple Allan Hills sites; those data imply regional cooling over the last 6 Ma that is commensurate with expectations from benthic records (i.e., Westerhold et al., 2020), and mean CH_4 and CO_2 values as old as 3 Ma.

However, ice stratigraphy in this region is complicated by the deformation history of blue ice: the region is characterized by very low regional accumulation rates (<1 cm/year; Dadic et al., 2015), extreme thinning (10ka-1Ma/m; Shackleton et al., submitted), and complex ice flow (e.g. Spaulding et al., 2012; Kerhl et al., 2018), yielding ice that is stratigraphically disordered and mixed at scales that are not known. Shackleton et al. (submitted) identified several reversals in the age-depth relationship at site ALHIC1901 (see Figure 3.1), indicative of recumbent folding over scales of several meters. Radar stratigraphy from the Allan Hills identifies local large-scale nonconformities at some sites and internal layers that dip as much as 45°, roughly following the steep topography of the underlying bedrock (e.g. Kerhl et al, 2018, Yan et al., 2019). However, internal layers identified by ice-penetrating radar – which are often interpreted as continuous time horizons due to the similarity of electrochemical properties of same-age snow at deposition – could also be caused by glaciological mixing or the entrainment of debris over time, so additional information is needed to understand the spatial continuity of ice layers and the amount of time represented by an individual sample.

Dating stratigraphically disordered ice cores relies upon the absolute dating of atmospheric ^{40}Ar that is contained within bubbles in the core (Bender et al., 2008; Higgins et al., 2015); this method provides an average age for each 0.2-0.6 kg sample of ice. While absolute dating has identified similar ages of ice at the bed at geographically proximal sites (such as from ALHIC1503 and ALHIC1901 in Yan et al., 2019 and Shackleton et al., submitted, respectively – see Figure 3.1), it is not clear whether isochrons (i.e., same-age layers) are spatially continuous between, or even within, different ice cores. This uncertainty complicates the interpretation of measurements made from different samples of ice. However, studying the internal deformation of blue ice by dating alone is not practical.

Shackleton et al. (submitted) showed that over million-year timescales, ^{40}Ar and δ^{18}O from Allan Hills ice are correlated, such that water-isotope measurements could be used as a general indicator of age over long timescales. Water isotopes (e.g., δ^{18}O, δD) from ice-cores are commonly measured due to their first-order relationship with local temperature during deposition and subsequent utility as a paleothermometer (e.g., Craig, 1961; Dansgaard,

1964). Likely due to long-term cooling since the Miocene, a gradual reduction of more than 10 in δ^{18}O is observed in Allan Hills ice since 6 Ma (Shackleton et al., submitted; 2024), which suggests that δ^{18}O could be used as an indicator of temporal similarity between sites over million-year timescales. By extension, water isotopes could be a useful indicator of layer continuity and mixing, even when layer ages are not known.

Due to their relationship with temperature, δ^{18}O and δD also fluctuate on glacial-interglacial timescales. If glacial-interglacial information is preserved in Allan Hills cores, the reproducibility of those signals could also provide insight into the scale of stratigraphic disturbance over appropriate depth scales. Spaulding et al. (2013) found glacial and interglacial water-isotope values at Site 27 (S27) between 90 and 250 ka, and most of the expected glacial-interglacial water-isotope variability was reproduced at ALHIC1503 for 1-Ma ice (Higgins et al., 2015); this suggests that glacial-interglacial values could also be preserved at other Allan Hills sites. The best-dated Allan Hills ice core is currently ALHIC1901, a 24-cm-diameter core that was drilled near ALHIC1503 (see Figure 3.1). The layer thicknesses implied by the age scale of Shackleton et al. (submitted) for ALHIC1901 suggest that glacial cycles in ALHIC1901 are likely centimeters to tens of centimeters in depth, and therefore potentially recoverable through higher-resolution sampling.

Here, we evaluate the reproducibility of water-isotope information between core sites and within a single ice core to make inferences about the scale of stratigraphic disturbance in this ice. We present new <1-m vertically resolved water-isotope data for three cores drilled during the 2022-2023 and 2023-2024 austral summers. We evaluate the distribution of water-isotope data at seven ice-core sites, and we cross-correlate the water-isotope signal between the four closest cores to evaluate stratigraphic continuity between core sites. We also present new, 1-cm vertically resolved, same-depth replicate water-isotope measurements spanning approximately 7 m of ALHIC1901. We identify patterned fluctuations within these samples and cross-correlate the water isotope signal between the replicate measurements to evaluate the disturbances across lateral distances of 17-24 cm. At both scales, we find evidence of differential thinning and evidence of steeply dipping internal layers that generally follow the

bedrock topography. Our results show that the isotopic similarity between cores generally decreases with distance. We discuss implications for ice core handling and implications for blue-ice flow conditions in the Allan Hills.

3.3 Measurement protocols and data comparison techniques

We prepared and measured two types of ice-core samples for this study that correspond to the two spatial scales of focus: drilling chips from three new cores that are resolved to <1 m, and replicate samples from disturbed layers of ALHIC1901 that are vertically resolved to 1 cm. Homogenized drilling chips are representative of the average isotope values for each returned barrel (e.g. Rowell et al., 2023), and therefore represent an average of all penetrated depths, even when ice is not recovered. This study presents new data from drilling chips collected during the 22-23 and 23-24 austral summers, including from the following cores: ALHIC1902 (135-162 m), ALHIC2201 (0-90 m/bedrock), ALHIC2301 (2-89 m (likely near bed)) and ALHIC2302 (0-143 m, first drilling season only). We compare the isotopic composition from these new records with published data from site ALHIC1502 (Yan et al., 2019), ALHIC1503 (Higgins et al., 2015; Yan et al., 2019), and ALHIC1901 and ALHIC1902 (Shackleton et al., submitted), all of which are shown in Figure 3.1.

To consider the signal reproducibility within a single core, we measured replicate samples from ALHIC1901 between depths of 135 and 156 m. ALHIC1901 is a 24-cm diameter, discontinuous blue ice core (core recovery 90%) that was drilled to bedrock (160 m). Ice fracture during drilling resulted in short (14±10 cm for the measured interval) sections with nonuniform shapes and variable ice quality; many pieces contain internal fractures and others cleaved along oblique planes during drilling or in transport. Absolute ages were determined by ^{40}Ar dating by Shackleton et al. (submitted) with a median sample resolution of 28.5 cm (ranging from 14 to 63 cm). We measured ice from an interval with estimated ages of 550-850 ka; we refer to this 135-142 m ice as "<900 ka ice". We also measured one section of ice approximately 5 m above the bed near ice of 1.3 Ma, which we refer to as ">1 Ma ice". For the <900 ka ice, we measured two replicate sample sets separated by a

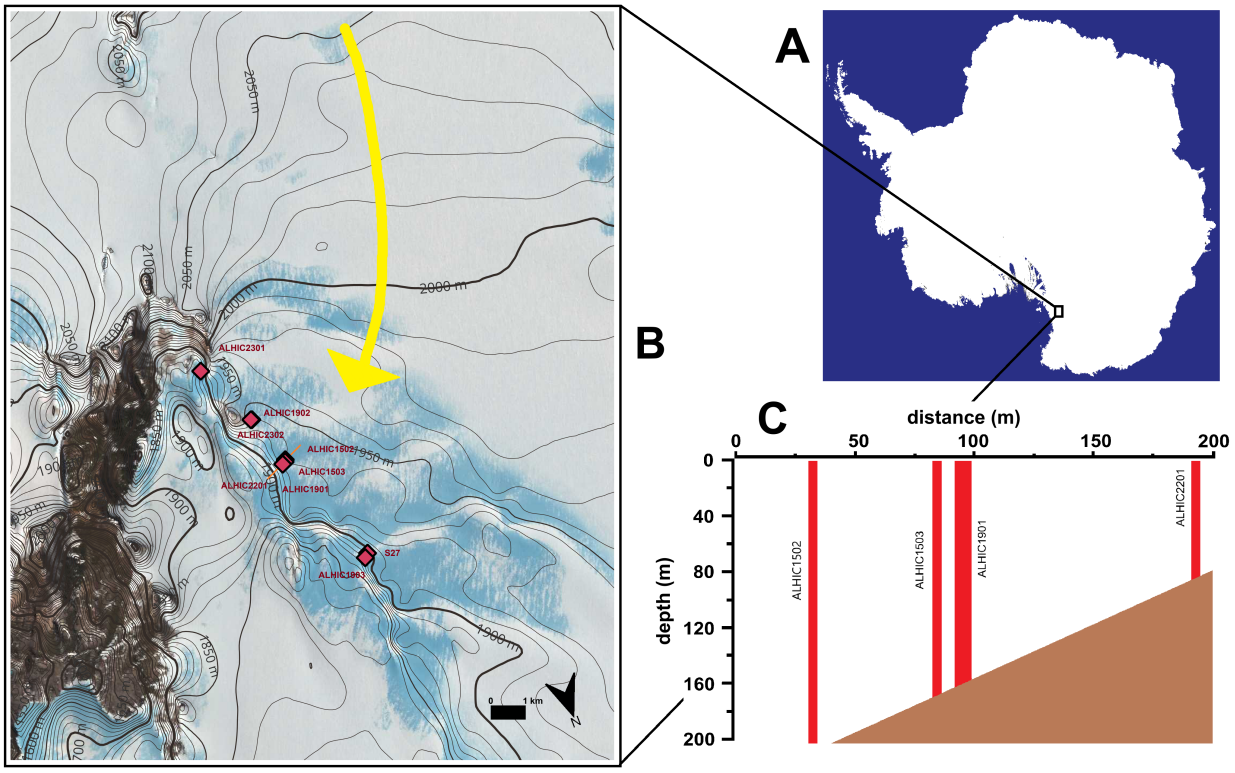

Figure 3.1: A) Map of Antarctica showing REMA coastlines and indicating the location of the Allan Hills. B) Regional map of the Allan Hills, including all cores used in this study (pink diamonds), approximate direction of modern ice flow (yellow arrow), and transect location along cores ALHIC1502, ALHIC1503, ALHIC1901, and ALHIC2201 (orange line). Satellite imagery is from LIMA and elevation contours are from REMA. C) Simplified schematic of cross-sectional view following the transect in the direction of modern ice flow. Note that the large-diameter (24-cm) core ALHIC1901 is indicated as a wider borehole, but that all core dimensions are exaggerated. Bedrock depth is an estimate from Yan et al. (2019) and is not in agreement with all core depths; see table 1.1 for more accurate depth details for each core.

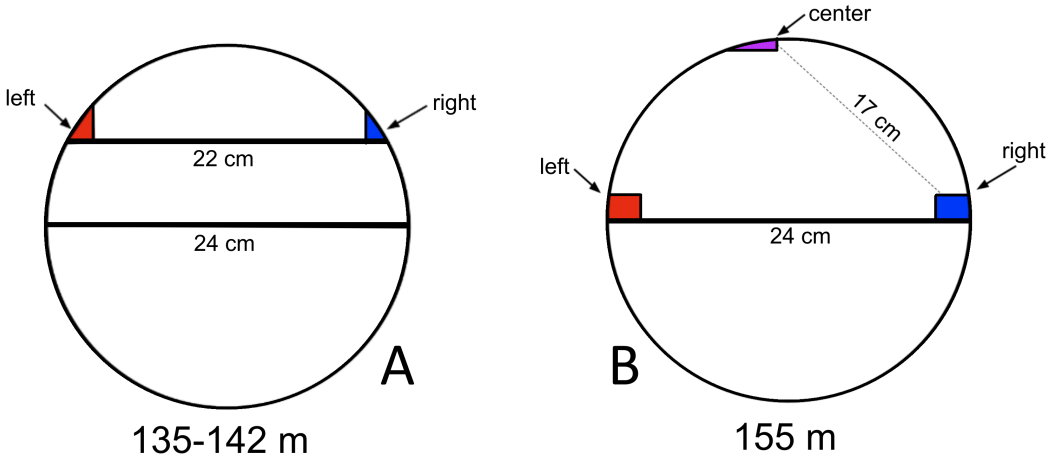

Figure 3.2: Water isotope cut plan for measured depths of ALHIC1901. Blue denotes the reference measurement and red and purple indicate replicate measurement positions. **A)** Water isotope cut plan for 135.51 m - 141.51 m (<900ka ice). **B)** Water isotope cut plan for 155.07 - 155.34 m interval (>1Ma ice).

horizontal distance of 22 cm; for the >1Ma ice, we measured three replicate sample sets that are horizontally separated by approximately 24 cm and 17 cm. The cut plan is shown in Figure 3.2. Sample preparation, measurement protocols, and data analysis techniques for all samples are described below.

3.3.1 Sample preparation and measurement by laser spectroscopy

Both drilling chips and ALHIC1901 core samples were subsampled and measured at the University of Washington. Chips were recovered from each drill run and were homogenized in the field by manual mixing within a large stainless steel bowl. Approximately 150-250 grams of drilling chips were subsampled into polyethylene Whirl-Pak bags and shipped frozen to the University of Washington. In the lab, the samples were homogenized again in a -17℃ freezer with a mortar and pestle. Approximately 10 cubic centimeters of re-homogenized chips were subsampled into polyethylene bottles, and then transferred into a 4℃ refrigerator to thaw. ALHIC1901 core samples were cut by bandsaw within a -17℃ freezer in accordance with

Figure 3.2. The samples were melted in 10-ml polyethylene bottles in a 4℃ refrigerator. For all samples, 150 μL of sample meltwater were loaded into a glass vial with a conical insert for autosampler analysis by Picarro L2130-i or Picarro L2140-i following Schauer et al. (2016). Samples were measured in High Precision mode with 6-12 injections per sample and were calibrated to three internal reference waters that have been calibrated against the VSMOW-SLAP scale. The average root mean square errors associated with the calibrated data used in this study are 0.14, 0.67, and 1.0% for δ^{18}O, δD, and d_{excess}, respectively.

Vertical depths were assigned for all samples according to the field-logged sample depths. Because drilling conditions varied in the field, the depth intervals represented by each chip sample vary (see Table 1.2 for specific core details). The 1-cm resolved vertical depths for ALHIC1901 were interpolated from field-logged depths. However, because many sections of ALHIC1901 are characterized by angular fractures, the section lengths around the perimeter of the core are not uniform; consequently, in our study, the length of each reference sample does not necessarily correspond to the length of its replicate(s). Depth uncertainties associated with these discrepancies are discussed in Section 3.3.3 and full list of ALHIC1901 sections used in this study (including the reference and replicate sample dimensions) is provided in Table 3.1.

3.3.2 Determination of similarity

We use multiple metrics to determine similarity between sample sets, depending on the scale of the comparison. Details for each metric are described below.

Variability metrics for regional survey

We first consider the overall distribution of δ^{18}O and d_{excess} at seven sites across the Allan Hills[1]. We expect that core sites that include layers of similar spatiotemporal origin – even if no longer chronologically ordered – will contain a similar distribution of water isotope

[1]Note that we do not include published cores S27 or ALHIC1903 (Spaulding et al., 2013; Carter et al., in review) in these analyses because previous work has established that they are significantly younger than other cores and because published S27 data does not include δ^{18}O or d_{excess}.

Section ID	**Reference Sample Length (cm)**	**Replicate Sample Length(s) (cm)**	**Top Depth (m)**	**Bottom Depth (m)**	**Field-Logged Length (cm)**
201-2	26	26	135.525	135.755	23
201-4	26	26	135.945	136.145	20
203-2	26	26	137.045	137.315	27
203-3	23	23	137.315	137.515	20
204-4	23	24	138.085	138.285	20
204-5	24	21	138.285	138.495	21
207-1	16	16	138.915	139.085	17
207-3	11	10	139.215	139.305	9
207-5	7	6	139.395	139.505	11
207-6	4	8	139.505	139.535	3
207-7	10	7	139.535	139.635	10
207-9	9	9	139.725	139.835	11
208-3	7	7	139.935	140.035	10
208-8	11	10	140.435	140.535	10
209-3	9	9	140.725	140.825	10
209-7	19	19	141.055	141.265	21
209-8	9	7	141.265	141.365	10
210-2	7	7	141.445	141.505	6
228-4	21	28, 24	155.065	155.355	29

Table 3.1: All sections of ALHIC1901 measured with 1-cm resolution for this study and corresponding depth intervals.

values, and we quantify this similarity between cores as the intersection of the integral of the probability density function (PDF) for all isotope data at that site, as indicated by Equation 3.1.

$$S_{1,2} = \int_{-\infty}^{\infty} \min\left(\hat{f}_1(x), \hat{f}_2(x)\right) \, dx \tag{3.1}$$

where $S_{1,2}$ is the overlap between the distributions of δ^{18}O at any pair of ice-core sites, and $\hat{f}(x)$ is an estimate of the probability density given by the kernel density equation (see, e.g., Silverman, 1986). This metric quantifies the percentage of isotopic (and possibly isochronal) overlap between core sites, regardless of stratigraphic ordering.

For cores along the flow-line transect shown in Figure 3.1, we additionally consider the cross-correlation of the water isotope profile with depth to determine if the ordering of information is preserved over inter-core distances of 8 to 140 m. Because earlier work has found the oldest ice layers near the bed at all sites (see, e.g., Yan et al., (2021); Shackleton et al., (submitted)), we normalize the depths of all cores to align the measurements at the bed. We align all core depths by δ^{18}O to find the highest correlation coefficient for each pair and adjust the sample depths as indicated by Equation 3.2:

$$depth_{adjusted} = k_{scaling} \times (depth_{original} - depth_{bedrock}) + depth_{normalized-bed} + lag \tag{3.2}$$

where $k_{scaling}$ is determined by maximizing the cross-correlation of δ^{18}O, and cores are aligned to within 5 m (maximum lag value) of an arbitrary normalization depth of 200 m. Here, the Pearson coefficient quantifies the strength of the linear association between the δ^{18}O profile at any two core sites, and we interpret a positive correlation as evidence of repeated packets of ice with similar ordering between core sites.

Variability metrics for 1-cm data

For 1-cm samples with variability greater than the analytical error, we also cross-correlate the δD signal to identify optimal values of $k_{scaling}$ and lag as described by Equation 3.3:

$$depth_{adjusted} = k_{scaling} \times depth_{original} + lag \tag{3.3}$$

We primarily focus on δD (rather than δ^{18}O) for these 1-cm data due to the slightly higher signal-to-noise ratio. Here, we test a range of values for $k_{scaling}$ (0.8 to 1.2) and a range of values for lag. We allow lag to be $\pm$(total section length $-$ 5cm) to ensure that at least 5 cm of data remain for each correlation. We align the replicate measurements with the reference measurements (which, unless otherwise noted, are indicated in blue as in 3.2) to optimize the correlation coefficient. Where these metrics are insufficient due to low variability or small section lengths, we assumed a scaling factor of 1 and identified the optimal signal lag to reduce the residual differences between isotope values. In a few instances where no overlapping isotope values were observed in the replicate sample set, such as in section 208_3, the assigned adjustment reflects a minimum lag, not an optimal lag.

Because the azimuthal orientation of ALHIC1901 was not preserved or logged while drilling, the sample sets used for this study do not represent spatially continuous data series but rather randomized pairings of section samples with the horizontal spacing indicated in Figure 3.2; that is, the reference measurement of one section has no fixed relationship to the reference measurement of an adjacent sample (except where otherwise noted), but is always 17-24 cm along the horizontal plane from the corresponding replicate sample (as indicated by Figure 3.2). In this way, our data are not biased toward a specific azimuthal position within the core; instead the paired measurements represent a random distribution of horizontal pairs. Because of this, we treat each set of measurements within a section independently.

3.3.3 Error estimation

We use the metrics described above to quantify the similarity between spatially separated isotope records and then to use the depth differences between those records to infer observations about the native blue ice environment such as the degree of layer dip or layer asymmetry. To verify that these differences are glaciological observations and not errors im-

parted during any step of the sampling or analytical process, we must carefully account for the sample depth, especially for the 1-cm data. The estimated magnitudes of uncertainties associated with these data are described below.

Sampling bias

As shown in Table 1.2, depth intervals and sampling intervals for these cores are nonuniform. While comparing the distribution between core sites, it is necessary to account for possible bias in sampling frequency. To do this, we conduct a bootstrapping experiment to determine a 95% confidence interval for the distribution. We randomly resample all datasets 1000 times, then bin and average all data before estimating the PDF for each core. The overlap ($S_{1,2}$) calculated from these experiments uses the mean value of all resampled data (n=1000).

Bandsaw cutting

While the bandsaw blade was set at 1-cm for all cuts, slight deviations in the bandsaw blade position could bias cut intervals larger or smaller than the intended 1-cm cut dimensions. The cut uncertainty is smaller than L^{-1}, where L is the section length, and well-matched laboratory measurements of each section with the subsample counts verify that our cutting tolerance was less than 0.04 cm during this study.

Depth interpolation

Differences between field-logged core dimensions and the subsample dimensions require subjective interpolation choices that impart the largest uncertainty on initial depth assignments. For example, due to sample asymmetry, section ALHIC1901_207_6 is logged at 3 cm, but the reference measurement contained 4 1-cm samples and the replicate measurement contained 8 1-cm samples. This means that the relative offset between the reference and replicate measurements due to interpolation is ±4 cm, which is the largest absolute error for any data pair. The average of all such errors is 0.9 cm.

Oblique cuts along core

A related source of uncertainty in depth assignments arises from the initial cuts of large-diameter, non-cyllindrical core sections: when positioning each core section in the tray for horizontal bandsaw cutting, it is possible that the core is not always positioned in perfect alignment with the tray. A cut that deviates a few centimeters from the vertical axis of the core could cut through isochronal layers at a different angle than the second cut, potentially causing length discrepancies as described in the previous paragraph, and also causing apparent stretching of internal layers and introducing error to $k_{scaling}$. This uncertainty also decreases with sample length since it is related to an offset in the cutting angle, the likelihood for which decreases as length increases. We calculate this uncertainty as $\cos(\theta)^{-1}$, where θ is the angle of offset, and find that even with a relative offset as high as 20°, the scaling error would be $< 7\%$. Notably, we find some of the highest values of k_{lag} in sections where the sample length exceeds the diameter of the core, and where this magnitude of angular offset is unlikely.

We interpret observations of scaling factors and vertical offsets (i.e. non-zero lags in Equation 3.3) that exceed these estimated handling errors as meaningful quantification of blue ice deformation.

3.4 Water isotope similarity at kilometer and centimeter scales

We find significant similarities between the water isotope averages observed at each core site and we find that over small distances (i.e. centimeters to hundreds of meters) water isotope signals can be matched in magnitude and pattern with corresponding samples from similar depths off the bed in other locations. We show that blue-ice core samples at both centimeter- and 100-meter-scales can be aligned and that significant horizontal heterogeneity is likely due to the steeply dipping bed topography and complex up-gradient flow of ice.

3.4.1 Water isotope distribution

First we examine the water isotope distribution of all Allan Hills ice cores noted by Figure 3.1; data plotted by depth and the isotope distributions for δ^{18}O and d_{excess} are shown in Fig-

ure 3.3; the mean and standard deviation of all cores is provided in Table 3.2. Qualitatively, we find that geographically similar core sites contain similar mean values, suggesting that ice oriented along the indicated flow-line on Figure 3.1 is largely of similar meteorological and glaciological origin. Notably, ALHIC2301 – which is geographically isolated from the other core sites in the "cul de sac" area of the Allan Hills, is composed of more negative δ^{18}O and higher d_{excess} values, and site ALHIC1903 contains more negative values of both δ^{18}O and d_{excess} as well as significantly younger ice than the other cores examined (Carter et al., in review). While ALHIC1903 is not included in this analysis, these values are shown in Table 3.2 for reference.

We quantify the similarity as $S_{1,2}$ in Equation 3.1, and provide a matrix that shows all inter-core values in Figure 3.4. Because not all cores are sampled at all depths, we first normalized all core data by local bedrock depth, such that the data are binned by. We then restrict the comparison between any two sites to shared normalized depth intervals, and calculate the overlap as in Equation 3.1. Figure 3.4 highlights similar PDF values at all sites where overlapping adjusted depth intervals are available; values range from 27% to 89% in δ^{18}O and from 40% to 91% in d_{excess}, with a weak negative trend between the inter-core distance and the isotope similarity. We also tested the correlations of these same data, but none are statistically significant when data are binned as described.

3.4.2 Cross-correlation of cores along a flow line

Cores ALHIC1502, ALHIC1503, ALHIC1901, and ALHIC2201 were drilled within a few meters of the transect shown in Figure 3.1. Figure 3.4 suggests that these cores have especially similar composition, with PDFs capturing 58%-89% similar values for δ^{18}O and a similar range for d_{excess}. For these cores, we cross-correlate the δ^{18}O signal to find adjusted depths and scaling factors as described by Equation 3.2. The optimal values of scaling coefficients are provided in Table 3.3. These adjustments are applied to the distributions and depth profiles shown in Figure 3.5, and the resulting relationships between each pair are shown in Figure 3.6.

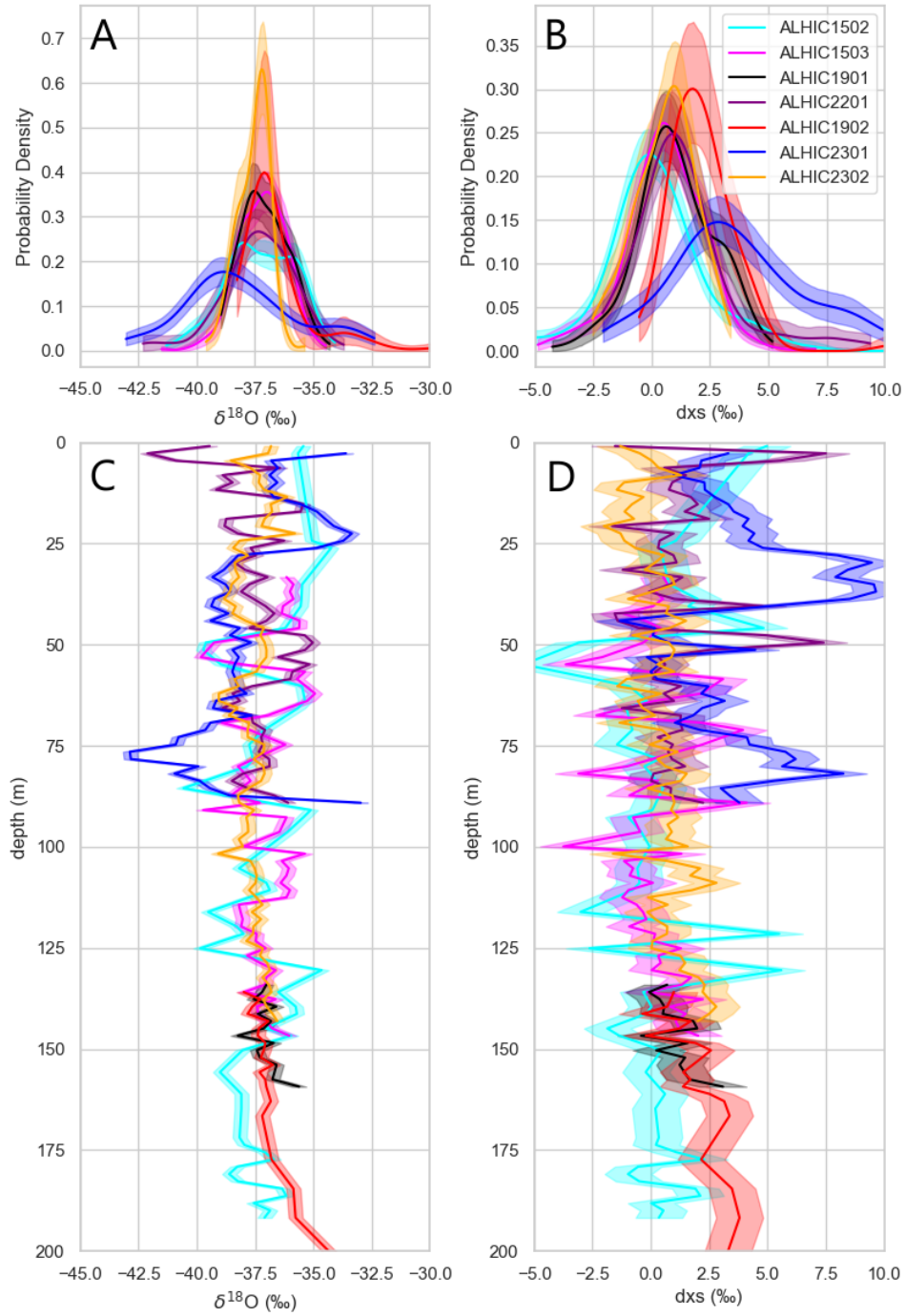

Figure 3.3: δ^{18}O and d_{excess} data for Allan Hills cores containing ice >1 Ma. **A)** Estimated PDF of δ^{18}O distribution (solid lines) with 95% confidence (shaded regions). **B)** Estimated PDF of d_{excess} distribution (solid lines) with 95% confidence (shaded regions). **C)** δ^{18}O profile (binned and averaged to 1.5 m) by depth, shown with analytical uncertainty as colored shading. **D)** d_{excess} profile (binned and averaged to 1.5 m) by depth, shown with analytical uncertainty as colored shading.

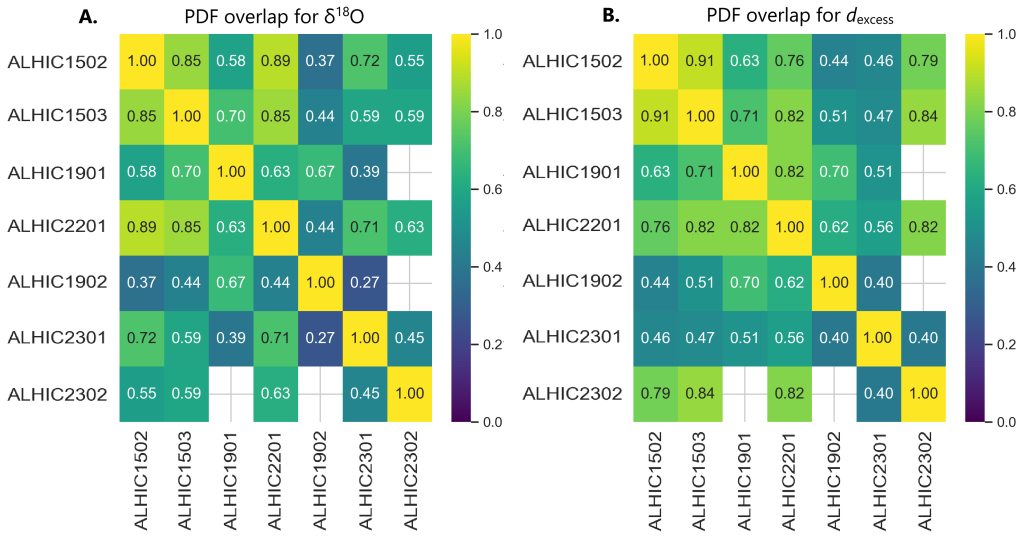

Figure 3.4: Similarity indicators for all pairs of cores, using data that have been binned and averaged to 1-m intervals and adjusted to the bed elevation. Note that only depth intervals that contain data for both cores are included in each analysis. **A)** Matrix of ice-core pairs colored by the intersection of δ^{18}O PDFs. **B)** Matrix of ice core pairs colored by the intersection of d_{excess} PDFs. Note that ALHIC1901/2302 and ALHIC1902/2302 do not contain overlapping depth intervals and are therefore excluded from analysis.

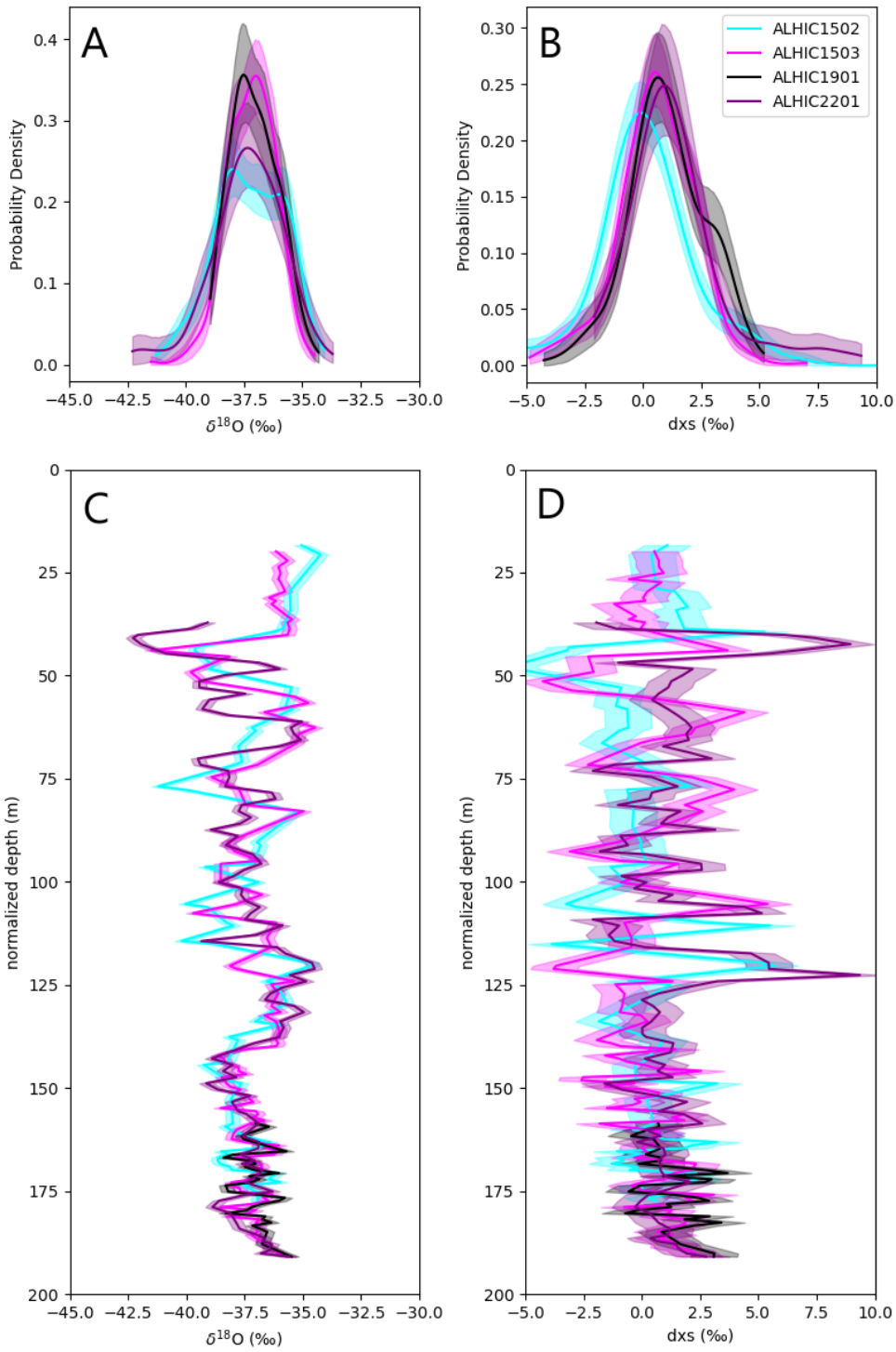

Figure 3.5: δ^{18}O and d_{excess} data along the transect indicated by 3.1 **A)** Estimated PDF of δ^{18}O distribution (solid lines) with 95% confidence (shaded regions). **B)** Estimated PDF of d_{excess} distribution (solid lines) with 95% confidence (shaded regions). **C)** δ^{18}O profile (binned and averaged to 1.5 m) by depth, shown with analytical uncertainty as colored shading. **D)** d_{excess} profile (binned and averaged to 1.5 m) by depth, shown with analytical uncertainty as colored shading.

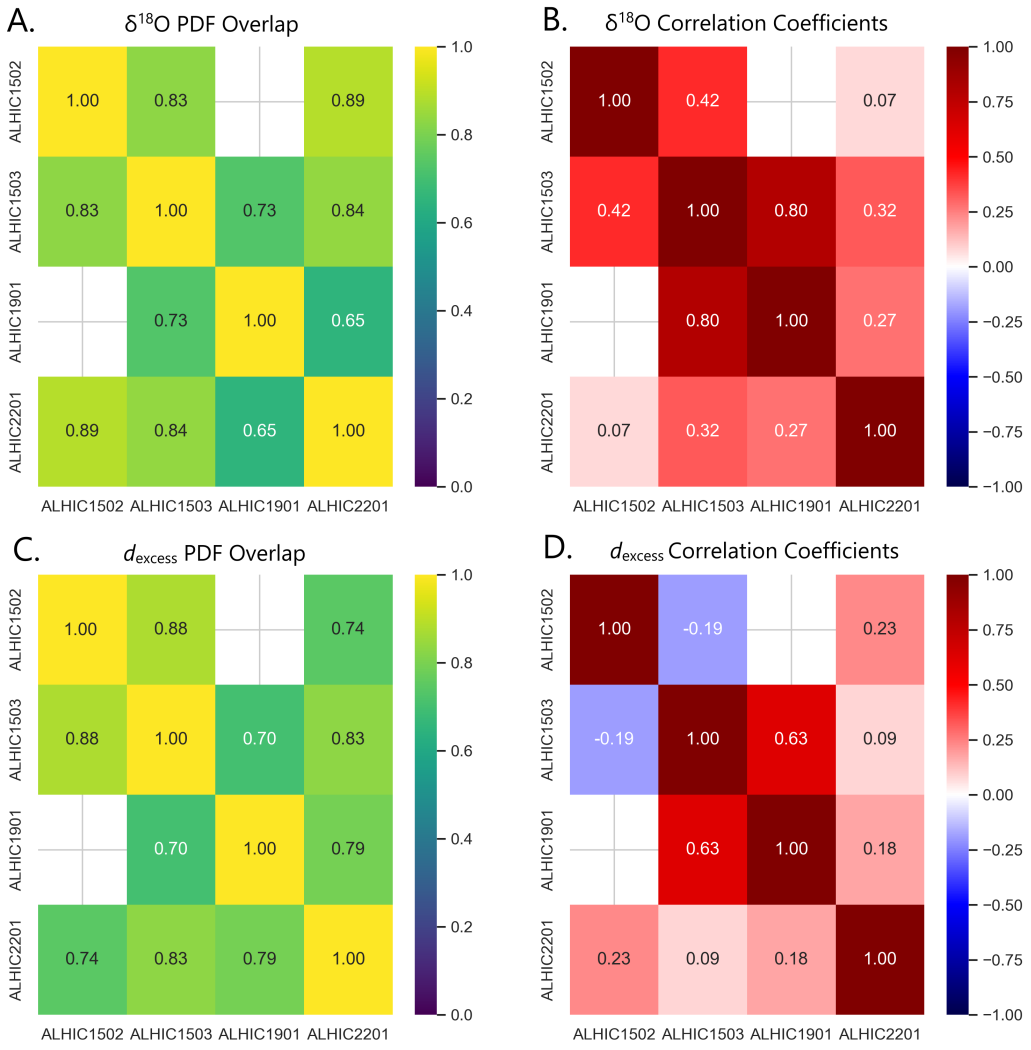

Figure 3.6: Similarity indicators for paired cores along a flow line, using depths determined by cross-correlation of δ^{18}O. (A) Matrix of ice core pairs colored by the intersection of δ^{18}O PDFs for corresponding adjusted depths. (B) Matrix of ice core pairs colored by the correlation of δ^{18}O for corresponding adjusted depth intervals. (C) Matrix of ice core pairs colored by the intersection of d_{excess} PDFs for corresponding adjusted depths. (D) Matrix of ice core pairs colored by the correlation of d_{excess} for corresponding adjusted depth intervals. Note that little overlapping information between the ALHIC1901/ALHIC1502 pair is available and it is therefore excluded from this analysis.

3.4.3 Cross-correlation of 1-cm measurements along ALHIC1901

At a smaller scale, we also find coherent isotope patterning between paired subsamples of ALHIC1901. We apply a depth adjustment in accordance with Equation 3.3 to optimize the Pearson coefficient, and then linearly interpolate along the $depth_{adjusted}$ vector such that

$$\delta D_{\text{original}} = f(\text{depth}_{\text{original}}) \quad \text{and} \quad \delta D_{\text{adjusted}} = f(\text{depth}_{\text{adjusted}}) \tag{3.4}$$

We highlight some examples of the cross-correlation process at this scale in Figure 3.7. Fig. 3.7 shows two end-member cases of $<$ 900 ka ice and the $>$ 1 Ma section. Fig. 3.7a-c shows a section with notable isotope patterning (ALHIC1901_209_7) where a near-perfect correlation is achieved at r = 0.99 ($0.98 < r < 1.0$, 95% confidence). Fig. 3.7d-f shows two adjacent sections where, due to overlapping isochrons in the replicate data series, all data from sections ALHIC1901_203_2 and ALHIC1901_203_3 were adjusted relative to the reference measurement of ALHIC1901_203_2 before cross-correlating; the best correlation was found to be r = 0.77 ($0.54 < r < 0.83$, 95% confidence). Fig. 3.7g-i shows the three dimensions of ALHIC1901_228_4. All isotope-aligned data are presented in Figure 3.8, and the lag and scaling factors are shown in Figure 3.9 and are discussed below.

Figure 3.8 demonstrates that high-frequency information is contained within this disturbed blue-ice core, and shows that similar isotopic layers are observed across distances of 17-24 cm (r = 0.72 for all adjusted data in both δD and δ^{18}O). The correlation coefficients and residuals for all sections are shown in Figure 3.9. Figure 3.9 also shows the reduction in δD residuals between $\delta D_{original}$ and $\delta D_{adjusted}$ ($\sigma_{original}$=7.8‰ and $\sigma_{adjusted}$=6.0‰).

3.5 Implications for layer dip, ice flow, and sample handling

Water-isotope signal coherence shows that that same-age packets of ice likely extend over hundreds of meters in the Allan Hills and that climatic information is generally reproducible across a single core. The imperfect correlations and nonzero residuals of the aligned datasets suggest that the horizontal heterogeneity cannot be explained by a simple linear

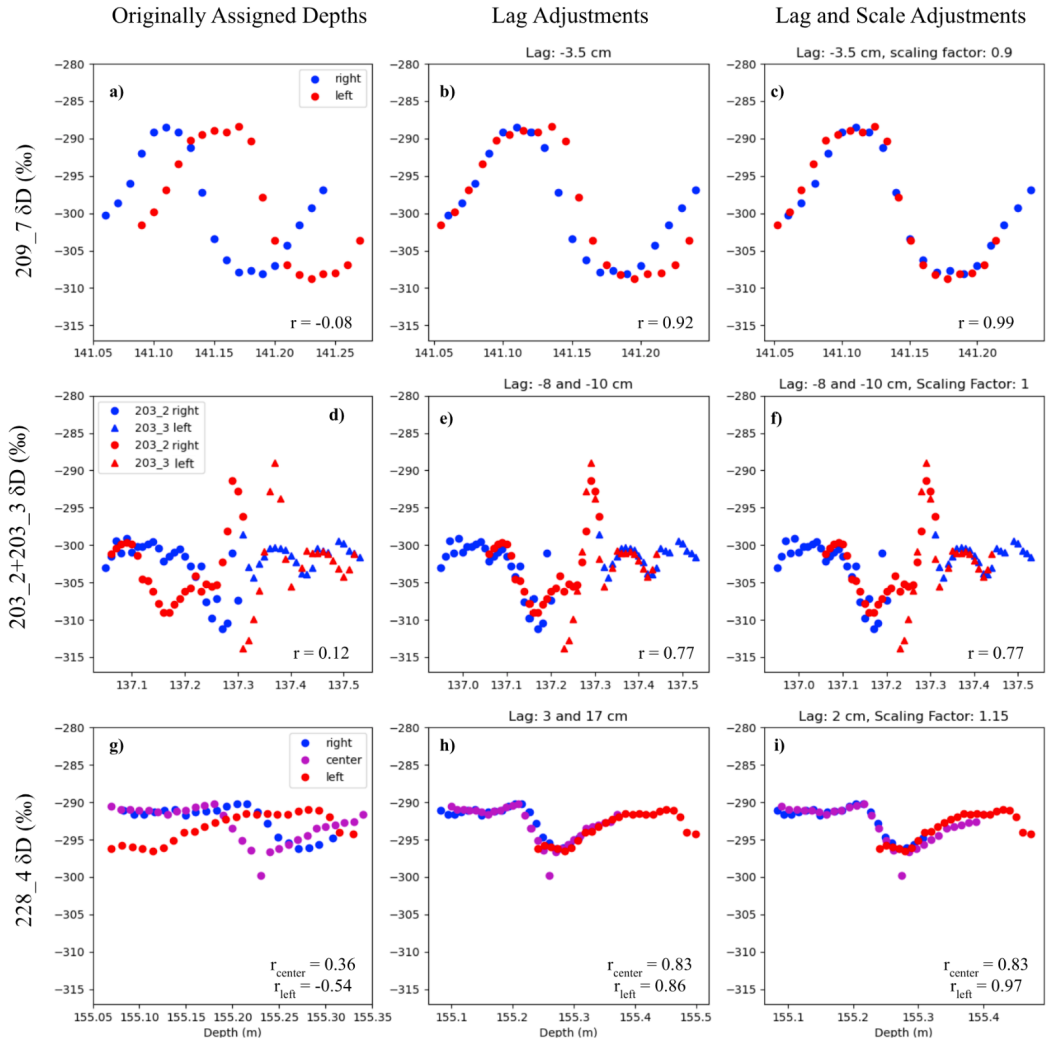

Figure 3.7: Signal adjustments used to identify depth offsets for sections 209_7 (top row), 203_2 & 203_3 (middle row), and 228_4 (bottom row). Panels A, D, and G show the correlation coefficients and data comparison using field-logged depths. Panels B, E, and H are the same, but depths are adjusted for the "left" replicate and "center" replicate data to maximize the correlation coefficient. Panels C, F and I are the same but allow for both signal scaling and signal lags. Note that there is no change between panels E and F because the optimal scaling factor is 1. Figure by Haley Lowes-Bicay.

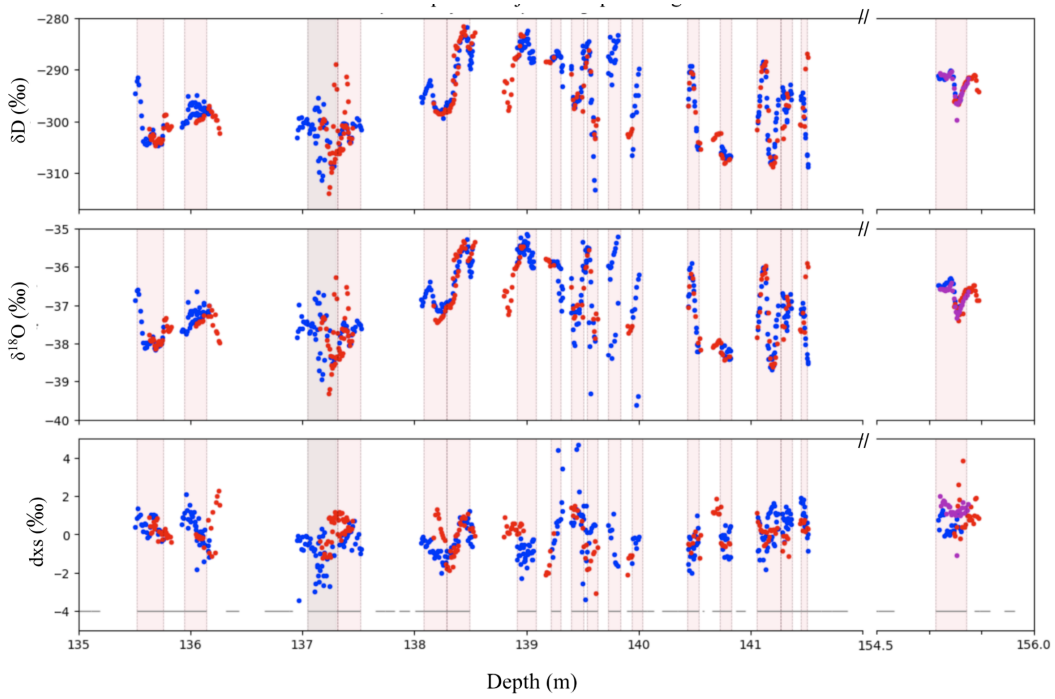

Figure 3.8: Isotope variations for all replicate sections of ALHIC1901. The shaded red boxes show depth_original for the replicate data; the shaded gray box highlights depth_original of section 203_2, where both samples were adjusted relative to the reference sample of section 203_3. The gray line at the bottom indicates all sections retrieved from this depth interval (recovery = 72.7%); note that not all recovered sections were available for this study. Figure by Haley Lowes-Bicay.

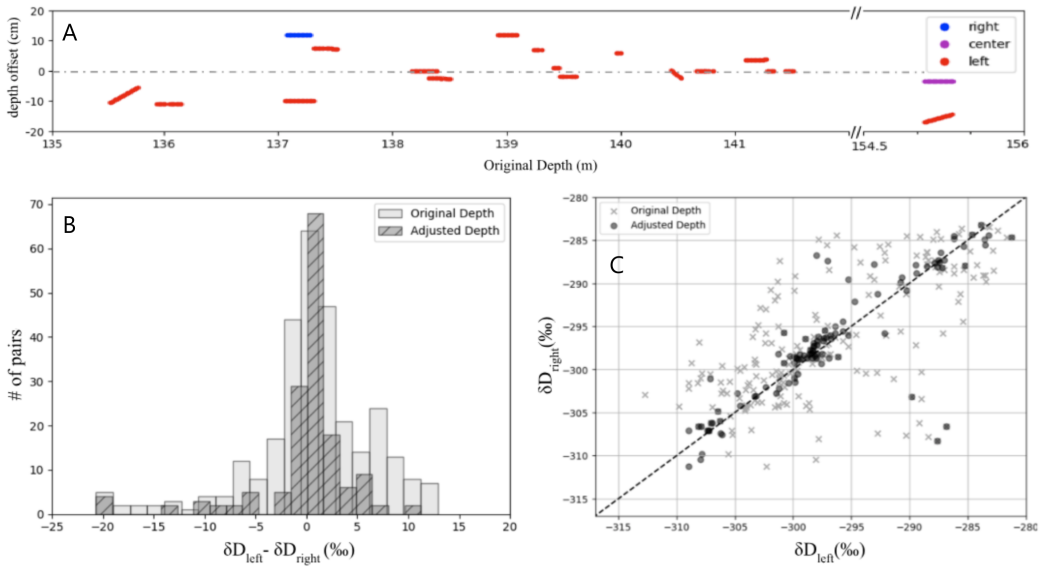

Figure 3.9: Calculated depth offsets and select cross-correlation metrics. **(A)** Total depth offsets (depth_original - depth_adjusted) in cm for all high-resolution samples. Colors indicate the dataset associated with each offset. **(B)**Histogram of residuals for both $\delta D_{original}$ and $\delta D_{adjusted}$. **(C)** Scatter plot showing the correlation for all <900 ka and >1 Ma ice for both $\delta D_{original}$ and $\delta D_{adjusted}$. The dashed black line represents r = 1. Figure by Haley Lowes-Bicay.

offset of isochrons for either kilometer- or centimeter-scale data, which is evidence of more complex deformation at these sites. Nonetheless, analyzing the discrepancies between paired measurements provides insight into the deformation of blue ice in this region.

Regional heterogeneity

Allan Hills ice cores exhibit characteristically similar water isotope distribution at most sites, with notable excursions in cul-de-sac core ALHIC2301 and downstream cores ALHIC1903 and S27. ALHIC2301 contains ice that is on average lower in δ^{18}O and higher in d_{excess} than most other sites; its unique isotope signature suggests that at least some ice in that location is transported through different meteorological or glaciological pathways (or both). The unique composition of ALHIC2301 is also apparent in Figure 3.3. Figures 3.3, 3.4, and 3.5 highlight the range and distribution of water isotopes in the Allan Hills, and indicate that there is a weak relationship of isotope similarity with distance, especially along the flowline. For 1-m averages along the transect, we find PDF overlap of 74±12% in δ^{18}O; this is reduced to 50%±11% by 1.5 km and is similar at distances of 3.5 km.

Similarly, correlation coefficients between pairs of cores along the flowline (i.e. Figure 3.6 suggest a reduction in similarity with distance, from r=0.80 at 8 m separation (i.e., ALHIC1901 and ALHIC1503) to r=0.07 at 140 m separation (i.e., ALHIC2201 and ALHIC1502). The $k_{scaling}$ values along the transect highlight thinning of similar packets as they move down the pressure gradient (i.e. uphill). However, it is worth noting that these linear scaling factors fail to capture nonlinear distortion between paired sites; nonlinearities can be observed in Figures B.1, B.2, B.3, B.4, and B.5, and could indicate instability in the historical ice flow direction. Between ALHIC1502 and ALHIC2201, layers seem to thin as they initially move towards the nunatak, but ablation from the top of the ice column combined with compression could modulate thinning at sites closer to the nunatak. Table 3.3 indicates the estimated depth of the ALHIC1502 surface layer along the flowline calculated from the thinning factors (i.e. $k_{scaling}$); as indicated, layers in ALHIC1503 and ALHIC1901 seem to thin more rapidly than the column thickness – suggesting that similar packets of

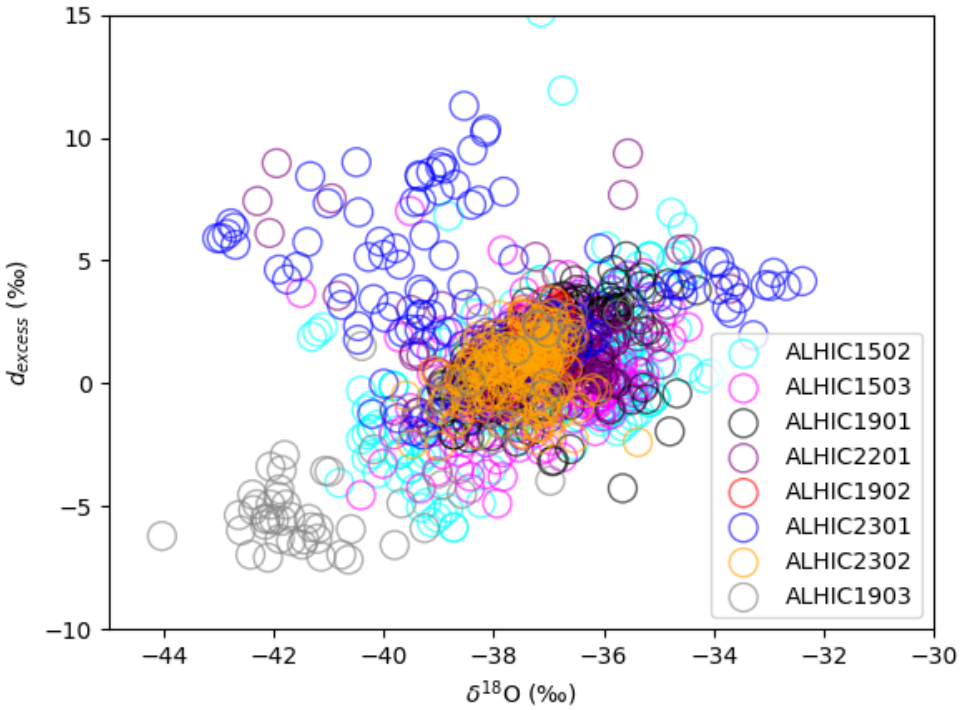

Figure 3.10: δ^{18}O vs. d_{excess} for Allan Hills core sites. Data sources are Yan et al., 2019 (ALHIC1502, ALHIC1503), Higgins et al., 2015 (ALHIC1503), Shackleton et al., submitted (ALHIC1901), Carter et al., 2024 (ALHIC1903), and this study (all remaining cores). The strong positive trend between most measurement pairs indicates a local meteoric water line for the accumulation site. Several cores, including ALHIC1502, ALHIC1503, ALHIC2201, and especially ALHIC2301, contain ice with isotopic values that fall above this line, and perhaps accumulated in a different location from typical Allan Hills ice.

Site	δ^{18}O mean (‰)	δ^{18}O σ (‰)	d_{excess} mean (‰)	d_{excess} σ (‰)
ALHIC2301	-38.0	2.4	3.7	2.9
ALHIC2302*	-37.6	0.7	0.5	1.2
ALHIC1902*	-37.2	0.4	1.6	0.9
ALHIC2201	-37.5	1.5	1.3	2.1
ALHIC1502	-37.3	1.5	0.3	2.3
ALHIC1503	-37.0	1.2	0.3	1.7
ALHIC1901*	-36.9	0.7	1.4	1.2
ALHIC1903	-40.1	2.1	-3.3	3.3

Table 3.2: Statistical data for all 1-m averaged ice core data compared by Figure 3.3 and ALHIC1903. An asterisk indicates core sites where depth intervals are not representative of the full ice column, leading to decreased variance. Ice cores are listed in order of their position to highlight trends in ice composition, which are particularly apparent for d_{excess}. Analytical error is approximately 0.1‰ for δ^{18}O and 1‰ for d_{excess}.

ice at the ALHIC1502 surface are tens of meters beneath the surface by this location – but ALHIC2201 layers are not significantly thinner despite its shallower bedrock conditions. Further, an example of evidence of nonlinear flow or a change in flow over time is at the top of the ALHIC1503 column, where we find approximately 31 m that are not isotopically represented at the top of the ALHIC1502 column.

ALHIC1901 heterogeneity

Our data show evidence of steeply dipping internal layers and nonlinear deformation over scales of several centimeters. After aligning all 1-cm data from ALHIC1901, we find that the linear depth offsets range from -12 to +21 cm, including scaling factors ranging from 0.79 to 1.28 (see Figure 3.9). These values far exceed the errors estimated in Section 3.3.3, lending confidence to our interpretation of these differences as evidence of glacial deformation. The signal differences are similar in both <900 ka and >1Ma ice, suggesting that deformation processes could be similar in the 135-142 m ice and at the bed, where the oldest ice samples

Core	distance from ALHIC1502 (m)	thickness relative to ALHIC1502 ($1/k_{scaling}$)	column depth (m)	estimated depth of ALHIC1502 top layers (m)
ALHIC1502	0	100%	200	0
ALHIC1503	56	58%	147	+31
ALHIC1901	60	67%	160	+26
ALHIC2201	147	56%	90	-20

Table 3.3: Table of core depth and thinning details along the transect. Distance is defined as the lateral distance from the ALHIC1502 core site. Relative thickness is provided as a percentage relative to ALHIC1502; a core with relative thickness of 50% would have layers with one-half of the thickness of ALHIC1502. The column depth is the observed column depth during coring or by geophysical observations, and the estimated depth of ALHIC1502 top layers is the theorized vertical position of the top of ALHIC1502 based upon on the relative layer thicknesses provided in the second column, where depth beneath the ice surface is defined in a positive direction. These calculations indicate ALHIC2201 layers with similar layer thickness to ALHIC1503 and ALHIC1901, despite persistent ablation that has removed 20 m of ice from the top of the column relative to ALHIC1502.

have been found (Shackleton et al., submitted). Linear offsets in depth can be attributed to layer dip; we identify a maximum apparent dip of 43° in these sections, which is similar to estimates of bedrock topography (Spaulding et al., 2012; Yan et al., 2019). Because azimuthal orientation was not logged during drilling, differences in apparent dip throughout these depths are not meaningful.

We interpret differences in signal scaling between the replicate sample sets (up to 28%) as evidence of asymmetrical thinning of isochrons, and we find that for many sections (such as 228_4 in Fig. 3c) nonlinear scaling even within a single section would be necessary to improve correlation values between cores. Although the magnitude of $k_{scaling}$ in 1-cm ALHIC1901 samples is similar to the magnitude of $k_{scaling}$ at the regional scale, it is not clear whether they are reflective of the same large-scale flow regime. If so, we would expect to see the largest values of $k_{scaling}$ in sample pairs that also experience the largest offsets; i.e. sample pairs that in-situ were oriented along the direction of dip and ice flow. We find the largest $k_{scaling}$ values in sample pairs from ALHIC1901_201_2 and ALHIC1901_228_4, both of which also see an isochronal offset greater than 10 cm across the sampling interval (see Figure 3.9). This leaves open the possibility that large-scale stress fields are imprinted upon layers at the centimeter-scale, though asymmetric deformation caused by rheological differences like boudinage, or more localized flow processes could also cause these changes.

These observations highlight the effects of three-dimensional deformation in blue ice layers and suggests that even if layer dip can be accounted for throughout these cores, developing high-resolution, multi-proxy records of same-age measurements will be nontrivial. Tools like multi-track electrical conductivity measurements (e.g. Kirkpatrick et al., 2024) and hyperspectral imaging (e.g. Garzonio et al., 2018; McDowell et al., 2024) will be useful for identifying the direction and magnitude of layer dip. Accounting for layer dip alone will correct for many of these discrepancies at the spatial scale that is required for the resolution of most analyses, but aligning all measured samples by their water-isotope composition will minimize alignment errors that arise from nonlinearities.

3.6 Summary

We investigated the reproducibility of water-isotope signals in seven cores across the Allan Hills region and in replicate measurements made from a 24-cm ice core. We demonstrate that the variability of water isotope data across the Allan Hills is similar between most cores, with notable differences observed at the geographically distinct cul-de-sac site ALHIC2301 and sites S27 and ALHIC1903. Along a flow-line transect, we find that the water isotope values with depth are correlated ($0.27 < r < 0.80$) and that all cores are characterized by essentially indistinguishable water-isotope compositions. This increases confidence that samples along this transect have similar origins, although additional material at the top of the ALHIC1503 column and missing material at the top of the ALHIC2201 column highlight the complex regional flow and provide evidence of historical ablation near the nunatak. We measured several sections of ALHIC1901 with 1-cm vertical resolution, establishing that high-frequency information is preserved in Allan Hills blue ice. We cross-correlated replicate cm-resolved water-isotope data to reveal steeply dipping layers (up to 43°) and significant asymmetry (up to 28%) within the core. The magnitude of dip and asymmetry observed at both scales is similar, suggesting that deformation at both scales is governed by ice flow over steeply dipping bedrock topography.

Chapter 4

INSIGHTS ON ALLAN HILLS CLIMATE AND SIGNAL PRESERVATION FROM A 4-MA, STRATIGRAPHICALLY DISTURBED, BLUE-ICE CORE

4.1 Overview

Blue ice cores from the Allan Hills region of Antarctica contain ice as old as 6 Ma, but the ice is stratigraphically disturbed and the distortion of the climate signal by post-depositional processes is not well characterized. Here, we consider whether high-frequency isotopic information recorded in Allan Hills ice is consistent with glacial-interglacial signal expectations. We present a new high-resolution (1-cm) water isotope record that spans 12 discontinuous (i.e., both incompletely recovered and not chronologically ordered) meters of Allan Hills core ALHIC1901 that have been dated at lower resolution by the ^{40}Ar geochronometer to 500 ka - 4 Ma. We compare these data with independent records from other ice cores and ocean sediment cores. We align high-frequency water isotope fluctuations with expected climatic variations based on the EPICA Dome C ice core record and the global benthic δ^{18}O stack, and demonstrate that the signal frequency is consistent with glacial-interglacial information within the error of the ^{40}Ar age scale. Confidence in this refined age scale is highest in ice 550 - 750 ka, where water-isotope variability is best preserved. We model the effects of sample averaging and molecular diffusion for this interval and demonstrate that molecular diffusion is necessary to obtain the degree of signal smoothing observed in ALHIC1901. Our data provide new constraints on glacial-interglacial accumulation rate changes (approximately 7 times more accumulation during interglacials between 550 and 750 ka) and layer thinning (>99.99% since deposition for ice 20 m above the bed). We show that the relationship between water isotopes in the Allan Hills and at Dome C has experienced a consistent rate of change since about 725 ka, suggestive of local isotopic cooling >5°C in the Allan Hills. We speculate that these changes could be attributed to an increase in snow redistribution from katabatic winds, an increase in local or upwind scour site elevation, or a combination of these processes.

4.2 Introduction

Blue ice areas form near mountainous regions in Antarctica, where the local topography slows ice flow and focuses katabatic winds, causing both net sublimation and flow of old ice towards the surface (Bintanja, 1999). In the Allan Hills blue ice area (BIA), ice hundreds of thousands of years old is found at the surface (e.g., Dunbar et al., 1995). However, depth-age relationships in BIAs are complex and exhibit folding and other stratigraphic disturbances that complicate the development of paleoclimate records (e.g., Petrenko et al., 2006; Sinisalo and Moore, 2010; Baggenstos et al., 2017). Allan Hills cores S27 and ALHIC1903 preserve chronological strata from the penultimate deglaciation (Spaulding et al., 2013; Carter et al., 2024), but older ice tends to exhibit more complicated age-depth relationships (e.g., Shackleton et al., submitted).

Ice from the Allan Hills BIA has the potential to extend the ice-core record beyond 800 ka. Absolute dating of atmospheric ^{40}Ar trapped in ice-core bubbles allows for the development of paleoclimate records from stratigraphically disordered blue ice cores (Bender et al., 2008; Higgins et al., 2015), yet considerable uncertainty remains in their ability to preserve high-frequency climate variability. Recent measurements of Allan Hills blue ice cores ALHIC1901, ALHIC1902, and ALHIC1903 demonstrate that long-term water isotope trends up to 6 Ma from stratigraphically disturbed blue ice cores broadly agree with other temperature proxies (Shackleton et al., submitted). However, the absolute age scale resolution is sample-limited and relatively coarse; currently, ALHIC1901 has the best resolved ^{40}Ar age scale, with median sample spacing of 0.28 m, ranging from 0.06 to 3.23 m (Shackleton et al., submitted). The age scale highlights the stratigraphic complexity of blue ice, with frequent age reversals and implied layer thicknesses that are highly variable; this irregular age-depth relationship combined with the volume-intensive absolute dating technique contributes to uncertainty in the amount of time represented by an individual sample. In addition, the uncertainty of the average gas age for dated samples is approximately 11% (Shackleton et al., submitted). Uncertainty in the average age assignment and limitations in the absolute

dating resolution limit the interpretation of high-resolution paleoclimate records from blue ice.

In addition to dating limitations, uncertainties in ice provenance and deposition conditions complicate the interpretation of many measurements. Recent work on ALHIC1901 identified an interglacial preservation bias in CO_2 (Marks Peterson et al., 2024), which could indicate that low glacial accumulation rates failed to capture glacial gases below bubble close-off during past glacial periods. The modern accumulation rate in the Allan Hills is estimated to be, at maximum, 0.0075 m a^{-1} over the last 600 years (Dadic et al., 2015), although large disparities in glacial-interglacial layer thicknesses (i.e., 1-2 orders of magnitude) are observed in Allan Hills ice cores S27 (Spaulding et al., 2013; Yan et al., 2021) and ALHIC1903 (Carter et al., 2024). Uncertainties in the deposition conditions are particularly problematic for the interpretation of the water-isotope signal because water isotopes reflect the integrated thermodynamic conditions of their atmospheric trajectory and are sensitive to evaporation, transport, and condensation site conditions (Merlivat and Jouzel, 1979; Jouzel and Merlivat, 1984; Markle and Steig, 2021) in addition to post-depositional alteration (e.g. Casado et al., 2018; Wahl et al., 2021). Interpreting the ice-core water-isotope record requires knowledge of local meteorological and glaciological conditions, but the complex atmospheric and glaciological flow conditions that cause the formation of BIAs also lead to accumulation rates, post-depositional alteration, firn processes, layer thinning, and water-isotope diffusion conditions that are not necessarily constant in time or space and are not well characterized in the Allan Hills. It is therefore not known whether or to what extent climate-scale water-isotope variability is retained by blue ice cores from this region.

Here, we compare high-resolution (1-cm) water-isotope observations from a well-dated, stratigraphically disturbed Allan Hills core (ALHIC1901) with the EPICA Dome C (EDC) ice-core record (Jouzel et al., 2009; Landais et al., 2021) and the globally stacked benthic $\delta^{18}O$ record (LR04; Lisiecki & Raymo, 2005), which provide estimates of climatic fluctuations as recorded in East Antarctica and in marine fossils, respectively. We model post-depositional thinning and diffusion and compare modeled results with ALHIC1901 observations to make

inferences about ice thinning, water-isotope diffusion, and depositional conditions likely affecting water-isotope composition in the Allan Hills. We demonstrate that the amplitude of water-isotope fluctuations observed in ALHIC1901 agrees with expectations for very thinned (i.e., 10^{-3} m ka^{-1}), 1-cm-resolved ice, but that a significant negative trend in Allan Hills isotope data since ca. 750 ka likely reflects a change in local depositional conditions since that time.

4.3 Developing water isotope records and regional expectations

We measure stable water isotopes ($\delta^{18}O$, δD, and d) from approximately 500-800 ka ice (135-142 m) and 1-4 Ma ice (155-160 m, terminating at bedrock) in ALHIC1901 and compare our data with expectations derived from EDC (Jouzel et al., 2009; Landais et al., 2021) and benthic $\delta^{18}O$ (Lisiecki & Raymo, 2005). Our goal is to investigate whether and how climatic information is archived in disturbed blue ice cores. We first refine the ^{40}Ar-age scale by aligning δD and d_{excess} with peaks in the global records within the error of the ^{40}Ar-age scale (Shackleton et al., submitted), and then comparing our high-resolution data with a synthetic ice-core history based on a modified EDC record that has been subjected to thinning, molecular diffusion, and 1-cm sample averaging. More details about the ALHIC1901 measurements and the synthetic Allan Hills core comparison are provided below.

4.3.1 High-resolution measurements of ALHIC1901

We measured available sections of ALHIC1901 from 135-142 m and from 155-160 m by laser spectroscopy (Picarro L2140-i (Steig et al., 2014) and Picarro L2130-i). Each section was sampled with 1-cm vertical resolution, and the resulting 266 samples were melted in sealed high-density polyethylene bottles at 4°C. After melting, a 200-µL aliquot of sample water was pipetted into a glass vial with a septum. The vials were loaded alongside four internal reference waters into an autosampler for high-precision measurement by laser spectroscopy (following Schauer et al., 2016) and data were calibrated to the VSMOW-SLAP scale (Schoenemann et al., 2013). The root-mean-square errors of the fourth reference water

	δ^{18}O (‰)	δD (‰)	d_{excess} (‰)
WW	-33.82	-268.30	2.3
WGW	-39.77	-318.82	-0.7
SPS	-46.96	-365.01	10.7
VW	-56.60	-438.65	14.2

Table 4.1: Table of internal reference water values used to calibrate data used in this study. WW is meltwater from West Antarctic ice core WDC06A. WGW is glacial meltwater from the WDC06A core. SPS is surface snow from the South Pole. VW is meltwater from the Vostok ice core.[2]

are less than 0.1‰ for δ^{18}O, 0.6‰ for δD, and 1‰ for d_{excess}. Calibration and reference water details are provided in Table 4.1.

The analytical data are shown by depth in Figure 1. The data are generally in good agreement with measurements from Shackleton et al. (submitted), which are larger samples from distinct depth intervals; this agreement supports the application of the Shackleton et al. (submitted) age scale to these data. Figure 4.1 establishes that there are high-frequency water isotope fluctuations preserved in this very thinned, disturbed, and discontinuous blue ice.

4.3.2 Age scale refinement

A shared age scale is necessary to compare ALHIC1901 and EDC data, but the available age-depth constraints for ALHIC1901 are not sufficiently resolved for direct application to the ALHIC1901 1-cm data. At present, ALHIC1901 has the best resolved age scale for disturbed ice in the Allan Hills, so these sections of 500-800-ka ice present the best opportunity for an age-constrained comparison with EDC. However, the scale of interest in our samples (0.01 m) is much finer resolution than the existing age scale (where the mean$\pm\sigma$

[2]Additional information about UW Isolab internal reference waters is available at https://isolab.ess.washington.edu/resources/standards.php#water

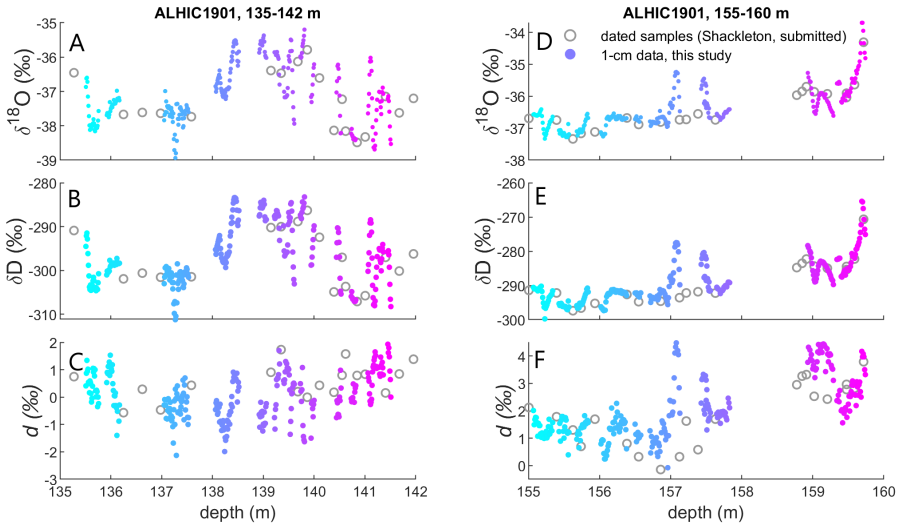

Figure 4.1: ALHIC1901 data by depth in meters. 1-cm vertically resolved measurements are shown as filled circles colored by depth. Grey circles indicate isotope values of larger-volume, dated samples presented by Shackleton et al. (submitted). A) δ^{18}O for 135-142-m ice. B) δD for 135-142-m ice. C) d_{excess} for 135-142-m ice. D) δ^{18}O for 155-160-m ice. E) δD for 155-160-m ice. F) d_{excess} for 155-160 m ice.

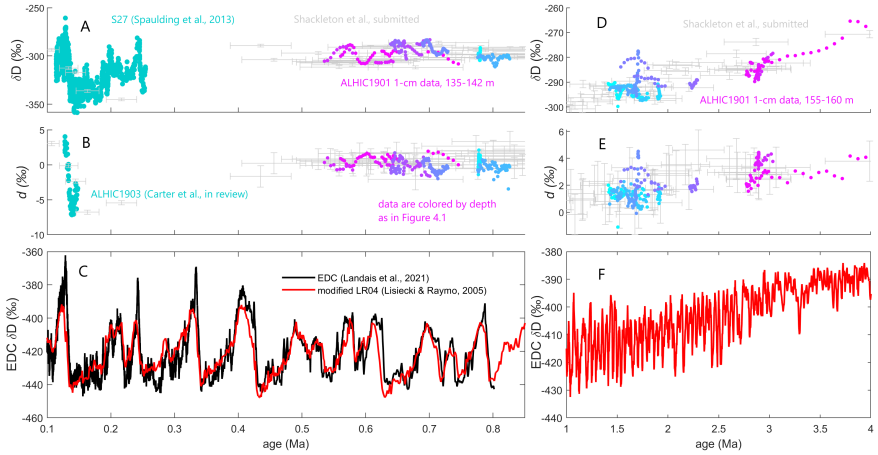

Figure 4.2: ALHIC1901 data by age, using a simple linear interpolation along the Shackleton et al. (submitted) age scale. Data from this study are colored according to the depth profiles provided in Figure 4.1. A) Allan Hills δD for 100-850 ka, including δD from 135-142 m. δD for S27 is published in Spaulding et al., 2013. B) Allan Hills d_{excess} for 100-850 ka, including d_{excess} from 135-142m. d_{excess} for ALHIC1903 is available from Carter et al., 2024. C) δD for 100-850 ka from EDC (Landais et al., 2021) (black line) and benthic δ^{18}O from Lisiecki & Raymo (2005) which has been aligned to EDC δD according to Equation 4.3.1. D) Allan Hills δD for 1-4 Ma, including δD from 155-160 m. E) Allan Hills d_{excess} for 1-4 Ma, including d_{excess} from 155-160 m. F) benthic δ^{18}O for 1-4 Ma from Lisiecki & Raymo (2005) which has been aligned to EDC δD according to Equation 4.3.1.

for our sampled interval is 31±31 cm). A simple linear interpolation of our high-resolution measurements along the Shackleton et al. (submitted) age scale is shown in Figure 4.2. Fig. 4.2 highlights the difficulty of interpreting high-resolution information from blue ice; while climatic information is apparent, the timing and magnitude of the signal does not agree with expected climatic fluctuations.

We align all water-isotope records from the Allan Hills with other global records and note key differences in Allan Hills ice that must be accounted for in order to create a synthetic climate history for the Allan Hills. Figure 4.2 shows new ALHIC1901 measurements alongside existing data from ALHIC1901, ALHIC1902, and ALHIC1903 (Shackleton et al., submitted) and from S27 (Spaulding et al., 2013; panel A) and ALHIC1903 (Carter et al., 2024; panel

B). In addition, we show global climate records spanning both intervals in panels C and F, including the EDC record for δD and the benthic stack, which records both ice volume and global temperature for the past 5 million years (Lisiecki and Raymo, 2005). Here, the benthic δ^{18}O stack has been modified to approximate Dome C δD by the following equation:

$$LR04_{modified} = LR04 \times (-28.31) - 303.98‰ \tag{4.1}$$

where LR04 refers to the benthic δ^{18}O stack (Lisiecki and Raymo, 2005) and the slope and intercept were determined by linear regression with EDC δD. The standard errors of the slope and intercept are 0.7 and 3.1‰, respectively. For comparison of data older than 800 ka, we are primarily concerned with the timing of fluctuations and not the mean signal, since we cannot assume that mean trends in benthic δ^{18}O and Antarctic δ^{18}O are similar; nonetheless, we find good agreement between $LR04_{modified}$ and Allan Hills δD from 1 - 4 Ma. For ice younger than 800 ka – where no trend is observed in the mean EDC δD over time – the Allan Hills data exhibit notably different behavior, especially for data younger than about 700 ka; Allan Hills data are also about 100‰ less negative in δD than EDC. These differences are discussed further in Section 4.3.3.

We refine the ALHIC1901 ^{40}Ar-age scale by aligning isotope fluctuations within error with a combined EDC-LR04 record that includes all data shown in Figure 4.2c,f. Our age scale relies upon several key assumptions about the depth-age relationship. First, we assume that there are no large age excursions between ^{40}Ar tie points; that is, we assume that the ages of our samples fall between the adjacent, dated sections. We assume that the depth-age relationship within each core section (typically <20 cm) can be approximated as linear, and we linearly interpolate between the two depth-adjacent ^{40}Ar tie points. Then, to bring our data into best alignment with the EDC timescale, we shift our data within the error of the age scale ($\pm$11% of age) to maximize the correlation between EDC and ALHIC1901 measurements of δD. Although there is some uncertainty in the peak assignments owing to the similarity in scale between the age error and glacial periodicity, we reduce uncertainty by using the magnitude of d_{excess} to inform the direction of age-scale adjustments (i.e., we

shift data such that the variance of d_{excess} at a given age is minimized). The resulting age scale yields data that are reasonably well correlated with expectations for δD (r=0.67), δ^{18}O (r=0.67), and d_{excess} (r = 0.21) that are described in Section 4.3.3. The resulting records for δD and d_{excess} are provided in Figure 4.4.[3]

4.3.3 Creating a synthetic Allan Hills core record

We create a synthetic climate history for the Allan Hills by modifying global records to account for the observed difference in magnitude and the observed trend in mean value in the Allan Hills; we then apply this climate history to a synthetic core and model layer thinning and diffusion to explore possible pathways that could lead to the observed isotope variability in ALHIC1901. The magnitude of Allan Hills water isotopes is indicative of a warmer precipitation site than EDC. In addition, Figure 4.2 suggests a trend in the mean value of Allan Hills water isotopes over time, likely indicating a change in the depositional environment (e.g., perhaps due to cooling of the depositional site). To account for these differences in our synthetic record, we begin by adjusting the magnitude of the blended EDC-LR04 δD record to align with S27 (Spaulding et al., 2013). We then modify our synthetic water-isotope history by assigning accumulation, thinning, and diffusion histories, and compare the synthetic core record with our ALHIC1901 data.

Disentangling local and global climate signals

To establish a synthetic climate history for the Allan Hills, we first consider the effects of local climatic changes on other ice-core records to establish a framework for treating the linear trend observed in our data. Because the water-isotope composition of precipitation reflects the deposition site, long-term ice-core water-isotope records reflect both global climate and site-specific conditions. In the Allan Hills, disentangling local and global effects on the water-isotope record is complicated by uncertainty about ice origins; the apparent long-term

[3]Note that we focus on the comparison of δD throughout this manuscript, rather than δ^{18}O, due to the availability of δD data from Allan Hills ice core S27 that we use for both comparison and model calibration.

trend in δD shown in Figure 4.2 suggests that Allan Hills ice likely reflects both global and local processes. While we expect that ice recovered from Allan Hills cores has traveled, at minimum, about 20 km from the modern snow accumulation area (see Figure 3.1a; Spaulding et al., 2012; Kerhl et al., 2018), it is possible that the conditions at that site (or that the site itself) has changed over time, which complicates interpretation of the water-isotope signal. In Figure 4.3, we consider the relationship between water isotopes at several ice-core sites (including Allan Hills site S27) and EDC for records that span multiple glacial cycles. Figure 4.3 shows the difference in either δ^{18}O or δD calculated for each ice-core site as

$$\Delta\delta = \delta_{site} - \delta_{EDC} \tag{4.2}$$

and includes details for the linear regression at each site and the standard error of both slope and intercept. For cores drilled at or near ice divides, such as east Antarctic sites Vostok (Petit et al., 1999) and Dome Fuji (Watanabe et al., 2003; Uemura et al., 2012; 2018) – and even in Greenland at NEEM (Gkinis et al., 2020) – there is no significant trend in $\Delta\delta$ over glacial timescales. However, the EPICA Dronning Maud Land (EDML) core (shown in Figure 4.3e) was drilled on a gentle slope approximately 20 km downstream from a local ice divide (Stenni et al., 2009), and therefore reflects precipitation from a transient accumulation site that was warming (due to movement downgradient) throughout the sampled time interval. Figure 4.3h shows the reduced trend in a "corrected" δ^{18}O record for which Stenni et al. (2009) applied an ice-sheet elevation correction determined from a glaciological model (Huybrechts et al., 2007). A trend in δ data from Talos Dome is also attributed to a decrease in elevation over time (Crotti et al., 2022). Figure 4.3a shows the observed offset in δD between Allan Hills site S27 and EDC over approximately 140 kyears. In addition to a linear offset of 70-120‰, an age-dependent slope in the isotope residual suggests evidence of local cooling in the Allan Hills during this interval. To account for this local effect in our synthetic record, we begin with an age-dependent, linear adjustment that approximates $\Delta\delta$D in the form of $\Delta\delta \approx m \times age + b$. The slope and intercept of the adjustment are given by the linear regression shown in Figure 4.3a. We translate the blended

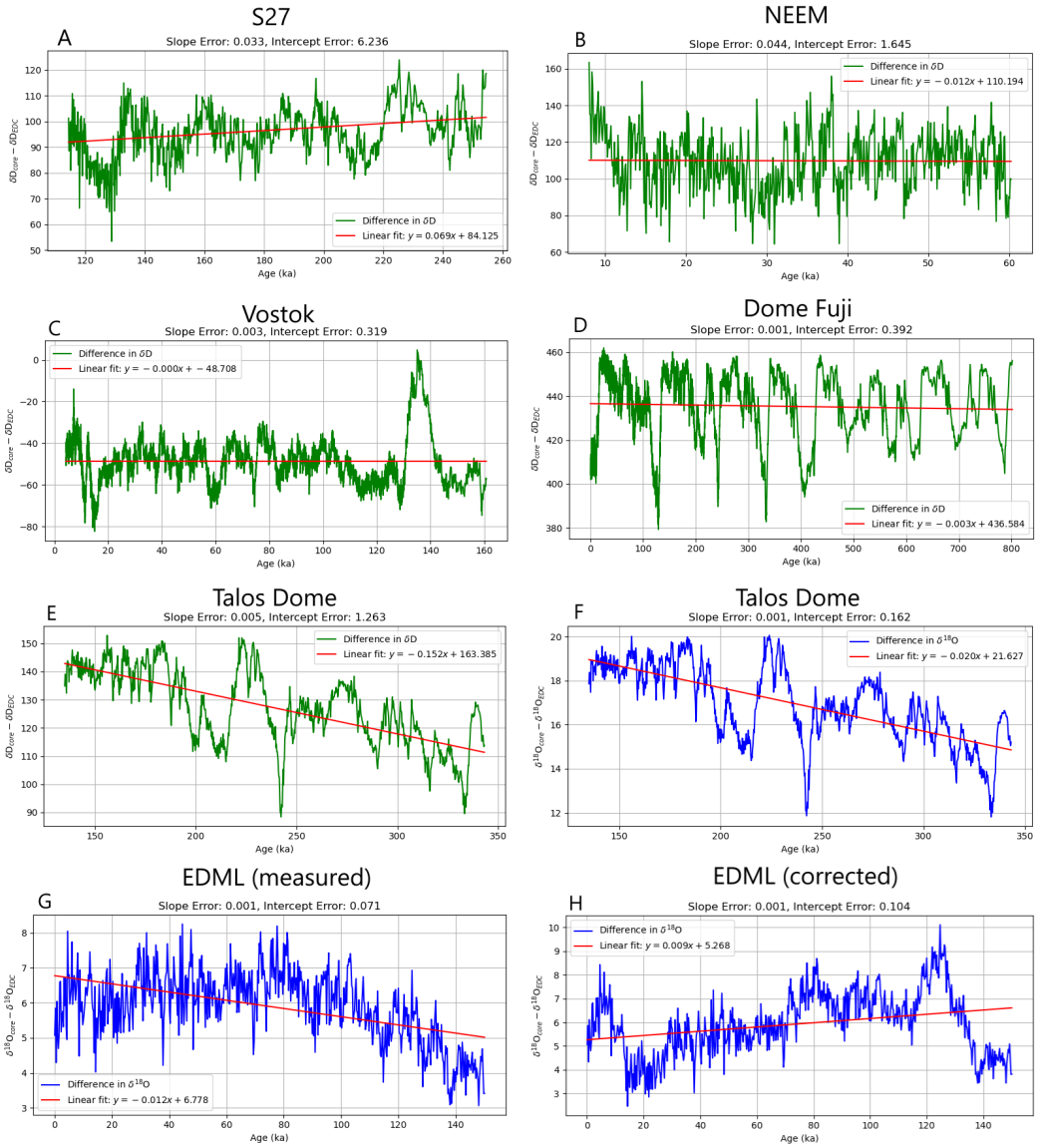

Figure 4.3: Isotopic difference between six ice-core sites and EDC, including a linear regression of $\Delta\delta$ residuals over time. δD are shown in green and δ^{18}O are shown in blue. A) S27 (Allan Hills), Spaulding et al., 2013. B) NEEM (Greenland), Gkinis et al., 2020. C) Vostok, Petit et al., 1999. D) Dome Fuji, Uemera et al., 2018. E-F) Talos Dome δD and δ^{18}O, Crotti et al., 2022. G-H) EDML as measured and EDML after correction for modeled elevation changes, Stenni et al., 2009.

EDC-LR04 record to align with Allan Hills water-isotope data by combining δD from EDC and from LR04$_{modified}$ with this adjustment:

$$\delta D_{\text{EDC-LR04-adjusted}} = \delta D_{\text{EDC-LR04}} + 0.07\,‰/\text{kyear} \times \text{age} + 84\,‰ \tag{4.3}$$

where $\delta D_{\text{EDC-LR04}}$ includes the combined records of δD from EDC and from LR04$_{modified}$, and where the slope and intercept are defined by the linear fit of $\Delta\delta$D shown in Figure 4.3a. The resulting record is plotted with the standard error (i.e., m$\pm$0.033 and b$\pm$6.2‰) as green shading in Figure 4.4 and is also used in all synthetic core experiments described below.

While $\delta\text{D}_{EDC-LR04-adjusted}$ agrees in magnitude with the ALHIC1901 1-cm δD data presented by this study for ages less than about 725 ka, agreement worsens between 725-900 ka. In addition, there are no published values for δ^{18}O or d_{excess} from S27; while these data exist for nearby core ALHIC1903 (Carter et al., 2024), they are limited to the penultimate deglaciation between 127-148 ka and are too narrow in age distribution to assess a long-term trend in δ^{18}O or d_{excess}. Therefore, we additionally consider differences between ALHIC1901 and EDC and find that the age-dependent relationship from $\Delta\delta\text{D}_{ALHIC1901}$ (135-142 m) is within the uncertainty of the relationship provided by Equation 4.3 for $\Delta\delta\text{D}_{S27}$. We use the slope and intercept from a linear fit of $\Delta\delta\text{D}_{ALHIC1901}$ and time to define a synthetic climate history for the Allan Hills for ages <800 ka:

$$\delta D_{synthetic-core<800ka} = \delta D_{\text{EDC-LR04}} + 0.053‰/\text{kyear} \times \text{age} + 87‰ \tag{4.4}$$

$$\delta^{18}O_{synthetic-core<800ka} = \delta^{18}O_{\text{EDC}} + 0.006‰/\text{kyear} \times \text{age} + 12.3‰ \tag{4.5}$$

where age is given in thousands of years. We find no trend in the relationship between $\Delta\delta\text{D}_{ALHIC1901}$ (155-160 m) and $LR04_{modified}$ (>800 ka), so we apply a simple linear offset for data >800 ka, which, combined with Equation 4.1 becomes

$$\delta D_{synthetic-core>800ka} = \delta D_{\text{EDC-LR04}} + 117‰ = LR04 \times (-28.31) - 187‰ \tag{4.6}$$

We also define an expectation for d_{excess} for ages less than 800 ka:

$$d_{excess-synthetic-core<800ka} = \delta D_{\text{synthetic-core¡800ka}} - 8 \times \delta^{18}O_{\text{synthetic-core¡800ka}}. \quad (4.7)$$

Synthetic climate histories for δD and d_{excess} are shown in Figure 4.4. We then assign these synthetic isotopic histories to a synthetic ice coree and investigate the effects of accumulation variability and thinning on signal damping within the synthetic core.

Estimating layer thicknesses in the synthetic core

Layer thicknesses dictate the frequency of climatic information in ice cores, which affects both the sampling resolution necessary to recover full climatic variability and also diffusive damping. Over time, diffusion reduces gradients in the water-isotope profile, reducing variability as the ice lattice deforms and molecularly reorganizes (Ramseier, 1967; Johnsen et al., 1969). We consider the effects of sample averaging and isotope diffusion on our synthetic core and specifically focus on ice from the 550-750 ka interval, where robust isotopic constraints in the 135-142 m ice lead to reduced age-scale uncertainty and where isotopic agreement between our measurements and synthetic history is greatest.

Variations in snowfall over time lead to differences in initial layer thicknesses within an ice core, and layers also thin under compressional strain after deposition; modeling smoothing due to molecular diffusion or sample averaging requires an estimate of accumulation rate and relative layer thicknesses for the synthetic core. The best estimate of modern accumulation at the Allan Hills is very low (0.0075 ma^{-1}; Dadic et al., 2015), although accumulation is probably spatially heterogenous and possibly up to an order of magnitude lower during glacial periods (Yan et al., 2021). Significantly thinned glacial layers during the penultimate deglaciation in Allan Hills core S27 (Spaulding et al., 2013) and a notable interglacial bias in gas data (Marks Peterson et al., 2024) are consistent with lower accumulation during glacial periods. While initial accumulation rates are poorly constrained, the final layer thicknesses can be inferred from the age scale.

At most ice-core sites, the accumulation rate is directly proportional to atmospheric temperature, so we define synthetic core layers with temperature-dependent relative layer

thicknesses. The Clausius-Clapeyron equation relates the saturation vapor pressure of water vapor to atmospheric temperature and can be written in the following form:

$$\ln(e_s) = -\frac{\Delta H_{\text{vap}}}{R} \cdot \frac{1}{T} + c \tag{4.8}$$

where e_s is the saturation vapor pressure, ΔH_{vap} is the heat of vaporization, R is the gas constant, T is temperature in K, and c is a constant. We leverage the first-order relationship between temperature and δD and the dependence of precipitation on atmospheric humidity to define relative layer thicknesses for the synthetic core as a function of δD. To do this, we use the empirical relationship between layer thickness and δD during the penultimate deglaciation at S27 in the form of Equation 4.8 to relate relative layer thicknesses to δD, and then assign relative layer thicknesses to the synthetic core according to the Allan Hills isotope expectations for δD:

$$\ln(\frac{1000}{m} \times \lambda) = -6647‰ \times \frac{1}{\delta D_{\text{synthetic core}}} \times x - 20 \tag{4.9}$$

where λ is the thickness of an annual layer in m, x is a dimensionless multiplier that we use to test the sensitivity to the slope, and the constants are empirically determined from S27 layer thickness and δD. Because this relationship assumes that no thinning has occurred in S27 since deposition (or that thinning has occurred equivalently at all depths), we expect that this estimate could be an underestimate of (deeper) glacial accumulation values, such that the relative λ difference applied to our record leads to a conservative estimate of interglacial biasing. Nevertheless, we test a range of relative layer thicknesses by testing slope multipliers (x) ranging from 0.4 to 1.0 in 4.9 to approximate glacial-interglacial layer differences of $\lambda_{interglacial} \approx 3.5 \times \lambda_{glacial}$ to $\lambda_{interglacial} \approx 26 \times \lambda_{glacial}$.

Low accumulation and ice thinning in the Allan Hills result in layer thicknesses on the order of 0.002 m ka^{-1} in <900ka ice from ALHIC1901, which is two orders of magnitude thinner than same-age layers at EDC, and three to four orders of magnitude smaller than estimated initial layer thickness in the Allan Hills (i.e., from Dadic et al., 2015; Spaulding

et al., 2013; Yan et al., 2021); the deepest ice in ALHIC1901 is even thinner. All diffusion experiments reported in this manuscript use a chronologically continuous synthetic core with a final thickness that matches the observed layer thicknesses of ALHIC1901 samples.

Estimating diffusion within the synthetic core

Post-depositional diffusion reduces isotopic gradients throughout the ice column, smoothing high-frequency climatic information over time. The effects of layer thinning and diffusion on the isotope signal are approximated by one-dimensional, Fickian diffusion:

$$\frac{\partial \delta}{\partial t} = D_{ice}\frac{\partial^2 \delta}{\partial z^2} - \dot{\epsilon}\frac{\partial \delta}{\partial z} \tag{4.10}$$

where $\partial\delta/\partial t$ is the change in water isotope composition (δ^{18}O or δD), D_{ice} is the temperature-dependent isotope diffusivity (discussed in more detail below), z is the depth position along the core, and $\dot{\epsilon}$ is the vertical strain rate, which defines the layer thinning (Johnsen et al., 1977). The cumulative effects of diffusion are sometimes quantified by the diffusion length, which quantifies the average displacement of a water molecule from its original position in the core (Gkinis et al., 2011; 2021). The diffusion length is typically considered to reflect the combined effects of displacement in the firn (σ_{firn}), where water vapor molecules are displaced along interconnected pore spaces near the surface, and displacement in solid ice (σ_{ice}), where water molecules are rearranged within the ice lattice (Johnsen, 1977; Whillans and Grootes, 1985; Cuffey and Steig, 1998). Firn diffusion is the dominant mode of isotope signal damping in typical ice cores, and diffusion in solid ice is generally thought to be less relevant except in ice near the bed, where layers are thinnest and temperatures are warmest (Johnsen et al., 2000; Grisart et al., 2022). However, diffusion lengths for water isotopes at the bottom of the EDC core are estimated to be 16-60 cm (Pol et al., 2010; Grisart et al., 2022); similar effects could cause significant damping or homogenization of the climate signal in extremely thinned Allan Hills ice, where apparent glacial cycles span only a few centimeters.

We solve for the effects of diffusion by convolving a gaussian filter G(z) with our simu-

lated core data, following the formulation below (Gkinis, 2011; Laepple et al., 2018; Gkinis et al., 2021):

$$G(z) = \frac{1}{\sigma_z \sqrt{2\pi}} \exp\left(-\frac{z^2}{2\sigma_z^2}\right) \tag{4.11}$$

where z is the sample depth and σ_z is the diffusion length. The diffusion length is given by

$$\sigma_z^2(\tau) = S(\tau)^2 \int_0^\tau 2D_{\text{ice}}(t) S(t)^{-2}\, dt \tag{4.12}$$

where τ is the age of each layer, $S(\tau)$ is the ice thinning function at each age, and $\mathrm{D_{ice}}$ is the water-isotope diffusivity in solid ice. Although accumulation rates, firn density profiles, and firn column thickness over these timescales are poorly constrained, it is likely that solid-ice diffusion governs signal smoothing in these samples, which are both near the bed and several orders of magnitude thinner than typical ice-core samples. In the EDC core, σ_{ice} begins to outpace the effects of σ_{firn} at around 2000 m depth, where the temperature of the ice is ~30°C and the layer thickness is about 30% of its initial thickness (Grisart et al., 2022). In the Allan Hills, observed layer thicknesses are orders of magnitude thinner than estimated accumulation rates, which amplifies the role of σ_{ice}. We therefore consider σ_{firn} to be negligible, such that $\sigma_z(\tau) = \sigma_{ice}(\tau)$. We also note that because are primarily looking for evidence of diffusion (and not trying to use the diffusion results to invert for historical conditions), even if σ_{firn} is not negligible, our interpretation would not be changed.

We adopt the conventional, empirically determined water isotope diffusivity given by Ramseier (1967) in the form of the Arrhenius equation:

$$D_{\text{ice}} = D_0 \exp\left(-\frac{Q}{RT}\right) \tag{4.13}$$

where $\mathrm{D_0}$=9.13cm^2/s, Q=59.820 kJ/mol, R is the gas constant and T is the temperature of the ice in K. We explore the effects of temperature, thinning rate, and differences in relative layer thicknesses to evaluate whether the Allan Hills water-isotope observations are consistent with glacial-interglacial transitions that have undergone diffusion.

4.4 Comparison of ALHIC1901 data with regional expectations

The analytical data on the refined age scale and the full synthetic climate history are presented in Figure 4.4 alongside other ice-core data from the Allan Hills for context.

4.4.1 Isotope agreement with synthetic climate history

The synthetic climate history is consistent in magnitude and signal amplitude with the S27 core (Spaulding et al., 2013), and also approximates the timing, magnitude and variability of available data from ALHIC1901, ALHIC1902, and ALHIC1903 for δ^{18}O, δD, and d_{excess} (from Shackleton et al., submitted; Carter et al., 2024; and this study). Perhaps surprisingly, the full range of variability suggested by $d_{excess\_synthetic-core<800ka}$ is observed in d_{excess} from the Allan Hills data, except for during marine isotope stage (MIS) 16 (approximately 650 ka). Variability in δD and in δ^{18}O (not shown) is slightly damped at all ages, capturing about 80% of the expected variability in ALHIC1901. Relatively constant δD measurements from 750-900 ka (see Figure 4.1) and adjacent age-invariant measurements of ^{40}Ar (see Figure 4.4a) suggest that either the ice above the recumbent fold is highly mixed or that ice at these depths is sampled along an isochron. Fully recovered variability in the d_{excess} signal points to a combination of mixing and diffusion, which is thought to be similar for δD and δ^{18}O (Ramseier, 1967) and thereby less significant for d_{excess}. Amplitude reductions caused by sampling bias and by diffusion are investigated in the next section.

4.4.2 Smoothing by sample averaging and molecular diffusion

We investigate sample averaging and water-isotope diffusion as possible causes of amplitude reduction in the ALHIC1901 1-cm data. The dominant control on signal smoothing due to sample averaging is the relative layer thickness, since layers that are thinner than the sampling resolution will be mixed with isotopically distinct, adjacent layers during sample analysis. The dominant controls on signal smoothing from diffusion are relative layer thickness, temperature, and layer thinning. Because historical information about these ice

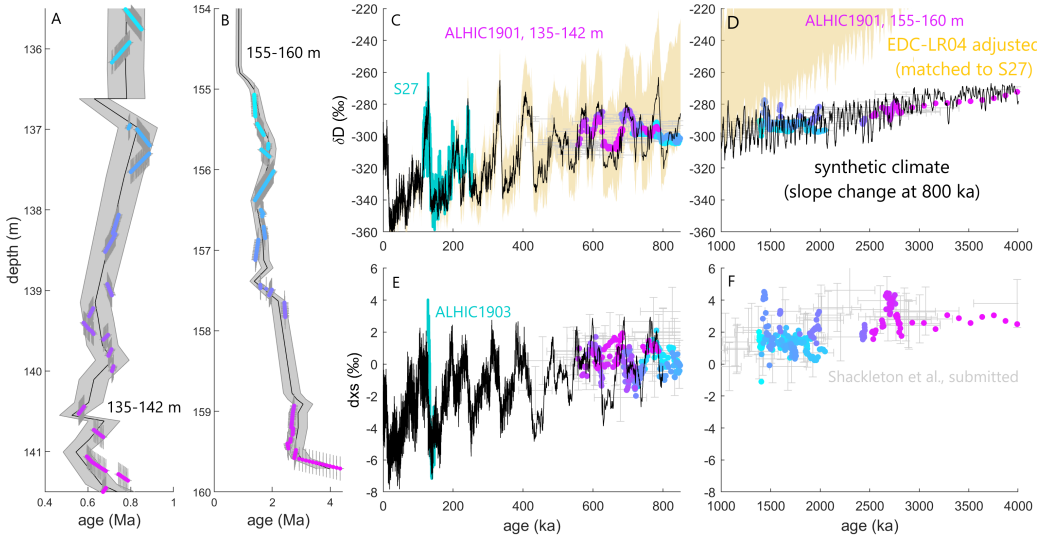

Figure 4.4: ALHIC1901 data for δD and d_{excess} on a refined depth-age scale. All 1-cm data from this study are colored according to the depth profiles shown in plots A and B (similar to Figures 4.1 and 4.2). A-B) ^{40}Ar-age and depth relationship (Shackleton et al., submitted; black line) with uncertainty (grey shaded region). ALHIC1901 depths are plotted with refined ages that have been adjusted within the measurement error as discussed in Section 4.3.2. Vertical error bars indicate one-half of the maximum isochron offset measured between same-depth samples in 135-142 m ice (see Lowes-Bicay et al. (in preparation) or Chapter 3 of this thesis). C) Comparison of Allan Hills δD with $\delta\text{D}_{\text{synthetic-core}}$. The gold shading shows $\delta\text{D}_{EDC-LR04-adjusted}$ as defined by Equation 4.3, representing an approximation of Allan Hills isotope expectations derived from the time-$\Delta\delta$ relationship shown in Figure 4.3a for residuals between S27 and EDC. The black line represents the synthetic core history as described by Equations 4.4 (younger than 800 ka) and 4.6 (older than 800 ka). Measurements from core S27 (Spaulding et al., 2013) are provided in teal, and dated measurements by Shackleton et al. (submitted) are provided as grey crosses. D) Same as C but for 1 Ma to 4 Ma. E) Allan Hills d_{excess} and $d_{excess\text{-synthetic core}}$, as described by Equation 4.7. Measurements from core ALHIC1903 (Carter et al., 2024) are provided in teal, and dated measurements by Shackleton et al., submitted are provided as grey crosses. F) Allan Hills d_{excess}.

conditions is limited, the diffusion model is poorly constrained; nonetheless, we solve for diffusion of the synthetic core signal to explore the effects of each of control and to identify potentially relevant processes that could lead to the water-isotope values observed in ALHIC1901.

Layer thickness assignments

Relative layer thicknesses control the depth-weighted smoothing of an ice-core record and are determined by accumulation differences during snow deposition and subsequent thinning. Yan et al. (2021) inferred an interglacial accumulation increase in the Allan Hills up to an order of magnitude from the difference between gas and ice ages in S27 during the penultimate deglaciation, although dating limitations lead to large uncertainty on this estimate. Relative ice-core layer thicknesses observed from the same core define our synthetic core layer thicknesses as described in Equation 4.9. We test a range of relative layer thickness ratios (from approximate glacial-interglacial layer differences of $\lambda_{interglacial} \approx 3.5 \times \lambda_{glacial}$ to $\lambda_{interglacial} \approx 26 \times \lambda_{glacial}$), and consider both the diffusion of the synthetic history across these layers and the smoothing caused by 1-cm sample averaging for the synthetic core. Diffusion controls and experimental results for this test of relative layer thicknesses are provided in Figure 4.5. Figure 4.5d-f shows the experimental controls, including the thinning history, diffusion length for the spatially and temporally constant -35°C experiment, and the age-depth profiles resulting from a range of relative layer thicknes assignments. Figure 4.5a-c and g show the smoothed isotopic data resulting from the described diffusion and 1-cm averaging tests.

Effects of layer thinning

While the final layer thicknesses of ALHIC1901 can be inferred from the refined age scale, the history of layer thinning since deposition is not known in the Allan Hills. If accumulation rates up to 0.0075 m a^{-1} have persisted in time, thinning on the order of 10^4-10^5 would be necessary to achieve the exceptionally thinned layers observed in ALHIC1901. However, because σ_{ice} is a function of thinning, the thinning history has large influence on

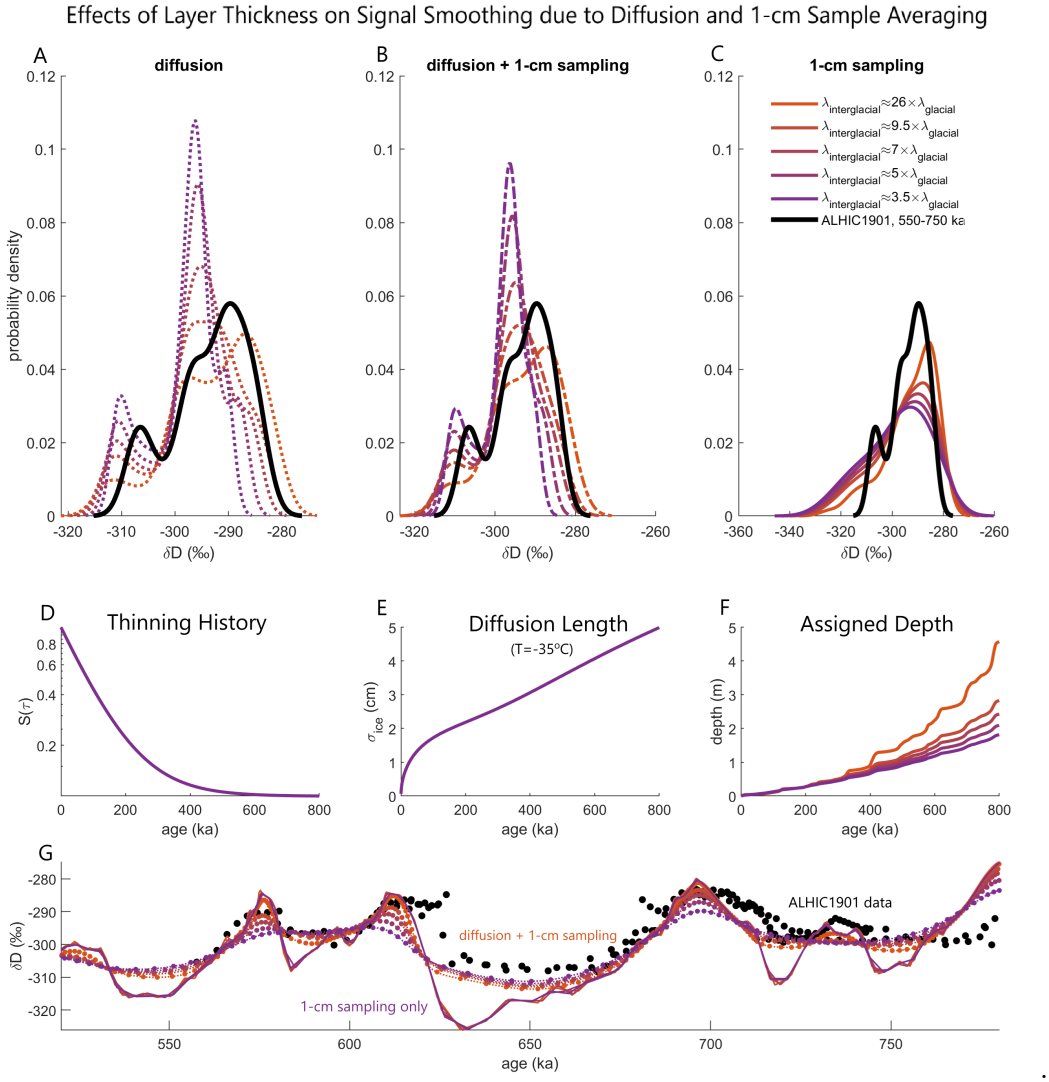

Figure 4.5: Effects of relative layer thickness on signal smoothing. A) Distribution of diffused δD from a synthetic core diffusion experiment with all conditions held constant except the relative layer thicknesses. B) Same as A, but the data have been binned and averaged at 1-cm intervals. C) Distribution of smoothed δD from a synthetic core without diffusion, where all smoothing is due to 1-cm sample averaging. D) Prescribed ice thinning history over time. E) Diffusion length over time for constant -35° temperature forcing. F) Depth-age relationship resulting from the prescribed layer thicknesses. G) Observations from 135-142 m in ALHIC1901 for δD (black) compared with the smoothed synthetic core results over time. Solid lines are smoothed by 1-cm averaging only; dotted lines are smoothed by diffusion only; and colored dots represent 1-cm averaging of the diffused synthetic core signal.

the molecular diffusion. In Figure 4.6, we test three different thinning histories that reduce the synthetic 800-ka column to 2.5 m, which approximates the observed layer thicknesses. These extreme thinning histories exhibit a dominant control on σ_{ice} over these timescales; rapid thinning following deposition will allow more diffusion to take place (i.e., increase σ_{ice}), and slower thinning later in time will reduce the effects of diffusive smoothing (i.e., decrease σ_{ice}). This is observed by the nonlinearities in the relationship between σ_{ice} and age in Figure 4.6e. Figure 4.6 shows the results of the diffused and 1-cm averaged synthetic core experiments with varying diffusion histories.

Effects of temperature

Because diffusivity is temperature-dependent, the ice temperature is another control on σ_{ice} and controls the amount of diffusion between layers of an ice core. Borehole thermometry at ALHIC1901 indicates a basal temperature of about -30°C (Manos et al., in preparation). Assuming a uniform column temperature, we tested a range of temperatures to examine the consequent smoothing. Results for an experiment with gradual thinning and constant layer thickness ($\lambda_{interglacial} \approx 7 \times \lambda_{glacial}$) are provided in Figure 4.7.

Combined diffusive effects

While each of these controls demonstrably smooths the water-isotope record in the direction of the observations, it is difficult to quantify the contributions of any individual process due to the fundamentally unconstrained histories of this ice. However, the histograms provided in Figures 4.6, 4.5, and 4.7 consistently show that 1-cm sample averaging of the synthetic profile is insufficient for reproducing the distribution of observed values between 550-750 ka (i.e., the best-dated and most complete interval) and that smoothing due to diffusion consistently produces a signal with the variability and bimodal distribution of our ALHIC1901 observations. Additionally, because the size of each peak in the distribution is controlled by the glacial-interglacial layer thickness ratio, our results provide new constraints on the relative layer thicknesses, with a best-matched ratio of about $\lambda_{interglacial} \approx 7 \times \lambda_{glacial}$ for the 550-750 ka ice. The general shape of the PDF is preserved by all thinning and tem-

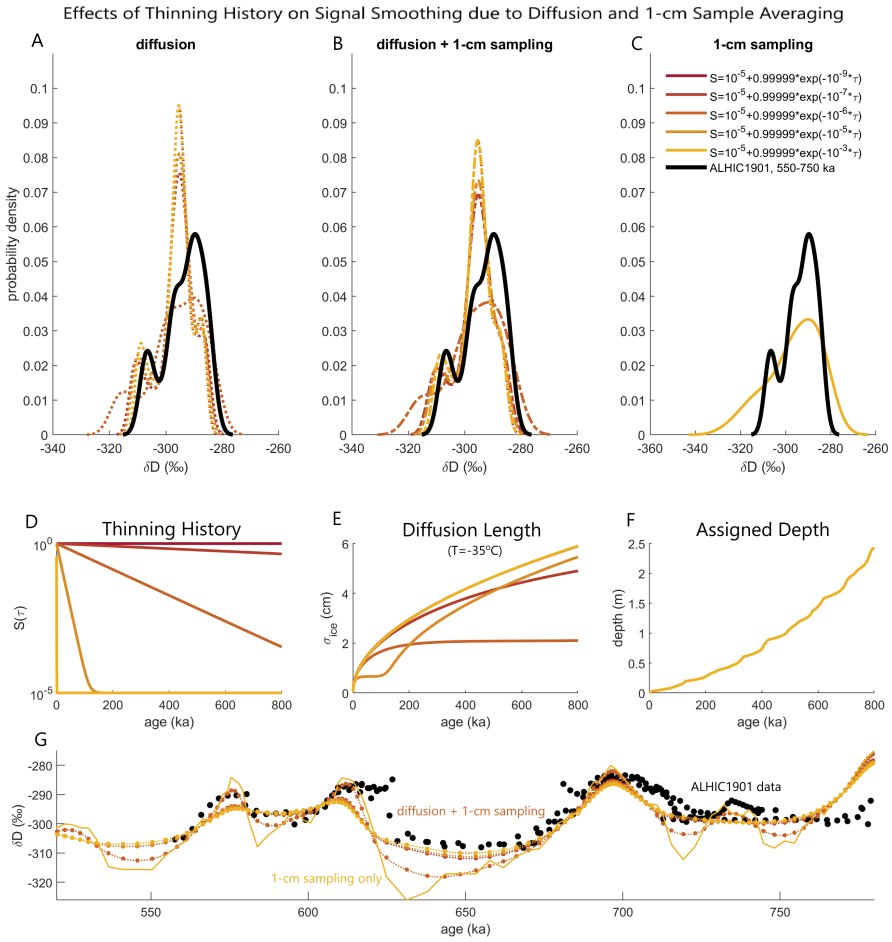

Figure 4.6: Effects of layer thinning history on signal smoothing. A) Distribution of diffused δD from a synthetic core diffusion experiment with all conditions held constant except the layer thinning history. B) Same as A, but the data have been binned and averaged at 1-cm intervals. C) Distribution of smoothed δD from a synthetic core without diffusion, where all smoothing is due to 1-cm sample averaging. Note that because the thinning history affects only diffusion (not smoothing due to sample averaging), all layer thinning history scenarios overlap. D) Prescribed ice thinning histories over time. Equations for each history are provided in the figure legend. E) Diffusion length over time for constant -35° temperature forcing. F) Depth-age relationship resulting from the prescribed final layer thicknesses. G) Observations from 135-142 m in ALHIC1901 for δD (black) compared with the smoothed synthetic core results over time. Solid lines are smoothed by 1-cm averaging only; dotted lines are smoothed by diffusion only; and colored dots represent 1-cm averaging of the diffused synthetic core signal.

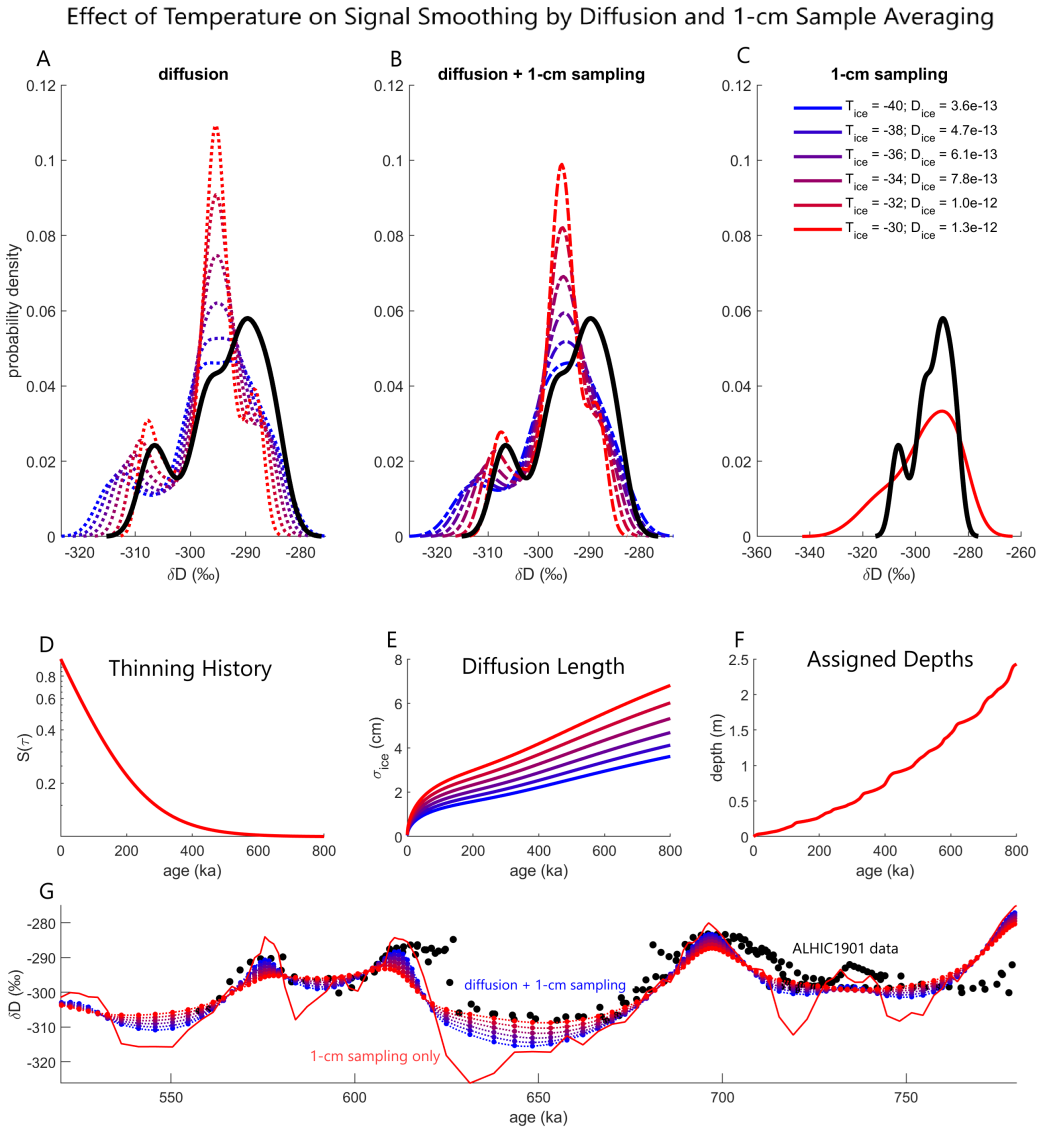

Figure 4.7: Effects of temperature on signal smoothing for a simplified time-invariant temperature experiment. A) Distribution of diffused δD from a synthetic core diffusion experiment with all conditions held constant except the ice temperature. B) Same as A, but the data have been binned and averaged at 1-cm intervals. C) Distribution of smoothed δD from a synthetic core without diffusion, where all smoothing is due to 1-cm sample averaging. Note that because the thinning history affects only diffusion (not smoothing due to sample averaging), all layer thinning history scenarios overlap. D) Prescribed ice thinning history over time. E) Diffusion length over time for temperature forcings ranging from -40°C to -30°C. F) Depth-age relationship resulting from the prescribed final layer thicknesses. G) Observations from 135-142 m in ALHIC1901 for δD (black) compared with the smoothed synthetic core results over time. Solid lines are smoothed by 1-cm averaging only; dotted lines are smoothed by diffusion only; and colored dots represent 1-cm averaging of the diffused synthetic core signal.

perature experiments for both diffusion scenarios, suggesting that the observed smoothing is a consequence of diffusive history and not simply a limitation of our sampling resolution. In addition, no synthetic information is lost when the diffused history is binned and averaged at 1-cm intervals, suggesting that our current sampling resolution is likely sufficient for capturing the full range of preserved variability in this ice.

Effects of diffusion throughout ALHIC1901

Our comparison suggests both extreme thinning and molecular diffusion are necessary to damp the signal as much as is reflected by the ALHIC1901 observations, but specific controls on that process cannot be determined from this analysis alone. We do not interpret these data as evidence of any specific history, but choose one possible history of the 550-750 ka ice to examine the effects of diffusion over longer timescales and in thinner layers.

Figure 4.8a-b show layer thicknesses inferred from ALHIC1901 alongside layer thicknesses for the synthetic core diffusion experiments; here, the relative layer thicknesses assigned by Equation 4.9 use x=0.7 ($\lambda_{interglacial} \approx 7 \times \lambda_{glacial}$) and thinning to match layer thicknesses observed in ALHIC1901. Glacial-interglacial changes for the 550-750 ka interval highlight general agreement with the synthetic history, co-validating both our refined age scale and also the layer thickness estimates for the synthetic core. Glacial-interglacial changes in layer thickness are not apparent at other depths in the core, likely due to dating imprecision and limited observations.

For this test, we consider whether diffusion conditions that produce the observed smoothing in 550-750 ka ice can also produce the observed smoothing in 1-4 Ma ice. Figure 4.8c-d shows the combined diffusive effects for a scenario that produces reasonable smoothing effects for the 550-750 ka ice. We apply the same conditions to the full record for two layer thickness scenarios that match the observed λ for the two sampling intervals (i.e., the younger ice at 135-142 m, and the older ice at 155-160 m). Most core sections exhibit signal damping that is well approximated by the closest end-member diffusion result, with notable exceptions in the 135-138 m interval, where variability is lower than expected, and the 157-158 m interval,

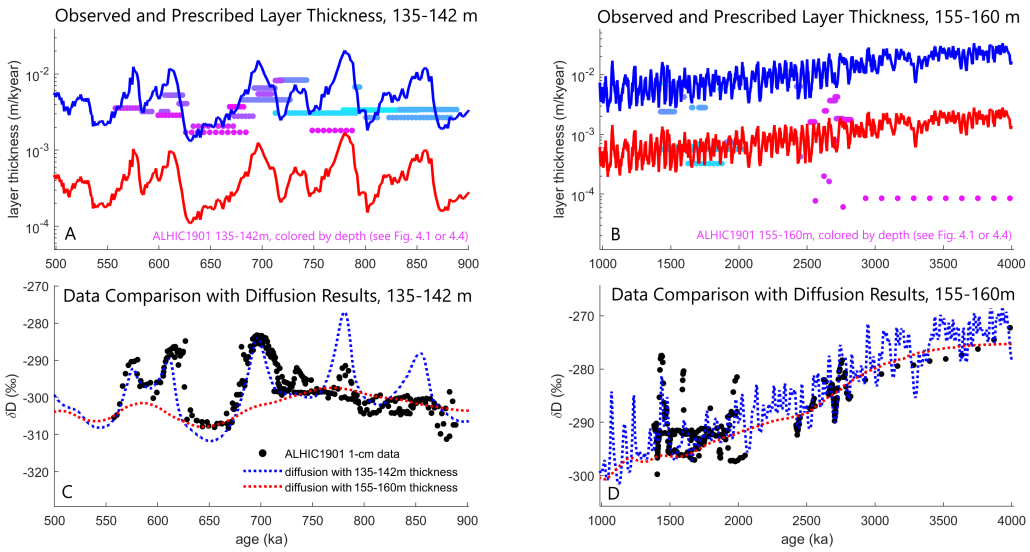

Figure 4.8: Comparison of ALHIC1901 δD data with synthetic core. A-B) Observed layer thicknesses for ALHIC1901 (colored dots – see Figures 4.1 or 4.4 for colorscale by depth). Simulated layer thicknesses that approximate thicknesses observed in the 135-142 m ice (blue line) and the 155-160 m ice (red line). C-D) Comparison of Allan Hills δD data (colored dots) with the diffused synthetic core profile. The blue and red dashed lines indicate diffused signal for these two layer thickness scenarios. Diffusion conditions were chosen to best approximate the 550-750 ka ice and include T=-35°C, $\lambda_{interglacial} \approx 7 \times \lambda_{glacial}$, and gradual thinning of about 10^{-3} since deposition.

where variability is higher. Our results suggest that additional detail could be recovered from ice at 157-158 m (specifically sections ALHIC1901_230-4 and ALHIC1901_231-3), but that other sections are unlikely to contain higher-frequency water-isotope information because the likely effects of diffusion exceed the current sample resolution.

4.5 Discussion

4.5.1 Implications for accumulation and layer thinning of Allan Hills ice

Figure 4.8 demonstrates good agreement between relative layer thicknesses in ALHIC1901 and the synthetic core, which suggests that significant glacial-interglacial changes in accumulation rate persists through at least MIS 15-18 in the Allan Hills, and could be characteristic of this region on longer timescales. Published ice-flow models applied to this region have used relatively invariant accumulation inputs (i.e., Kehrl et al., 2018), but steep interglacial accumulation increases implied by ALHIC1901 and S27 (Yan et al., 2021) over multiple glacial transitions demonstrate a need for variable accumulation conditions in ice-flow models.

While it seems likely that the observed layer thickness gradient is a consequence of accumulation differences, preferential thinning of glacial layers is also possible, if perhaps inconsistent with the interglacial biasing of atmospheric gases reported by Peterson et al. (2024). A three-to-five order-of-magnitude difference in the layer thicknesses observed between S27 and ALHIC1901 implies substantial thinning (up to 99.999%) has occurred within ALHIC1901 layers since deposition, which is both unexplained by existing ice-flow models and difficult to reconcile with meter-scale coherence of geochemical observations across tens of meters (see Chapter 3). We speculate that regional extension of ice combined with complex internal deformation to accommodate shear could lead to the conditions observed in the vicinity of ALHIC1901.

Our layer thickness estimates of ice older than 750 ka are somewhat uncertain due to low isotopic variability and limited dating constraints. Nevertheless, increased isotopic variability over some intervals (e.g., 1.3-1.9 Ma and 2.8 Ma) coincides with increased layer

thicknesses inferred from available dating constraints (Shackleton et al., submitted); high-resolution measurements of other Allan Hills cores, such as by continuous-flow analysis for water isotopes (such as Jones et al., 2017; Gkinis et al., 2011; Davidge et al., 2022), will be useful for identifying sections with best-preserved variability.

4.5.2 Global and local climate influence in the Allan Hills

Present-day snowfall in the Allan Hills is primarily delivered by synoptic events driven by the Amundsen Sea Low and westerly winds (Cohen et al., 2013; Bertler et al., 2004). Yan et al. (2021) interpreted abrupt accumulation changes in S27 during the penultimate deglaciation as evidence of large-scale atmospheric reorganization, and Carter et al. (2024) interprets a large increase in d_{excess} at the same time to a collapsed West Antarctic Ice Sheet (WAIS) and change in moisture source. While both are plausible, long-term coherence between the synthetic core history, which is based on the EDC water-isotope record, and all Allan Hills observations points to a longer-term process connecting archived Allan Hills water isotopes to East Antarctic climate over longer timescales.

We demonstrate that a statistically equivalent relationship between time and $\Delta\delta$ from EDC is observed in all available Allan Hills data since about 725 ka, before which time the age-dependent relationship is no longer supported by the data. This age-dependent slope implies a local change in δ^{18}O of 4.4‰ since about 725 ka, although the cause of this shift is not immediately clear.

A simple explanation for the change in δD and δ^{18}O is an increase in distillation, such as would be caused by an increase in elevation or a change in sea-ice extent; however, neither mechanism is insufficient to cause the relationship observed between δD and δ^{18}O. Using a lapse rate of 1K/100m and isotope-temperature relationship of 0.88‰ δ^{18}O/K (Buizert et al., 2021) from the nearby Talos Dome ice core site, we find that the magnitude of temperature change is about 5°C, explainable by local ice sheet growth of 510±50 m since 725 ka. However, this cannot account for the synchronous decrease in d_{excess}; increased elevation and a cooler deposition site would extend the atmospheric distillation pathway and

cause additional fractionation, thus leading to higher (not lower) values of d_{excess}. Sea ice is often considered a local influence on d_{excess} in coastal Antarctic sites, both because sea-ice extent controls local moisture flux through increased evaporation from the open water (e.g., Weatherly, 2004; Posmentier et al., 2011) and because moisture recycling from the re-evaporation of isotopically deplete sea ice is known to alter the isotopic composition of the atmosphere (e.g., Bonne et al., 2019). While a long-term change in sea-ice extent could also increase the distillation of marine air masses arriving in the Allan Hills, this mechanism is also insufficient in that it cannot explain the decrease in d_{excess} since 725 ka.

Observations of low d_{excess} are common in the Allan Hills and nearby McMurdo Dry Valleys (e.g., Dadic et al., 2015; Gooseff et al., 2006; Hu et al., 2022, Carter et al., 2024). Low d_{excess} is common in coastal sites due to the warmer conditions, reduced distillation (relative inland sites), and ice cloud dynamics (e.g., Dutsch et al., 2019). However, Hu et al. (2022) found that an isotope-enabled atmosphere model, iCESM (Nusbaumer et al., 2017; Brady et al., 2019) was unable to reproduce the observed Allan Hills d_{excess} surface values with a moisture-tagging experiment, and interpreted the unusually low values as evidence of post-depositional sublimation in the Allan Hills. Post-depositional sublimation in blue-ice settings is likely on some scale due to the exceptionally windy conditions near the Antarctic coast. Katabatic winds move dense air masses from the Antarctic plateau at high speeds (>30 m s^{-1}, Nylen et al., 2004), allowing isotopic exchange in surface layers and driving ablation of surface ice in the Allan Hills BIA. However, a theoretical increase in local sublimation due to surface exchange with katabatic winds would decrease d_{excess} and increase $\delta^{18}O$, which is not consistent with the age-$\Delta\delta$ relationship in ALHIC1901 and therefore also unlikely.

Existing ideas of the controls on Allan Hills water isotopes assume that samples from surface snow and ice originated as local precipitation. However, in a local climate characterized by – and perhaps controlled by (Parish and Cassano, 2003; Nylen et al., 2004) – high winds and surface scour, the roles of vapor exchange and snow redistribution are not well understood. Katabatic controls over water-isotope composition at other coastal sites has been observed over shorter timescales: in coastal Greenland, daily fluctuations in the at-

mospheric water-isotope composition are driven by a reversal between continentally-sourced air masses (with low δ^{18}O and high d_{excess}) at night and marine-sourced air (with high δ^{18}O and low d_{excess}) delivered by sea breeze events as land temperatures increase (Kopec et al., 2014). At another coastal Antarctic site, fluctuations in the intensity of continental katabatic winds were shown to cause a similar reversal in coastal isotope values (Breant et al., 2019). However, these mechanisms still cannot explain the simultaneous decreases in both δ^{18}O and d_{excess} over long timescales.

In order to explain long-term trends in δ^{18}O, δD, and d_{excess}, a mechanism is needed that simultaneously decreases all isotope values, which is not the typical relationship resulting from either distillation or evaporation. While the mechanisms described above are insufficient in isolation to explain the changes observed in Allan Hills water isotopes since about 725 ka, it is plausible that in combination, they could lead to the trend observed in our samples. We propose that changes in the delivery of continental air masses to the Allan Hills could cause the trend observed in water-isotope data since the MPT. Specifically, a combination of wind scour from the high-plateau and sublimation of blowing snow can lead to simultaneous decreases in δ^{18}O – as either more redistributed snow is incorporated or as the elevation site of the scoured snow increases – and in d_{excess}, due to sublimation. This would imply an onset of either stronger wind controls coincident with the MPT, increased ice-sheet elevation at upstream scour sites, or both. While there is considerable need for additional studies of snowfall, accumulation, and archival processes in the Allan Hills, a preliminary analysis of local isotopic controls in snow supports the possibility of continental wind controls on isotopic composition – more details about these preliminary observations are available in Appendix C. The significant control exhibited by katabatic winds on water isotopes in other regions and the perplexing relationship between water isotope data in the Allan Hills – perhaps best explained as a response to those winds – highlights the need for a more thorough investigation of wind redistribution and controls on the archival processes in this region.

4.6 Summary

We detected high-frequency water-isotope variability in 1-cm samples from 0-25 m above the bed in stratigraphically disturbed Allan Hills core ALHIC1901. We used the preserved water-isotope patterning within each section to refine an age-scale interpolation that agrees within error with the ^{40}Ar-age scale developed by Shackleton et al. (submitted), and compared our measurements with the Dome C ice-core record (Landais et al., 2021) and globally stacked benthic δ^{18}O data (Lisiecki and Raymo, 2005). We used observed layer thicknesses within the core to constrain a diffusion experiment using a synthetic ice-core record developed by modifying EDC and LR04 records, and found that diffusion can recreate the observed variability and distribution of water-isotope data in 550-750 ka ice. We show that higher-resolution sampling is unlikely to recover additional detail. We identify a few sections of ice with superior signal preservation as targets for other analyses. Our data suggest that the Allan Hills have experienced approximately seven-fold changes in accumulation rate during glacial periods since at least 725 ka, and we suggest that our samples have been thinned by an additional 3-4 orders of magnitude. To explain decreasing trends in all water isotopes since about 725 ka, we propose that Allan Hills ice could be significantly influenced by plateau-sourced snow that is redistributed by katabatic wind events.

Chapter 5

THE WATER-ISOTOPE SYSTEM IN A WARMER WORLD: SENSITIVITIES TO GLOBAL CLIMATE IN MIOCENE ICE

5.1 Overview

Ice-core samples from the Allan Hills have been dated to 6 Ma; basal ice that cannot be dated by ^{40}Ar due to low gas content is likely even older. While these samples extend the ice-core water-isotope record through the Pliocene (2.6 - 5.3 Ma) and into the late Miocene (5.3 - 23 Ma), interpreting the water-isotope data as a temperature record is complicated by uncertainty in the temperature-isotope relationship on these timescales. Changes to Earth's mean climate state on multimillion-year timescales would theoretically alter the water isotope system – with changes to the temperature-isotope relationship imparted by global changes to atmospheric moisture gradients, ocean surface conditions, and isotopic composition of source waters – but the magnitude and direction of these changes for the temperature-isotope relationship of polar snow is not well characterized. This chapter offers an initial investigation of the isotope response to Miocene-like atmospheric and oceanic changes at the atmosphere-ocean boundary layer with a simple Rayleigh fractionation model. I show that expected changes in Earth's climatology shift polar isotopes in the direction of Allan Hills observations, suggesting at least part of the observed isotope response is due to changes in the global water isotope system and not local temperature. Higher-resolution atmospheric models that more accurately reflect global moisture gradients could better resolve changes to this relationship over time.

5.2 Introduction

Marine sediment records suggest a long-term cooling of Earth's global climate from the Miocene (23 - 5.3 Ma) and through the Pliocene (5.3 - 2.7 Ma), with variability in Earth's climate state caused by ice-sheet and oceanic changes (Clark et al., 2024). Oxygen isotope records from benthic foraminifera have been critical for studying the growth cycles and histories of modern ice sheets, but because benthic δ^{18}O reflects both local ocean temperature and ice-sheet volume, disentangling these histories is complex (Langebroek et al., 2010). Climate records developed from Antarctic ice-core samples could provide more direct evidence

of Antarctic climatic changes during this time period. Shackleton et al. (submitted) identified ice as old as 6 million years – and likely older – in basal material at Allan Hills core site ALHIC1902, and developed a temporally discontinuous record of stable water isotopes (δ^{18}O, δD, and d_{excess}) from absolutely dated, chronologically disordered ice-core samples.

While the Allan Hills glaciological setting adds complexity to the interpretation of these ice-core data, this new archive opens the possibility of interpreting ice-core water-isotope records up to at least 6 Ma (Shackleton et al., submitted). Uncertainty in the glacial provenance of Allan Hills ice and uncertainty in the age of basal materials add difficulty to interpreting changes in isotope values. Within the bottom tens of centimeters of the ≥6-Ma ALHIC1902 core, δ^{18}O and d_{excess} both increase by approximately 5‰ (Shackleton et al., submitted; see Figure 5.1), potentially indicating large transitions in climate, local glaciological setting, or both during the associated time interval. Shackleton et al. (submitted) speculate that the large increase in isotopic composition near the bed could be evidence of a distinct volume of middle-to-late Miocene snowpack that was buried by the encroachment of the growing East Antarctic Ice Sheet into this region during that time (Shackleton et al., submitted; Denton and Sudgen, 2005), and they approximate a temperature history for the Allan Hills since 6 Ma using the modern relationship between water-isotope observations and temperature (Masson-Delmotte et al., 2008). However, this method of temperature conversion does not account for changes in the temperature-isotope relationship over time, and is therefore highly uncertain (Shackleton et al., submitted; Jouzel et al., 2003). While the modern spatial slope (0.80‰/K) is similar to the isotope-temperature relationship from the nearby Talos Dome ice core (0.88‰/K; Buizert et al., 2021) – which extends in time beyond 300 ka (Crotti et al., 2021) – the stability of the temperature-isotope relationship deeper in time is not known.

Differences in Earth's mean climate state, such as the long-term cooling observed before 800 ka and its effects on ice-sheet configuration and sea level, are associated with changes in Earth's atmosphere and oceans that theoretically affect the water-isotope system, including the temperature-isotope relationship (Boyle, 1997; Fricke and O'Neil, 1999; Botsyun et al.,

2023). Pliocene and Miocene climate was warmer and more humid than present day, with smaller ice sheets, warmer oceans, and a reduced sea-surface temperature (SST) gradient (Fedorov et al., 2015; Zhang et al., 2014; Burls et al., 2021). These notable changes to Earth's climate would alter the distillation conditions experienced by atmospheric moisture, but a framework is needed to explore the effects of a warmer world on the water isotope system.

Recent efforts to model Miocene and Pliocene climate have advanced theoretical understandings of the relationships between Antarctic ice sheet configuration, ocean temperature, and sea level changes, but implications for the water-isotope system are not well established. Simulations of Miocene climate have been combined and compared through the MioMIP1 ensemble (Burls et al., 2021), although MioMIP1 ensemble members vary in both model configurations and experimental design and vary widely in terms of atmospheric moisture expectations (Acosta et al., 2023). Other modeling efforts have explored the water-isotope system under different climate states with the goal of interpreting terrestrial (Botsyun et al., 2022) or marine (Langebroek et al., 2010) water-isotope archives. Langebroek et al. (2010) modeled the effects of ice-sheet volume on δ^{18}O of seawater, and Botsyun et al. (2023) used an isotope-enabled model to examine specific changes to the δ^{18}O of precipitation over Europe using middle-Miocene boundary conditions; both suggest that Miocene-like boundary conditions could change the interpretation of water isotopes on these timescales.

Interpreting observed changes to basal water-isotope values in ALHIC1902 will be facilitated by a better understanding of these global temperature controls on the water-isotope system. Basal ice from ALHIC1902 contains anomalously low gas concentrations, thereby preventing absolute age determination (Shackleton et al., submitted) and limiting the number of geochemical records that can be developed from samples of basal material. Despite this, existing N_2 and O_2 data indicate the likelihood of refreezing after a thaw event and alteration near the bed (Shackleton et al., submitted); despite the potential for melt and refreezing processes to impact the water-isotope record, the basal samples from ALHIC1902 are not depleted in d_{excess} relative to the meteoric water line. In fact, they are enriched in

d_{excess} relative to the local meteoric water line observed in other Pliocene and late Miocene samples from the Allan Hills (Figure 5.1), further highlighting the demand for additional information about global temperature forcings on the distillation of polar water isotopes on these timescales.

In this chapter, I verify the steep isotope increase in basal ice from ALHIC1902 by re-measuring the ice with 1-cm resolution, and then I explore the response of water isotopes to hydrologic cycle changes that are expected on multimillion-year timescales. I use a simple water isotope fractionation model (SWIM; Markle and Steig, 2021) to quantify the strength and direction of water-isotope changes in polar precipitation due to prescribed differences in the global hydrologic cycle relative to modern conditions. I demonstrate that climate conditions resulting from a warmer global temperature can cause an unambiguous shift in polar water-isotope values that are especially pronounced for d_{excess}. This work builds intuition for interpreting water isotopes from polar precipitation during warmer climatic intervals in Earth's past.

5.3 Confirmation of water-isotope relationship in basal ice

While steep changes to the isotopic gradient were observed by Shackleton et al. (submitted) in basal materials, only one measurement is available of isotopically distinct basal materials. First, I confirm this result with higher-resolution measurements from the bottom meter of ALHIC1902 ice. Approximately 50 cm of basal ice from <1m above bedrock at site ALHIC1902 were sampled at 1-cm vertical resolution to confirm basal water-isotope values and to investigate the nature of isotopic changes near the bed. Four samples from ALHIC1902 (including ALHIC1902_321-1, ALHIC1902_322-2, ALHIC1902_322-3 and ALHIC1902_324-1) were cut by bandsaw into approximately 1-cm cubes and were melted in polyethylene bottles inside a 4°C refrigerator. Approximately 200 μL of meltwater were aliquoted into glass vials with conical inserts and clean caps with a septum; bottles were measured alongside four internal reference waters by an autosampler with a Picarro L2130-i in agreement with Schauer et al. (2016). Calibrated data are shown alongside measurements from Shackleton

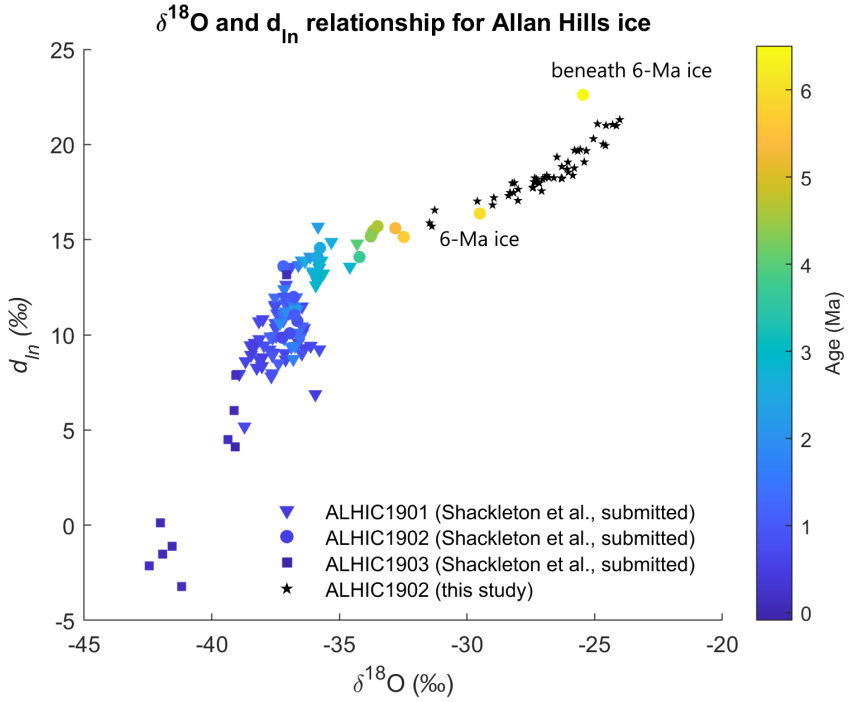

Figure 5.1: Water-isotope data for dated samples of ALHIC1901, ALHIC1902, and ALHIC1903 between 0 and 6+ Ma (colored triangles (ALHIC1901), circles (ALHIC1902), and squares (ALHIC1903); Shackleton et al., submitted) and water-isotope data for 1-cm vertically resolved subsamples of ALHIC1902 basal material (black stars). The oldest dated sample is 6±0.6 Ma, and is labeled as "6-Ma ice" (ALHIC1902, mid-sample depth 205.65 m). The basal sample is not dated and is labeled as "beneath 6-Ma ice" (ALHIC1902, mid-sample depth 206.45). 1-cm samples for this study span a (discontinuous) vertical range of 205.61 to 206.67 m.

Reference Water	δD (‰)	δ^{18}O (‰)	d_{excess}(‰)
BW	-156.87	-20.01	3.21
SW	-75.63	-10.55	8.77
WGW	-318.82	-39.77	-0.66
WW	-268.3	-33.82	2.26

Table 5.1: Table of internal reference waters used to calibrate measurements of ALHIC1902 basal ice. BW is a mixture of Antarctic water from ITASE and Seattle tapwater; SW is seattle tapwater; WGW is glacial meltwater from the WDC06A core in West Antarctica, and WW is meltwater from the WDC06A core in West Antarctica. Data in this section were calibrated to BW, SW, and WGW, and WW is used as a verification of the calibration.

et al. (submitted) in Figure 5.1; these data confirm a change in the δ^{18}O-d_{excess} relationship within the bottom 40 cm of ice.

5.4 Modeling atmospheric distillation pathways

Numerical modeling of water-isotope distillation permits the quantitative interpretation of water-isotope data as corresponding site and source temperatures. In this section, I simulate the fractionation of water isotopes along a wide range of atmospheric distillation pathways, and I specifically explore the model's sensitivity to changes at the ocean-atmosphere boundary that would be likely in a warmer climate state to quantify changes in precipitation-site isotope values that result from otherwise identical distillation trajectories. This approach quantifies the difference in isotope composition that could result entirely from ocean-surface changes during a warmer climate state (i.e., not due to the precipitation-site climate), which is important context for interpreting changes in ice-core isotope values over multimillion-year timescales.

The observed increase near the bed of the ALHIC1902 δ^{18}O-d_{excess} slope is perhaps indicative of increased distillation, which could be caused by an increased temperature gradient between evaporation and precipitation sites (such as in the case of increased ice elevation or

decreased ice temperature) or by fundamental changes to the conditions governing fractionation along that gradient (as noted by Boyle (1997), Fricke and O'Neil (1999), or Botsyun et al. (2023)). Disentangling influences from ice-sheet evolution, local temperature, and mean climate state on these timescales is difficult because of large uncertainties in all three. As an initial step towards building a theoretical understanding of isotopic changes in Antarctic precipitation that are driven by changes to Earth's mean climate state over multimillion-year timescales, I use a simple Rayleigh fractionation model to isolate the isotopic response in precipitation of changes during evaporation.

The isotope-to-temperature conversion of Miocene precipitation is a somewhat circular problem, as fractionation models rely upon many assumptions about the climate state that the isotopes could provide insight into. Markle and Steig (2021) built a simple water-isotope distillation model that defines a domain of pseudo-adiabatic temperature gradients and models distillation along those pathways to determine the resulting composition of δ^{18}O and d_{ln}[1]. The model relies upon modern climatological correlations to define thermodynamic conditions along the atmospheric temperature gradient (Markle and Steig, 2021). For example, reliance on modern statistical associations between air temperature and sea-surface temperature permits the straightforward assignment of realistic sea-surface temperatures to a prescribed atmospheric temperature pathway, which enables fairly accurate conversion of modern isotopes to temperature with modern climate conditions (Markle and Steig, 2021). While the applicability of these climatic relationships is less clear for multimillion-year-old precipitation, investigating the sensitivity of the model's isotopic response to climatic changes can provide insight into possible influences on the water-isotope system in other climate states.

Miocene-age changes to Earth's climatology likely impacted the water-isotope system. On shorter timescales, changes between glacial and interglacial climatology are known to alter

[1]Note that in this section, we use the logarithmic definition of deuterium excess due to its incorporation in the Markle and Steig (2021) fractionation model and demonstrated improvements in the quantitative interpretation of d_{ln} relative to d_{excess}.

the temperature-isotope slope (Boyle, 1997), and those effects are likely more pronounced over longer timescales due to long-term changes in and above Earth's oceans (Botsyun et al., 2022; Burls et al., 2021). An increase in global mean temperatures during the Pliocene and Miocene is associated with smaller ice sheets, decreased meridional temperature gradients, and changes to Earth's hydrologic cycle (Burls et al., 2021); these changes cause fundamental differences in oceanic and atmospheric conditions affecting water isotope evaporation and distillation. Increased global temperature is associated with smaller ice sheets and depletion of mean ocean water δ^{18}O relative to modern values; warmer temperatures and differing humidity conditions alter atmospheric distillation pathways.

In Figure 5.2a, I highlight the differences between the MioMIP1 ensemble mean (Burls et al., 2021) and NCEP modern climatology. While the general global relationship between 2-m air temperature – which defines a distillation gradient initial condition – and the sea-surface temperature, which is a control on evaporative fractionation, is similar in NCEP and the MioMIP1 ensemble mean, 5.2d-i show the isotopic differences from results modeled with NCEP. Isotopic anomalies are generally positive for d_{ln} and negative for δ^{18}O (except at the warmest evaporation sites (i.e, > 20°C when the seawater composition is not changed from modern), indicating a shift consistent with the direction of change observed in the Allan Hills basal ice. This effect is exaggerated by depleted seawater values, leading to average changes in δ^{18}O of -1‰ $\delta^{18}O_{site}/\delta^{18}O_{seawater}$ and average changes in d_{ln} >4‰ $d_{ln-site}/\delta^{18}O_{seawater}$. We note that the d_{ln} anomaly increases with decreasing evaporation temperature (T_{source}), thus likely (and perhaps disproportionately) affecting Antarctic precipitation.

A few idealized tests to interrogate the cause of the relationship shown in Figure 5.2 are shown in Figures 5.3 and 5.4. First, we consider uniform warming of the sea-surface temperature (SST) by 1°C. As shown in 5.3, the magnitude and direction of isotopic change here is similar, but it does not account for the nonlinearity in either the T_{source} effect (which the MioMIP1 run is relatively insensitive to between 10-25°), nor the inversion of the T_{site}-isotope relationship shown in Figure 5.2d. The result is also slightly more sensitive to the seawater composition, leading to average changes in δ^{18}O of -1.3‰ $\delta^{18}O_{site}/\delta^{18}O_{seawater}$

and average changes in d_{ln} >8‰ $d_{ln-site}/\delta^{18}O_{seawater}$. The nonlinearity of the isotope-T_{site} relationship is reproducible by simulating a reduced meridional SST gradient, as shown in Figure 5.4a. The similarity of isotope response for these runs to the MioMIP1 forcing suggests that the nonlinear isotope response could be characteristic of a reduced meridional gradient, although Antarctic precipitation is likely to be influenced by increased d_{ln} and decreased $\delta^{18}O$ due to low evaporation temperatures.

5.5 Conclusions

While the scope of this preliminary work is limited, the Rayleigh fractionation modeling results presented here link sea-surface evaporative changes that are expected in a warmer climate state to notable enrichment of d_{ln} (of several ‰) in polar precipitation and a smaller change in $\delta^{18}O$; these changes are especially pronounced for high-latitude evaporation sites (i.e, at low evaporation temperatures) and for isotopically depleted seawater that is associated with smaller ice sheets and higher sea levels. Our results highlight the sensitivity of water isotopes (especially d_{ln}) to the mean climate state and suggest that at least some of the change to the meteoric water line observed in basal ice from ALHIC1902 could be attributed to these global hydrologic cycle changes. This preliminary work invites additional study of the water-isotope system under Miocene and Pliocene conditions – especially to consider differences in humidity gradients – and cautions against simple interpretations of d_{excess} using modern relationships, as the d_{excess}-temperature relationship has likely evolved with global climate. This work does, however, suggest that the $\delta^{18}O$-temperature relationship is less sensitive.

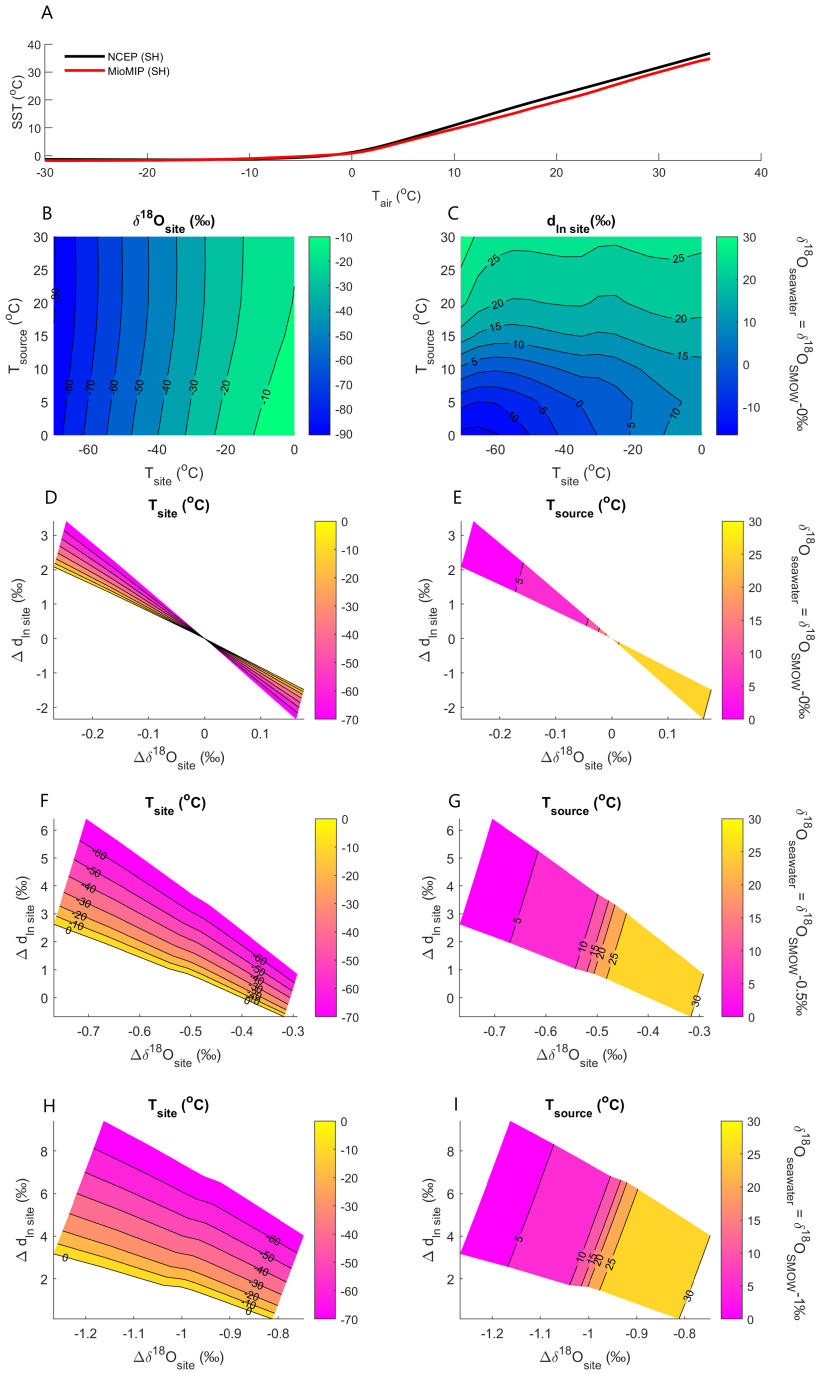

Figure 5.2: Isotope response to MioMIP1 atmosphere relative to modern reanalysis data from NCEP (southern hemisphere (SH) only). A) Relationship between air temperature (at 2 m) and SST. The black line is from SH NCEP (1980-2010); the red line is from the MioMIP1 ensemble mean temperature data Burls et al. (2021). B) Modeled precipitation-site δ^{18}O for MioMIP1 temperature conditions shown in panel A. δ^{18}O data are contoured for the full domain of evaporation (T_{source}) and precipitation (T_{site}) conditions. C) Same as panel B but for d_{ln}. D) Inverted precipitation-site temperature surface shown as a function of modeled precipitation-site δ^{18}O and d_{ln} anomalies; isotope anomalies are the difference between modeled values for the MioMIP1 SSTs and modeled values for the SH NCEP 1980-2010 climate. E) Same as D for evaporation source temperature at 2m. F) Same as D, but the δ^{18}O of seawater has been decreased by 0.5‰ δ^{18}O and 0‰ d_{ln}. G) Same as E, but the δ^{18}O of seawater has been decreased by 0.5‰ δ^{18}O and 0‰ d_{ln}. H) Same as D, but the δ^{18}O of seawater has been decreased by 1‰ δ^{18}O and 0‰ d_{ln}. I) Same as E, but the δ^{18}O of seawater has been decreased by 1‰ δ^{18}O and 0‰ d_{ln}.

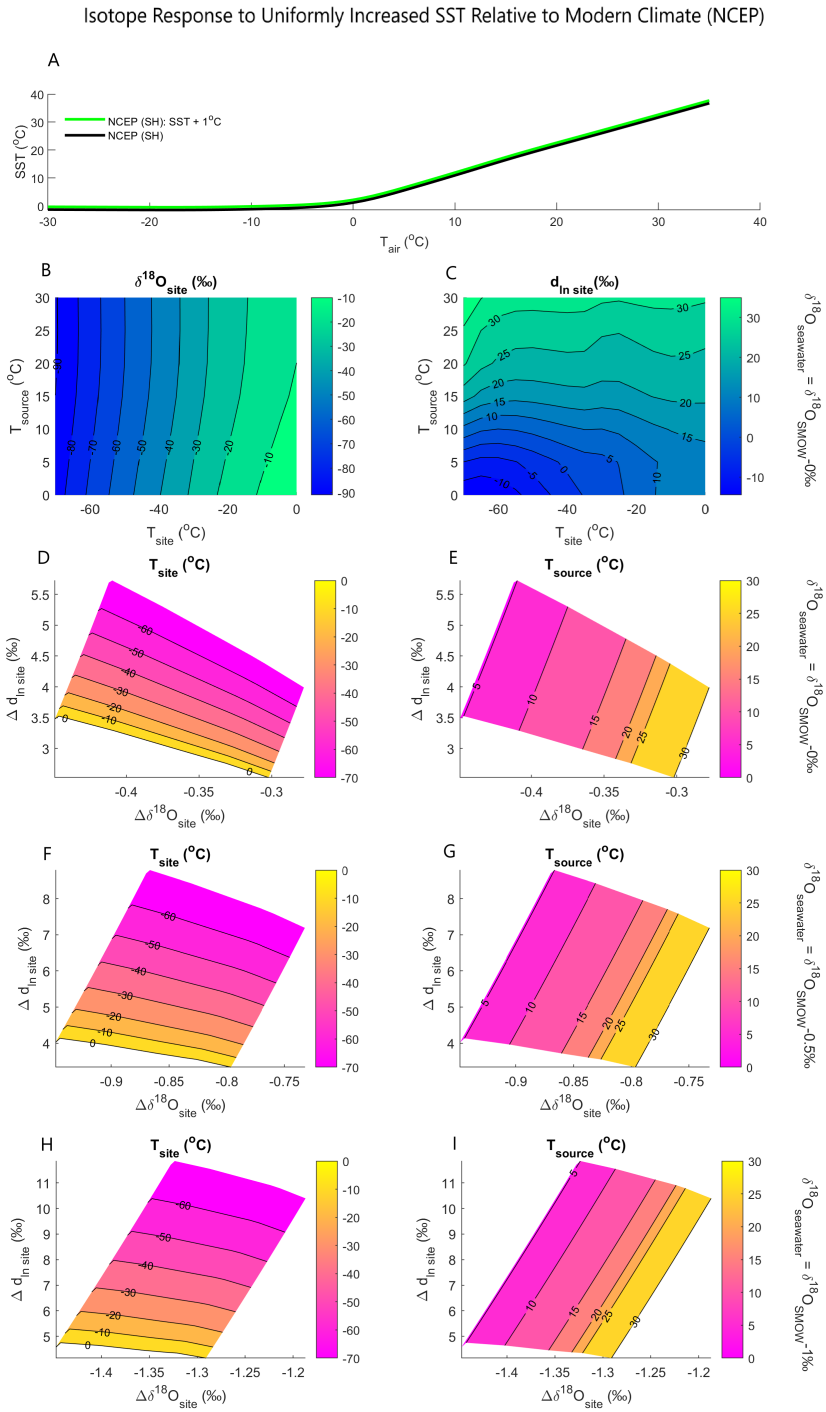

Figure 5.3: Isotope response to uniformly increased sea-surface temperature (SST) relative to modern reanalysis data from NCEP (southern hemisphere (SH) only). A) Relationship between air temperature (at 2 m) and SST from SH NCEP (1980-2010); black line). The green line is the same data, with all SSTs uniformly adjusted by +1°C. B) Modeled precipitation-site δ^{18}O for NCEP distillation conditions with SSTs uniformly increased by +1°C as shown in panel A. δ^{18}O data are contoured for the full domain of evaporation (T_{source}) and precipitation (T_{site}) conditions. C) Same as panel B but for d_{ln}. D) Inverted precipitation-site temperature surface shown as a function of modeled precipitation-site δ^{18}O and d_{ln} anomalies; isotope anomalies are the difference between modeled values for the SST+1°C climate and the modeled values for the unaltered SH NCEP 1980-2010 climate. E) Same as D for evaporation source temperature at 2m. F) Same as D, but the δ^{18}O of seawater has been decreased by 0.5‰ δ^{18}O and 0‰ d_{ln}. G) Same as E, but the δ^{18}O of seawater has been decreased by 0.5‰ δ^{18}O and 0‰ d_{ln}. H) Same as D, but the δ^{18}O of seawater has been decreased by 1‰ δ^{18}O and 0‰ d_{ln}. I) Same as E, but the δ^{18}O of seawater has been decreased by 1‰ δ^{18}O and 0‰ d_{ln}. .

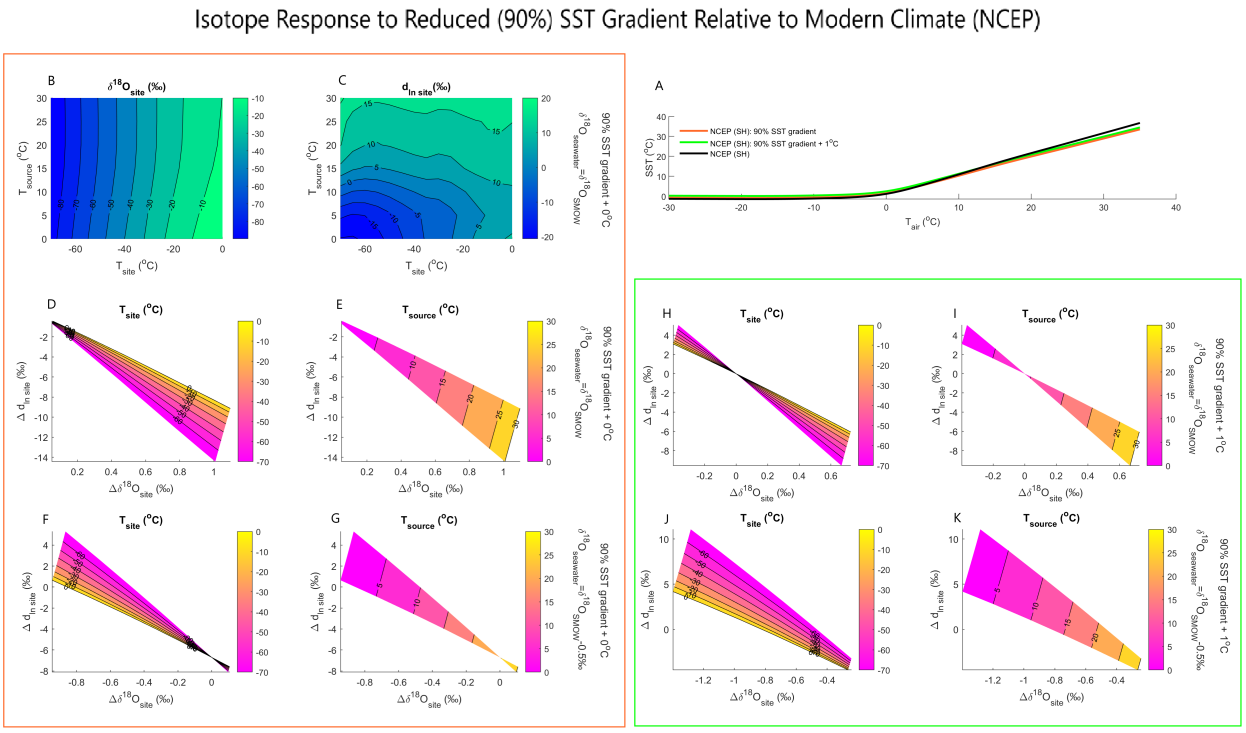

Figure 5.4: Isotope response to a reduced (90%) SST gradient relative to modern reanalysis data from NCEP (southern hemisphere (SH) only). A) Relationship between air temperature (at 2 m) and SST from SH NCEP (1980-2010); black line). The orange line is the same data, with all SSTs multiplied by 90%. The green line is the same data, with all SSTs multiplied by 90% and increased by +1°C. B) Modeled precipitation-site δ^{18}O for NCEP distillation conditions with a reduced (90%) SST gradient as shown in panel A (orange line). δ^{18}O data are contoured for the full domain of evaporation (T_{source}) and precipitation (T_{site}) conditions. C) Same as panel B but for d_{ln}. D) Inverted precipitation-site temperature surface shown as a function of modeled precipitation-site δ^{18}O and d_{ln} anomalies; isotope anomalies are the difference between modeled values for the reduced SST gradient climate and the modeled values for the unaltered SH NCEP 1980-2010 climate. E) Same as D for evaporation source temperature at 2m. F) Same as D, but the δ^{18}O of seawater has been decreased by 0.5‰ δ^{18}O and 0‰ d_{ln}. G) Same as E, but the δ^{18}O of seawater has been decreased by 0.5‰ δ^{18}O and 0‰ d_{ln}. H) Inverted precipitation-site temperature surface shown as a function of modeled precipitation-site δ^{18}O and d_{ln} anomalies; isotope anomalies are the difference between modeled values for the reduced SST gradient climate +1°C and the modeled values for the unaltered SH NCEP 1980-2010 climate. I) Same as H for evaporation source temperature at 2m. J) Same as H, but the δ^{18}O of seawater has been decreased by 0.5‰ δ^{18}O and 0‰ d_{ln}. K) Same as I, but the δ^{18}O of seawater has been decreased by 0.5‰ δ^{18}O and 0‰ d_{ln}.

Chapter 6

SUMMARY

This work explores the water-isotope system as recorded by discontinuous blue-ice cores in the Allan Hills of Antarctica. The Allan Hills BIA is a very unconventional climatological and glaciological setting for paleoclimate reconstructions from ice cores because it is not possible to infer the glaciological history of chronologically discontinuous Allan Hills ice by geophysical methods or computational tools. While these uncertainties are less relevant for atmospheric gas measurements, which are generally thought to be globally averaged, it presents considerable difficulty in interpreting water-isotope data from this region.

In the Allan Hills, strong katabatic winds ablate surface ice, inducing vertical ice flow and shearing and folding of ice strata. Because the water-isotope signal in disturbed ice is affected by both the climate during snow deposition and by subsequent glaciological processes, the resulting climate record is an indication of both processes, and it is possible to infer both climatological and glaciological information from disturbed cores. In this thesis, I present several studies of Allan Hills water isotopes that investigate the integrated history of climate and glaciology from Allan Hills ice.

In Chapter 2, I presented a measurement methodology for high-resolution water-isotope analysis using continuous-flow analysis and laser spectroscopy. I demonstrated that CFA can be used for all stable water isotopes (including $\delta^{17}O$ and $\Delta^{17}O$) with errors that are lower than or comparable to other methods. I investigated the causes of CFA errors and showed that the largest source of error is a calibration offset, which can be prevented by the measurement of additional reference waters. I showed that the CFA data agree with discrete measurements both for an ice-core section from Summit, Greenland (Davidge et al., 2022) and for a 68-m record of centimeter-resolved Allan Hills ice from ALHIC2201 (Hudak et al., 2024). A similar system is now in use at the COLDEX CFA laboratory.

In Chapter 3, I consider what the distribution and patterning of water-isotope data in the Allan Hills implies about ice-flow history and snow sources for geographically distinct cores. I present four new records of Allan Hills drilling chips from sites ALHIC1902 (limited interval), ALHIC2201 (full core), ALHIC2301 (full core), and ALHIC2302 (first drilling season only); while not yet well-dated, these records introduce new geochemical information

about the spatial distribution of isotopically similar ice that can provide insight into regional flow. These data confirm the spatial trend in the isotope values, where downgradient sites like S27 and ALHIC1903 are most negative, and ALHIC2301 (in the "cul-de-sac" region) is the least negative δ; this trend generally agrees with known age constraints and modern ice flow conditions (i.e., the youngest ice is downstream from the fastest-flowing ice, and ice in the cul-de-sac is, on average, the oldest), suggesting that this flow pattern has been established for some time. I show that isotopes at several core sites are statistically similar, suggesting similar spatiotemporal origins for many cores. In particular, four cores along a flowline contain isotopically indistinguishable ice; I show that the isotopic profiles at these sites can be cross-correlated, which suggests extensional flow towards the nunatak, where ablation is most prevalent, with internal deformation of layers distorting the signal between core sites at meter-length scales. I show that the farthest downstream core is missing tens of meters of ice that are measured upstream, likely due to wind scour near the nunatak.

Chapter 3 also considers the reproducibility of the water-isotope signal within an individual ice core.[1] We show that data are highly correlated on two different sides of a 24-cm ice core, but that steeply dipping layers and asymmetrical thinning cause large vertical isochronal offsets (up to 20 cm). Scaling factors and vertical offsets are comparable to the large-scale average layer scaling and dip, which is suggestive of local bedrock controls on ice distortion at all scales.

In Chapter 4, I show that high-frequency information recorded by ALHIC1901 can be approximated by rapid ice thinning and diffusion of a statistically determined synthetic climate history. My data demonstrate that observed isotopic δ and d_{excess} fluctuations can be aligned within the ^{40}Ar-age scale error to expected global climatic fluctuations. While thinning, temperature, and accumulation histories that govern the diffusion process are relatively unconstrained, I demonstrate that thinning on the order of 10^3-10^5 and diffusion are likely in disturbed Allan Hills ice and that the thinning history is a dominant control on the

[1]This is work that was conducted collaboratively with former REU student Haley Lowes-Bicay, whom I mentored from 2022-2024.

signal preservation. I infer that an interglacial accumulation rate about seven times higher than glacial rates is necessary to match the distribution of smoothed isotope data in 550-750 ka ice.

Differences between the Allan Hills signal and other global records also highlight the influence of local processes on the archival of snow in the Allan Hills. I identify a local decrease in δD, δ^{18}O, and d_{excess} since about 725 ka in all Allan Hills isotope records, which is inconsistent with simple fractionation mechanisms. I speculate that a combination of upstream elevation changes and sublimation of blowing snow could cause the relationships observed in our data, which is perhaps related to the growth of the ice sheet during the MPT.

In Chapter 5, I explore how ocean-atmospheree boundary differences during the Miocene could influence atmospheric distillation pathways for Miocene precipitation logged in Allan Hills ice cores. This preliminary work explores the isotopic response to differences in sea-surface isotopic composition and temperature that determine the initial isotopic conditions of a distillation trajectory. I use a simple water isotope model to isolate these influences and demonstrate that, relative to modern distillation results, changes are in the same direction as observed Allan Hills ice-core measurements. I show that the d_{excess} (modeled as d_{ln}) is especially sensitive to changes at the atmosphere-ocean boundary during evaporation, which is consistent with theory. The direction and magnitude of changes to both d_{ln} and δ^{18}O are consistent with changes likely during a warmer climate state, and these changes are potentially responsible for some or all of the observed change in the meteoric water line for 6-Ma basal ice in ALHIC1902.

BIBLIOGRAPHY

R. P. Acosta, N. J. Burls, M. J. Pound, C. D. Bradshaw, A. M. De Boer, N. Herold, M. Huber, X. Liu, Y. Donnadieu, A. Farnsworth, A. Frigola, D. J. Lunt, A. S. Von Der Heydt, D. K. Hutchinson, G. Knorr, G. Lohmann, A. Marzocchi, M. Prange, A. C. Sarr, X. Li, and Z. Zhang. A Model-Data Comparison of the Hydrological Response to Miocene Warmth: Leveraging the MioMIP1 Opportunistic Multi-Model Ensemble. *Paleoceanog and Paleoclimatol*, 39(1):e2023PA004726, Jan. 2024. ISSN 2572-4517, 2572-4525. doi: 10.1029/2023PA004726.

R. B. Alley, C. A. Shuman, D. A. Meese, A. J. Gow, K. C. Taylor, K. M. Cuffey, J. J. Fitzpatrick, P. M. Grootes, G. A. Zielinski, M. Ram, G. Spinelli, and B. Elder. Visual-stratigraphic dating of the GISP2 ice core: Basis, reproducibility, and application. *J. Geophys. Res.*, 102(C12):26367–26381, Nov. 1997. ISSN 0148-0227. doi: 10.1029/96JC03837.

R. E. Bell, F. Ferraccioli, T. T. Creyts, D. Braaten, H. Corr, I. Das, D. Damaske, N. Frearson, T. Jordan, K. Rose, M. Studinger, and M. Wolovick. Widespread Persistent Thickening of the East Antarctic Ice Sheet by Freezing from the Base. *Science*, 331(6024):1592–1595, Mar. 2011. ISSN 0036-8075, 1095-9203. doi: 10.1126/science.1200109.

M. L. Bender, B. Barnett, G. Dreyfus, J. Jouzel, and D. Porcelli. The contemporary degassing rate of^{40} Ar from the solid Earth. *Proc. Natl. Acad. Sci. U.S.A.*, 105(24):8232–8237, June 2008. ISSN 0027-8424, 1091-6490. doi: 10.1073/pnas.0711679105.

W. Berner, H. Oeschger, and B. Stauffer. Information on the CO_2 Cycle from Ice Core Studies. *Radiocarbon*, 22(2):227–235, 1980. ISSN 0033-8222, 1945-5755. doi: 10.1017/S0033822200009498.

N. A. N. Bertler, P. A. Mayewski, P. J. Barrett, S. B. Sneed, M. J. Handley, and K. J. Kreutz. Monsoonal circulation of the McMurdo Dry Valleys, Ross Sea region, Antarctica: signal from the snow chemistry. *Ann. Glaciol.*, 39:139–145, 2004. ISSN 0260-3055, 1727-5644. doi: 10.3189/172756404781814087.

R. Bintanja. On the glaciological, meteorological, and climatological significance of Antarctic blue ice areas. *Reviews of Geophysics*, 37(3):337–359, Aug. 1999. ISSN 8755-1209, 1944-9208. doi: 10.1029/1999RG900007.

R. Bintanja and R. S. W. Van De Wal. North American ice-sheet dynamics and the onset of 100,000-year glacial cycles. *Nature*, 454(7206):869–872, Aug. 2008. ISSN 0028-0836, 1476-4687. doi: 10.1038/nature07158.

S. Botsyun, T. A. Ehlers, A. Koptev, M. Böhme, K. Methner, C. Risi, C. Stepanek, S. G. Mutz, M. Werner, D. Boateng, and A. Mulch. Middle Miocene Climate and Stable Oxygen Isotopes in Europe Based on Numerical Modeling. *Paleoceanog and Paleoclimatol*, 37(10): e2022PA004442, Oct. 2022. ISSN 2572-4517, 2572-4525. doi: 10.1029/2022PA004442.

E. A. Boyle. Cool tropical temperatures shift the global ^{18} O-T relationship: An explanation for the ice core ^{18} O - borehole thermometry conflict? *Geophysical Research Letters*, 24 (3):273–276, Feb. 1997. ISSN 0094-8276, 1944-8007. doi: 10.1029/97GL00081.

E. Brady, S. Stevenson, D. Bailey, Z. Liu, D. Noone, J. Nusbaumer, B. L. Otto-Bliesner, C. Tabor, R. Tomas, T. Wong, J. Zhang, and J. Zhu. The Connected Isotopic Water Cycle in the Community Earth System Model Version 1. *J Adv Model Earth Syst*, 11(8): 2547–2566, Aug. 2019. ISSN 1942-2466, 1942-2466. doi: 10.1029/2019MS001663.

British Antarctic Survey, United States National Aeronautics and Space Administration, and United States National Science Foundation. Landsat Image Mosaic of Antarctica (LIMA) [Map], 2007.

C. Bréant, C. Leroy Dos Santos, C. Agosta, M. Casado, E. Fourré, S. Goursaud, V. Masson-Delmotte, V. Favier, O. Cattani, F. Prié, B. Golly, A. Orsi, P. Martinerie, and A. Landais. Coastal water vapor isotopic composition driven by katabatic wind variability in summer at Dumont d'Urville, coastal East Antarctica. *Earth and Planetary Science Letters*, 514: 37–47, May 2019. ISSN 0012821X. doi: 10.1016/j.epsl.2019.03.004.

C. Buizert, T. J. Fudge, W. H. G. Roberts, E. J. Steig, S. Sherriff-Tadano, C. Ritz, E. Lefebvre, J. Edwards, K. Kawamura, I. Oyabu, H. Motoyama, E. C. Kahle, T. R. Jones, A. Abe-Ouchi, T. Obase, C. Martin, H. Corr, J. P. Severinghaus, R. Beaudette, J. A. Epifanio, E. J. Brook, K. Martin, J. Chappellaz, S. Aoki, T. Nakazawa, T. A. Sowers, R. B. Alley, J. Ahn, M. Sigl, M. Severi, N. W. Dunbar, A. Svensson, J. M. Fegyveresi, C. He, Z. Liu, J. Zhu, B. L. Otto-Bliesner, V. Y. Lipenkov, M. Kageyama, and J. Schwander. Antarctic surface temperature and elevation during the Last Glacial Maximum. *Science*, 372(6546): 1097–1101, June 2021. ISSN 0036-8075, 1095-9203. doi: 10.1126/science.abd2897.

N. J. Burls, C. D. Bradshaw, A. M. De Boer, N. Herold, M. Huber, M. Pound, Y. Donnadieu, A. Farnsworth, A. Frigola, E. Gasson, A. S. Von Der Heydt, D. K. Hutchinson, G. Knorr, K. T. Lawrence, C. H. Lear, X. Li, G. Lohmann, D. J. Lunt, A. Marzocchi, M. Prange, C. A. Riihimaki, A. Sarr, N. Siler, and Z. Zhang. Simulating Miocene Warmth: Insights From an Opportunistic Multi-Model Ensemble (MioMIP1). *Paleoceanog and Paleoclimatol*, 36(5):e2020PA004054, May 2021. ISSN 2572-4517, 2572-4525. doi: 10.1029/2020PA004054.

P. Caias and J. Jouzel. Deuterium and oxygen 18 in precipitation: Isotopic model, including mixed cloud processes. *J. Geophys. Res.*, 99(D8):16793–16803, Aug. 1994. ISSN 0148-0227. doi: 10.1029/94JD00412.

A. Carter, S. Aarons, J. Epifanio, J. Sutter, A. Choi, C. Tabor, D. Introne, S. Shackleton, P. Gabrielli, J. Higgins, J. Schnaubelt, G. Davies, J. Morgan, J. Severinghaus, J. Marks Peterson, L. Davidge, J. Koornneef, and E. Brook. Evidence for diminished Ross Ice Shelf

and West Antarctic Ice Sheet during the Last Interglacial at the Allan Hills, Antarctica. In *Goldschmidt2024 abstracts*, Chicago, IL, USA, 2024. Geochemical Society. doi: 10.46427/gold2024.21423.

M. Casado, A. Cauquoin, A. Landais, D. Israel, A. Orsi, E. Pangui, J. Landsberg, E. Kerstel, F. Prie, and J.-F. Doussin. Experimental determination and theoretical framework of kinetic fractionation at the water vapour–ice interface at low temperature. *Geochimica et Cosmochimica Acta*, 174:54–69, Feb. 2016a. ISSN 00167037. doi: 10.1016/j.gca.2015.11.009.

M. Casado, A. Landais, V. Masson-Delmotte, C. Genthon, E. Kerstel, S. Kassi, L. Arnaud, G. Picard, F. Prie, O. Cattani, H.-C. Steen-Larsen, E. Vignon, and P. Cermak. Continuous measurements of isotopic composition of water vapour on the EastAntarctic Plateau. *Atmos. Chem. Phys.*, 16(13):8521–8538, July 2016b. ISSN 1680-7324. doi: 10.5194/acp-16-8521-2016.

M. Casado, A. Landais, G. Picard, T. Münch, T. Laepple, B. Stenni, G. Dreossi, A. Ekaykin, L. Arnaud, C. Genthon, A. Touzeau, V. Masson-Delmotte, and J. Jouzel. Archival processes of the water stable isotope signal in East Antarctic ice cores. *The Cryosphere*, 12 (5):1745–1766, May 2018. ISSN 1994-0424. doi: 10.5194/tc-12-1745-2018.

M. Casado, A. Landais, G. Picard, L. Arnaud, G. Dreossi, B. Stenni, and F. Prié. Water Isotopic Signature of Surface Snow Metamorphism in Antarctica. *Geophysical Research Letters*, 48(17):e2021GL093382, Sept. 2021. ISSN 0094-8276, 1944-8007. doi: 10.1029/2021GL093382.

J. Chappellaz, C. Stowasser, T. Blunier, D. Baslev-Clausen, E. J. Brook, R. Dallmayr, X. Faïn, J. E. Lee, L. E. Mitchell, O. Pascual, D. Romanini, J. Rosen, and S. Schüpbach. High-resolution glacial and deglacial record of atmospheric methane by continuous-flow and laser spectrometer analysis along the NEEM ice core. *Clim. Past*, 9(6):2579–2593, Nov. 2013. ISSN 1814-9332. doi: 10.5194/cp-9-2579-2013.

P. U. Clark and D. Pollard. Origin of the Middle Pleistocene Transition by ice sheet erosion of regolith. *Paleoceanography*, 13(1):1–9, Feb. 1998. ISSN 0883-8305, 1944-9186. doi: 10.1029/97PA02660.

P. U. Clark, D. Archer, D. Pollard, J. D. Blum, J. A. Rial, V. Brovkin, A. C. Mix, N. G. Pisias, and M. Roy. The middle Pleistocene transition: characteristics, mechanisms, and implications for long-term changes in atmospheric pCO2. *Quaternary Science Reviews*, 25 (23-24):3150–3184, Dec. 2006. ISSN 02773791. doi: 10.1016/j.quascirev.2006.07.008.

P. U. Clark, J. D. Shakun, Y. Rosenthal, P. Köhler, and P. J. Bartlein. Global and regional temperature change over the past 4.5 million years. *Science*, 383(6685):884–890, Feb. 2024. ISSN 0036-8075, 1095-9203. doi: 10.1126/science.adi1908.

L. Cohen, S. Dean, and J. Renwick. Synoptic Weather Types for the Ross Sea Region, Antarctica. *Journal of Climate*, 26(2):636–649, Jan. 2013. ISSN 0894-8755, 1520-0442. doi: 10.1175/JCLI-D-11-00690.1.

H. Craig. Isotopic Variations in Meteoric Waters. *Science*, 133(3465):1702–1703, May 1961. ISSN 0036-8075, 1095-9203. doi: 10.1126/science.133.3465.1702.

R. Criss. *Principles of Stable Isotope Distribution*. Oxford University Press, Incorporated, 1 edition, 1999.

I. Crotti, A. Landais, B. Stenni, L. Bazin, F. Parrenin, M. Frezzotti, F. Ritterbusch, Z.-T. Lu, W. Jiang, G.-M. Yang, E. Fourré, A. Orsi, R. Jacob, B. Minster, F. Prié, G. Dreossi, and C. Barbante. An extension of the TALDICE ice core age scale reaching back to MIS 10.1. *Quaternary Science Reviews*, 266:107078, Aug. 2021. ISSN 02773791. doi: 10.1016/j.quascirev.2021.107078.

K. M. Cuffey and E. J. Steig. Isotopic diffusion in polar firn: implications for interpretation of seasonal climate parameters in ice-core records, with emphasis on cen-

tral Greenland. *J. Glaciol.*, 44(147):273–284, 1998. ISSN 0022-1430, 1727-5652. doi: 10.3189/S0022143000002616.

K. M. Cuffey and F. Vimeux. Covariation of carbon dioxide and temperature from the Vostok ice core after deuterium-excess correction. *Nature*, 412(6846):523–527, Aug. 2001. ISSN 0028-0836, 1476-4687. doi: 10.1038/35087544.

R. Dadic, M. Schneebeli, N. A. Bertler, M. Schwikowski, and M. Matzl. Extreme snow metamorphism in the Allan Hills, Antarctica, as an analogue for glacial conditions with implications for stable isotope composition. *J. Glaciol.*, 61(230):1171–1182, 2015. ISSN 0022-1430, 1727-5652. doi: 10.3189/2015JoG15J027.

D. Dahl-Jensen, T. Thorsteinsson, R. Alley, and H. Shoji. Flow properties of the ice from the Greenland Ice Core Project ice core: The reason for folds? *J. Geophys. Res.*, 102 (C12):26831–26840, Nov. 1997. ISSN 0148-0227. doi: 10.1029/97JC01266.

W. Dansgaard. Stable isotopes in precipitation. *Tellus*, 16(4):436–468, Nov. 1964. ISSN 00402826, 21533490. doi: 10.1111/j.2153-3490.1964.tb00181.x.

W. Dansgaard. *Stable isotope glaciology*. C.A. Reitzel, 1973.

W. Dansgaard and S. J. Johnsen. A Flow Model and a Time Scale for the Ice Core from Camp Century, Greenland. *J. Glaciol.*, 8(53):215–223, 1969. ISSN 0022-1430, 1727-5652. doi: 10.3189/S0022143000031208.

W. Dansgaard, S. J. Johnsen, H. B. Clausen, and N. Gundestrup. Stable Isotope Glaciology. *Meddr Grønland*, 197(2), Jan. 1973. ISSN 2794-6827. doi: 10.7146/mog.v197.147754.

W. Dansgaard, J. W. C. White, and S. J. Johnsen. The abrupt termination of the Younger Dryas climate event. *Nature*, 339(6225):532–534, June 1989. ISSN 0028-0836, 1476-4687. doi: 10.1038/339532a0.

W. Dansgaard, S. J. Johnsen, H. B. Clausen, D. Dahl-Jensen, N. S. Gundestrup, C. U. Hammer, C. S. Hvidberg, J. P. Steffensen, A. E. Sveinbjörnsdottir, J. Jouzel, and G. Bond. Evidence for general instability of past climate from a 250-kyr ice-core record. *Nature*, 364 (6434):218–220, July 1993. ISSN 1476-4687. doi: 10.1038/364218a0.

L. Davidge, E. J. Steig, and A. J. Schauer. Improving continuous-flow analysis of triple oxygen isotopes in ice cores: insights from replicate measurements. *Atmos. Meas. Tech.*, 15(24):7337–7351, Dec. 2022. ISSN 1867-8548. doi: 10.5194/amt-15-7337-2022.

G. H. Denton and D. E. Sugden. Meltwater features that suggest miocene ice-sheet overriding of the transantarctic mountains in victoria land, antarctica. *Geografiska Annaler: Series A, Physical Geography*, 87(1):67–85, Mar. 2005. ISSN 0435-3676, 1468-0459. doi: 10.1111/j.0435-3676.2005.00245.x.

M. Dütsch, P. N. Blossey, E. J. Steig, and J. M. Nusbaumer. Nonequilibrium Fractionation During Ice Cloud Formation in iCAM5: Evaluating the Common Parameterization of Supersaturation as a Linear Function of Temperature. *J Adv Model Earth Syst*, 11(11): 3777–3793, Nov. 2019. ISSN 1942-2466, 1942-2466. doi: 10.1029/2019MS001764.

EPICA community members. Eight glacial cycles from an Antarctic ice core. *Nature*, 429 (6992):623–628, June 2004. ISSN 0028-0836, 1476-4687. doi: 10.1038/nature02599.

E. et al. Rapid Comm Mass Spectrometry - 2013 - Ellehoj - Ice-vapor equilibrium fractionation factor of hydrogen and oxygen isotopes .pdf, 2013.

J. R. Farmer, K. J. Keller, R. K. Poirier, G. S. Dwyer, M. F. Schaller, H. K. Coxall, M. O'Regan, and T. M. Cronin. A 600 kyr reconstruction of deep Arctic seawater ^{18} O from benthic foraminiferal ^{18} O and ostracode Mg Ca paleothermometry. *Clim. Past*, 19(3):555–578, Mar. 2023. ISSN 1814-9332. doi: 10.5194/cp-19-555-2023.

H. C. Fricke and J. R. O'Neil. The correlation between 18O/16O ratios of meteoric water and surface temperature: its use in investigating terrestrial climate change over geologic

time. *Earth and Planetary Science Letters*, 170(3):181–196, July 1999. ISSN 0012821X. doi: 10.1016/S0012-821X(99)00105-3.

R. Garzonio, B. Di Mauro, S. Cogliati, M. Rossini, C. Panigada, B. Delmonte, V. Maggi, and R. Colombo. A novel hyperspectral system for high resolution imaging of ice cores: Application to light-absorbing impurities and ice structure. *Cold Regions Science and Technology*, 155:47–57, Nov. 2018. ISSN 0165232X. doi: 10.1016/j.coldregions.2018.07.005.

H. Gildor and E. Tziperman. Sea ice as the glacial cycles' Climate switch: role of seasonal and orbital forcing. *Paleoceanography*, 15(6):605–615, Dec. 2000. ISSN 0883-8305, 1944-9186. doi: 10.1029/1999PA000461.

H. Gildor and E. Tziperman. A sea ice climate switch mechanism for the 100-kyr glacial cycles. *J. Geophys. Res.*, 106(C5):9117–9133, May 2001. ISSN 0148-0227. doi: 10.1029/1999JC000120.

V. Gkinis, S. Simonsen, S. Buchardt, J. White, and B. Vinther. Water isotope diffusion rates from the NorthGRIP ice core for the last 16,000 years – Glaciological and paleoclimatic implications. *Earth and Planetary Science Letters*, 405:132–141, Nov. 2014. ISSN 0012821X. doi: 10.1016/j.epsl.2014.08.022.

V. Gkinis, B. M. Vinther, T. Quistgaard, T. Popp, A.-K. Faber, C. T. Holme, C. M. Jensen, M. Lanzky, A. M. Lütt, V. Mandrakis, N. O. Ørum, A.-S. Pedersen, N. Vaxevani, Y. Weng, E. Capron, D. Dahl-Jensen, M. Hörhold, T. R. Jones, J. Jouzel, A. Landais, V. Masson-Delmotte, H. Oerter, S. O. Rasmussen, H. C. Steen-Larsen, J. P. Steffensen, E. Sveinbjörnsdottir, B. H. Vaughn, and J. White. NEEM ice core High Resolution (0.05m) Water Isotope Ratios (18O/16O, 2H/1H) covering 8-129 ky b2k, 2020. Type: dataset.

V. Gkinis, C. Holme, E. C. Kahle, M. C. Stevens, E. J. Steig, and B. M. Vinther. Numerical experiments on firn isotope diffusion with the Community Firn Model. *J. Glaciol.*, 67 (263):450–472, June 2021a. ISSN 0022-1430, 1727-5652. doi: 10.1017/jog.2021.1.

V. Gkinis, B. M. Vinther, T. J. Popp, T. Quistgaard, A.-K. Faber, C. T. Holme, C.-M. Jensen, M. Lanzky, A.-M. Lütt, V. Mandrakis, N.-O. Ørum, A.-S. Pedersen, N. Vaxevani, Y. Weng, E. Capron, D. Dahl-Jensen, M. Hörhold, T. R. Jones, J. Jouzel, A. Landais, V. Masson-Delmotte, H. Oerter, S. O. Rasmussen, H. C. Steen-Larsen, J.-P. Steffensen, -E. Sveinbjörnsdóttir, A. Svensson, B. Vaughn, and J. W. C. White. A 120,000-year long climate record from a NW-Greenland deep ice core at ultra-high resolution. *Sci Data*, 8 (1):141, May 2021b. ISSN 2052-4463. doi: 10.1038/s41597-021-00916-9.

Gonfiantini and Picciotto. Oxygen Isotope Variations in Antarctic Snow Samples. 184, Nov. 1959.

M. N. Gooseff, W. B. Lyons, D. M. McKnight, B. H. Vaughn, A. G. Fountain, and C. Dowling. A Stable Isotopic Investigation of a Polar Desert Hydrologic System, McMurdo Dry Valleys, Antarctica. *Arctic, Antarctic, and Alpine Research*, 38(1):60–71, Feb. 2006. ISSN 1523-0430, 1938-4246. doi: 10.1657/1523-0430(2006)038[0060:ASIIOA]2.0.CO;2.

L. J. Gregoire, A. J. Payne, and P. J. Valdes. Deglacial rapid sea level rises caused by ice-sheet saddle collapses. *Nature*, 487(7406):219–222, July 2012. ISSN 0028-0836, 1476-4687. doi: 10.1038/nature11257.

A. Grisart, M. Casado, V. Gkinis, B. Vinther, P. Naveau, M. Vrac, T. Laepple, B. Minster, F. Prié, B. Stenni, E. Fourré, H. C. Steen-Larsen, J. Jouzel, M. Werner, K. Pol, V. Masson-Delmotte, M. Hoerhold, T. Popp, and A. Landais. Sub-millennial climate variability from high-resolution water isotopes in the EPICA Dome C ice core. *Clim. Past*, 18(10):2289–2301, Oct. 2022. ISSN 1814-9332. doi: 10.5194/cp-18-2289-2022.

J. E. Hansen, T. Takahashi, and American Geophysical Union, editors. *Climate processes and climate sensitivity.* Number v. 5 in Maurice Ewing. American Geophysical Union, Washington, D.C, 2010. ISBN 978-0-87590-404-7 978-1-118-66603-6.

Hays. Variations in the Earth's Orbit: Pacemaker of the Ice Ages. 1976.

J. A. Higgins, A. V. Kurbatov, N. E. Spaulding, E. Brook, D. S. Introne, L. M. Chimiak, Y. Yan, P. A. Mayewski, and M. L. Bender. Atmospheric composition 1 million years ago from blue ice in the Allan Hills, Antarctica. *Proc. Natl. Acad. Sci. U.S.A.*, 112(22): 6887–6891, June 2015. ISSN 0027-8424, 1091-6490. doi: 10.1073/pnas.1420232112.

I. M. Howat, C. Porter, B. E. Smith, M.-J. Noh, and P. Morin. The Reference Elevation Model of Antarctica. *The Cryosphere*, 13(2):665–674, Feb. 2019. ISSN 1994-0424. doi: 10.5194/tc-13-665-2019.

J. Hu, Y. Yan, L. Y. Yeung, and S. G. Dee. Sublimation Origin of Negative Deuterium Excess Observed in Snow and Ice Samples From McMurdo Dry Valleys and Allan Hills Blue Ice Areas, East Antarctica. *JGR Atmospheres*, 127(11):e2021JD035950, June 2022. ISSN 2169-897X, 2169-8996. doi: 10.1029/2021JD035950.

A. Hudak, A. Banerjee, E. Brook, C. Buizert, M. Sliwinski, L. Davidge, E. Steig, A. Schauer, N. Brown, M. Miranda, and E. Saltzman. Development of a Continuous Flow Analysis system for studying Allan Hills, Antarctica ice cores, 2024.

P. Huybrechts, O. Rybak, F. Pattyn, U. Ruth, and D. Steinhage. Ice thinning, upstream advection, and non-climatic biases for the upper 89% of the EDML ice core from a nested model of the Antarctic ice sheet. *Clim. Past*, 2007.

S. Johnsen, H. Clausen, K. Duffey, G. Hoffmann, J. Schwander, and T. Cryts. *Diffusion of stable isotopes in polar firn and ice: the isotope effect in firn diffusion*, pages 121–140. Hokkaido University, Japan, 2000.

S. J. Johnsen, W. Dansgaard, and J. W. C. White. The origin of Arctic precipitation under present and glacial conditions. *Tellus B*, 41B(4):452–468, Sept. 1989. ISSN 02806509, 16000889. doi: 10.1111/j.1600-0889.1989.tb00321.x.

S. J. Johnsen, H. B. Clausen, W. Dansgaard, N. S. Gundestrup, C. U. Hammer, and H. Tauber. The Eem Stable Isotope Record along the GRIP Ice Core and Its Inter-

pretation. *Quat. res.*, 43(2):117–124, Mar. 1995a. ISSN 0033-5894, 1096-0287. doi: 10.1006/qres.1995.1013.

S. J. Johnsen, D. Dahl-Jensen, W. Dansgaard, and N. Gundestrup. Greenland palaeotemperatures derived from GRIP bore hole temperature and ice core isotope profiles. *Tellus B*, 47(5):624–629, Nov. 1995b. ISSN 0280-6509, 1600-0889. doi: 10.1034/j.1600-0889.47.issue5.9.x.

S. J. Johnsen, D. Dahl-Jensen, N. Gundestrup, J. P. Steffensen, H. B. Clausen, H. Miller, V. Masson-Delmotte, A. E. Sveinbjörnsdottir, and J. White. Oxygen isotope and palaeotemperature records from six Greenland ice-core stations: Camp Century, Dye-3, GRIP, GISP2, Renland and NorthGRIP. *J Quaternary Science*, 16(4):299–307, May 2001. ISSN 0267-8179, 1099-1417. doi: 10.1002/jqs.622.

T. R. Jones, K. M. Cuffey, J. W. C. White, E. J. Steig, C. Buizert, B. R. Markle, J. R. McConnell, and M. Sigl. Water isotope diffusion in the WAIS Divide ice core during the Holocene and last glacial. *J. Geophys. Res. Earth Surf.*, 122(1):290–309, Jan. 2017a. ISSN 2169-9003, 2169-9011. doi: 10.1002/2016JF003938.

T. R. Jones, J. W. C. White, E. J. Steig, B. H. Vaughn, V. Morris, V. Gkinis, B. R. Markle, and S. W. Schoenemann. Improved methodologies for continuous-flow analysis of stable water isotopes in ice cores. *Atmos. Meas. Tech.*, 10(2):617–632, Feb. 2017b. ISSN 1867-8548. doi: 10.5194/amt-10-617-2017.

J. Jouzel. Calibrating the Isotopic Paleothermometer. *Science*, 286(5441):910–911, Oct. 1999. ISSN 0036-8075, 1095-9203. doi: 10.1126/science.286.5441.910.

J. Jouzel and L. Merlivat. Deuterium and oxygen 18 in precipitation: Modeling of the isotopic effects during snow formation. *J. Geophys. Res.*, 89(D7):11749–11757, Dec. 1984. ISSN 0148-0227. doi: 10.1029/JD089iD07p11749.

J. Jouzel, L. Merlivat, and C. Lorius. Deuterium excess in an East Antarctic ice core suggests higher relative humidity at the oceanic surface during the last glacial maximum. *Nature*, 299(5885):688–691, Oct. 1982. ISSN 0028-0836, 1476-4687. doi: 10.1038/299688a0.

J. Jouzel, K. Froehlich, and U. Schotterer. Deuterium and oxygen-18 in present-day precipitation: data and modelling. *Hydrological Sciences Journal*, 42(5):747–763, Oct. 1997. ISSN 0262-6667, 2150-3435. doi: 10.1080/02626669709492070.

J. Jouzel, F. Vimeux, N. Caillon, G. Delaygue, G. Hoffmann, V. Masson-Delmotte, and F. Parrenin. Magnitude of isotope/temperature scaling for interpretation of central Antarctic ice cores. *J. Geophys. Res.*, 108(D12):2002JD002677, June 2003. ISSN 0148-0227. doi: 10.1029/2002JD002677.

J. Jouzel, V. Masson-Delmotte, O. Cattani, G. Dreyfus, S. Falourd, G. Hoffmann, B. Minster, J. Nouet, J. M. Barnola, J. Chappellaz, H. Fischer, J. C. Gallet, S. Johnsen, M. Leuenberger, L. Loulergue, D. Luethi, H. Oerter, F. Parrenin, G. Raisbeck, D. Raynaud, A. Schilt, J. Schwander, E. Selmo, R. Souchez, R. Spahni, B. Stauffer, J. P. Steffensen, B. Stenni, T. F. Stocker, J. L. Tison, M. Werner, and E. W. Wolff. Orbital and Millennial Antarctic Climate Variability over the Past 800,000 Years. *Science*, 317(5839):793–796, Aug. 2007. ISSN 0036-8075, 1095-9203. doi: 10.1126/science.1141038.

J. L. Kavanaugh and K. M. Cuffey. Space and time variation of ^{18} O and D in Antarctic precipitation revisited. *Global Biogeochemical Cycles*, 17(1):2002GB001910, Mar. 2003. ISSN 0886-6236, 1944-9224. doi: 10.1029/2002GB001910.

L. Kehrl, H. Conway, N. Holschuh, S. Campbell, A. V. Kurbatov, and N. E. Spaulding. Evaluating the Duration and Continuity of Potential Climate Records From the Allan Hills Blue Ice Area, East Antarctica. *Geophysical Research Letters*, 45(9):4096–4104, May 2018. ISSN 0094-8276, 1944-8007. doi: 10.1029/2018GL077511.

L. Kirkpatrick, A. Carter, J. Marks Peterson, S. Shackleton, and T. Fudge. Three-

Dimensional Multitrack Electrical Conductivity Method for Interpretation of Complex Ice Core Stratigraphy, Nov. 2024.

P. Kohler and R. Bintanja. The carbon cycle during the Mid Pleistocene Transition: the Southern Ocean Decoupling Hypothesis. *Clim. Past*, 2008.

B. G. Kopec, A. M. Lauder, E. S. Posmentier, and X. Feng. The diel cycle of water vapor in west Greenland. *JGR Atmospheres*, 119(15):9386–9399, Aug. 2014. ISSN 2169-897X, 2169-8996. doi: 10.1002/2014JD021859.

T. Laepple, T. Münch, M. Casado, M. Hoerhold, A. Landais, and S. Kipfstuhl. On the similarity and apparent cycles of isotopic variations in East Antarctic snow pits. *The Cryosphere*, 12(1):169–187, Jan. 2018. ISSN 1994-0424. doi: 10.5194/tc-12-169-2018.

F. Lambert, B. Delmonte, J. R. Petit, M. Bigler, P. R. Kaufmann, M. A. Hutterli, T. F. Stocker, U. Ruth, J. P. Steffensen, and V. Maggi. Dust-climate couplings over the past 800,000 years from the EPICA Dome C ice core. *Nature*, 452(7187):616–619, Apr. 2008. ISSN 0028-0836, 1476-4687. doi: 10.1038/nature06763.

A. Landais, E. Barkan, and B. Luz. Record of ^{18}O and^{17}O-excess in ice from Vostok Antarctica during the last 150,000 years. *Geophysical Research Letters*, 35(2):2007GL032096, Jan. 2008. ISSN 0094-8276, 1944-8007. doi: 10.1029/2007GL032096.

A. Landais, B. Stenni, V. Masson-Delmotte, J. Jouzel, A. Cauquoin, E. Fourré, B. Minster, E. Selmo, T. Extier, M. Werner, F. Vimeux, R. Uemura, I. Crotti, and A. Grisart. Interglacial Antarctic–Southern Ocean climate decoupling due to moisture source area shifts. *Nat. Geosci.*, 14(12):918–923, Dec. 2021. ISSN 1752-0894, 1752-0908. doi: 10.1038/s41561-021-00856-4.

P. M. Langebroek, A. Paul, and M. Schulz. Simulating the sea level imprint on marine oxygen isotope records during the middle Miocene using an ice sheet-climate model: mod-

eling oxygen isotopes in the miocene. *Paleoceanography*, 25(4):n/a–n/a, Dec. 2010. ISSN 08838305. doi: 10.1029/2008PA001704.

C. C. Langway. A 400 Meter Deep Ice Core in Greenland: Preliminary Report. *J. Glaciol.*, 3(23):217–217, 1958. ISSN 0022-1430, 1727-5652. doi: 10.3189/S0022143000024278.

M. Lehmann and U. Siegenthaler. Equilibrium oxygen- and hydrogen-isotope fractionation between ice and water. *J. Glaciol.*, 37(125):23–26, 1991. ISSN 0022-1430, 1727-5652. doi: 10.3189/S0022143000042751.

L. E. Lisiecki and M. E. Raymo. A Pliocene-Pleistocene stack of 57 globally distributed benthic ^{18} O records. *Paleoceanography*, 20(1):2004PA001071, Mar. 2005. ISSN 0883-8305, 1944-9186. doi: 10.1029/2004PA001071.

C. Lorius, L. Merlivat, and R. Hagemann. Variation in the mean deuterium content of precipitations in Antarctica. *J. Geophys. Res.*, 74(28):7027–7031, Dec. 1969. ISSN 01480227. doi: 10.1029/JC074i028p07027.

L. Loulergue, A. Schilt, R. Spahni, V. Masson-Delmotte, T. Blunier, B. Lemieux, J.-M. Barnola, D. Raynaud, T. F. Stocker, and J. Chappellaz. Orbital and millennial-scale features of atmospheric CH4 over the past 800,000 years. *Nature*, 453(7193):383–386, May 2008. ISSN 0028-0836, 1476-4687. doi: 10.1038/nature06950.

B. Luz and E. Barkan. Variations of 17O/16O and 18O/16O in meteoric waters. *Geochimica et Cosmochimica Acta*, 74(22):6276–6286, Nov. 2010. ISSN 00167037. doi: 10.1016/j.gca.2010.08.016.

D. Lüthi, M. Le Floch, B. Bereiter, T. Blunier, J.-M. Barnola, U. Siegenthaler, D. Raynaud, J. Jouzel, H. Fischer, K. Kawamura, and T. F. Stocker. High-resolution carbon dioxide concentration record 650,000–800,000 years before present. *Nature*, 453(7193):379–382, May 2008. ISSN 0028-0836, 1476-4687. doi: 10.1038/nature06949.

M. Majoube. Fractionation Factor of d18O between Water Vapour and Ice. *Nature*, 226, June 1970.

B. R. Markle and E. J. Steig. Improving temperature reconstructions from ice-core water-isotope records. preprint, Proxy Use-Development-Validation/Ice Cores/Milankovitch, Apr. 2021.

B. R. Markle, E. J. Steig, C. Buizert, S. W. Schoenemann, C. M. Bitz, T. J. Fudge, J. B. Pedro, Q. Ding, T. R. Jones, J. W. C. White, and T. Sowers. Global atmospheric teleconnections during Dansgaard–Oeschger events. *Nature Geosci*, 10(1):36–40, Jan. 2017. ISSN 1752-0894, 1752-0908. doi: 10.1038/ngeo2848.

J. Marks Peterson, S. Shackleton, J. Severinghaus, E. Brook, J. Higgins, A. Kurbatov, Y. Yan, C. Buizert, M. Kalk, R. Beaudette, A. Carter, J. Epifanio, and J. Morgan. Late Pliocene and Early Pleistocene CO2 and CH4 from ice cores from the Allan Hills, Antarctica. 2024. doi: 10.5194/egusphere-egu24-6781.

S. J. Marshall and P. U. Clark. Basal temperature evolution of North American ice sheets and implications for the 100-kyr cycle. *Geophysical Research Letters*, 29(24), Dec. 2002. ISSN 0094-8276, 1944-8007. doi: 10.1029/2002GL015192.

V. Masson-Delmotte, S. Hou, A. Ekaykin, J. Jouzel, A. Aristarain, R. T. Bernardo, D. Bromwich, O. Cattani, M. Delmotte, S. Falourd, M. Frezzotti, H. Gallée, L. Genoni, E. Isaksson, A. Landais, M. M. Helsen, G. Hoffmann, J. Lopez, V. Morgan, H. Motoyama, D. Noone, H. Oerter, J. R. Petit, A. Royer, R. Uemura, G. A. Schmidt, E. Schlosser, J. C. Simões, E. J. Steig, B. Stenni, M. Stievenard, M. R. Van Den Broeke, R. S. W. Van De Wal, W. J. Van De Berg, F. Vimeux, and J. W. C. White. A Review of Antarctic Surface Snow Isotopic Composition: Observations, Atmospheric Circulation, and Isotopic Modeling*. *Journal of Climate*, 21(13):3359–3387, July 2008. ISSN 1520-0442, 0894-8755. doi: 10.1175/2007JCLI2139.1.

I. E. McDowell, K. M. Keegan, S. M. Skiles, C. P. Donahue, E. C. Osterberg, R. L. Hawley, and H.-P. Marshall. A cold laboratory hyperspectral imaging system to map grain size and ice layer distributions in firn cores. *The Cryosphere*, 18(4):1925–1946, Apr. 2024. ISSN 1994-0424. doi: 10.5194/tc-18-1925-2024.

L. Merlivat and J. Jouzel. Global climatic interpretation of the deuterium-oxygen 18 relationship for precipitation. *J. Geophys. Res.*, 84(C8):5029, 1979. ISSN 0148-0227. doi: 10.1029/JC084iC08p05029.

L. Merlivat and C. Lorius. Traceurs isotopiques et glaciologie. *La Houille Blanche*, 62(3-4): 285–289, June 1976. ISSN 0018-6368, 1958-5551. doi: 10.1051/lhb/1976017.

J. Nusbaumer, T. E. Wong, C. Bardeen, and D. Noone. Evaluating hydrological processes in the Community Atmosphere Model Version 5 (CAM5) using stable isotope ratios of water. *J Adv Model Earth Syst*, 9(2):949–977, June 2017. ISSN 1942-2466, 1942-2466. doi: 10.1002/2016MS000839.

T. H. Nylen, A. G. Fountain, and P. T. Doran. Climatology of katabatic winds in the McMurdo dry valleys, southern Victoria Land, Antarctica. *J. Geophys. Res.*, 109(D3): 2003JD003937, Feb. 2004. ISSN 0148-0227. doi: 10.1029/2003JD003937.

T. R. Parish and J. J. Cassano. The Role of Katabatic Winds on the Antarctic Surface Wind Regime. *Mon. Wea. Rev.*, 131(2):317–333, Feb. 2003. ISSN 0027-0644, 1520-0493. doi: 10.1175/1520-0493(2003)131¡0317:TROKWO¿2.0.CO;2.

J. R. Petit, J. Jouzel, D. Raynaud, N. I. Barkov, G. Delaygue, M. Delmotte, V. M. Kotlyakov, M. Legrand, V. Y. Lipenkov, C. Lorius, and E. Saltzman. Climate and atmospheric history of the past 420,000 years from the Vostok ice core, Antarctica. 399, 1999.

K. Pol, V. Masson-Delmotte, S. Johnsen, M. Bigler, O. Cattani, G. Durand, S. Falourd, J. Jouzel, B. Minster, F. Parrenin, C. Ritz, H. Steen-Larsen, and B. Stenni. New MIS 19 EPICA Dome C high resolution deuterium data: Hints for a problematic preservation of

climate variability at sub-millennial scale in the "oldest ice". *Earth and Planetary Science Letters*, 298(1-2):95–103, Sept. 2010. ISSN 0012821X. doi: 10.1016/j.epsl.2010.07.030.

R. O. Ramseier. Self-Diffusion of Tritium in Natural and Synthetic Ice Monocrystals. *Journal of Applied Physics*, 38(6):2553–2556, May 1967. ISSN 0021-8979, 1089-7550. doi: 10.1063/1.1709948.

C. F. Raymond. Deformation in the Vicinity of Ice Divides. *J. Glaciol.*, 29(103):357–373, 1983. ISSN 0022-1430, 1727-5652. doi: 10.3189/S0022143000030288.

G. H. Roe and M. R. Allan. Geophysical Research Letters - 1999 - Roe - A comparison of competing explanations for the 100 000-yr Ice Age cycle.pdf, 1999.

G. H. Roe and M. R. Allen. A comparison of competing explanations for the 100,000-yr Ice Age cycle. *Geophysical Research Letters*, 26(15):2259–2262, Aug. 1999. ISSN 0094-8276, 1944-8007. doi: 10.1029/1999GL900509.

I. F. Rowell, R. Mulvaney, J. Rix, D. R. Tetzner, and E. W. Wolff. Viability of chemical and water isotope ratio measurements of RAID ice chippings from Antarctica. *J. Glaciol.*, 69 (275):623–638, June 2023. ISSN 0022-1430, 1727-5652. doi: 10.1017/jog.2022.94.

A. J. Schauer, S. W. Schoenemann, and E. J. Steig. Routine high-precision analysis of triple water-isotope ratios using cavity ring-down spectroscopy: High-precision analysis of triple water-isotope ratios. *Rapid Commun. Mass Spectrom.*, 30(18):2059–2069, Sept. 2016. ISSN 09514198. doi: 10.1002/rcm.7682.

S. W. Schoenemann and E. J. Steig. Seasonal and spatial variations of ^{17}O $_{\text{excess}}$ and d $_{\text{excess}}$ in Antarctic precipitation: Insights from an intermediate complexity isotope model. *JGR Atmospheres*, 121(19), Oct. 2016. ISSN 2169-897X, 2169-8996. doi: 10.1002/2016JD025117.

S. W. Schoenemann, A. J. Schauer, and E. J. Steig. Measurement of SLAP2 and GISP ^{17}O and proposed VSMOW-SLAP normalization for ^{17}O and ^{17}O $_{\text{excess}}$: Measurement of

SLAP2 and GISP ^{17} O values. *Rapid Commun. Mass Spectrom.*, 27(5):582–590, Mar. 2013. ISSN 09514198. doi: 10.1002/rcm.6486.

S. W. Schoenemann, E. J. Steig, Q. Ding, B. R. Markle, and A. J. Schauer. Triple water-isotopologue record from WAIS Divide, Antarctica: Controls on glacial-interglacial changes in ^{17} O $_{\text{excess}}$ of precipitation: WAIS LGM-Holocene 17Oexcess Record. *J. Geophys. Res. Atmos.*, 119(14):8741–8763, July 2014. ISSN 2169897X. doi: 10.1002/2014JD021770.

N. J. Shackleton and N. D. Opdyke. Oxygen isotope and palaeomagnetic evidence for early Northern Hemisphere glaciation. *Nature*, 270(5634):216–219, Nov. 1977. ISSN 0028-0836, 1476-4687. doi: 10.1038/270216a0.

S. Shackleton and Allan Hills Blue Ice Coring Team. Early-Mid Pleistocene ice core records of Antarctic and global cooling. 2024. doi: 10.5194/egusphere-egu24-14335.

S. Shackleton, V. Hishamunda, L. Davidge, E. Brook, J. M. Peterson, A. Carter, S. Aarons, A. Kurbatov, D. Introne, Y. Yan, C. Buizert, E. Steig, A. Schauer, J. Morgan, J. Severinghaus, M. Bender, P. Neff, J. Epifanio, and J. Higgins. Miocene and Pliocene ice and air from the Allan Hills blue ice area, East Antarctica. Preprint. doi: 10.22541/essoar.173897232.24923969/v1.

J. D. Shakun, P. U. Clark, F. He, S. A. Marcott, A. C. Mix, Z. Liu, B. Otto-Bliesner, A. Schmittner, and E. Bard. Global warming preceded by increasing carbon dioxide concentrations during the last deglaciation. *Nature*, 484(7392):49–54, Apr. 2012. ISSN 0028-0836, 1476-4687. doi: 10.1038/nature10915.

B. Silverman. *Density estimation for statistics and data analysis*. Chapman and Hall, 1986.

A. Sinisalo and J. C. Moore. Antarctic blue ice areas - towards extracting palaeoclimate information. *Antarctic Science*, 22(2):99–115, Apr. 2010. ISSN 0954-1020, 1365-2079. doi: 10.1017/S0954102009990691.

N. E. Spaulding, V. B. Spikes, G. S. Hamilton, P. A. Mayewski, N. W. Dunbar, R. P. Harvey, J. Schutt, and A. V. Kurbatov. Ice motion and mass balance at the Allan Hills blue-ice area, Antarctica, with implications for paleoclimate reconstructions. *J. Glaciol.*, 58(208): 399–406, 2012. ISSN 0022-1430, 1727-5652. doi: 10.3189/2012JoG11J176.

N. E. Spaulding, J. A. Higgins, A. V. Kurbatov, M. L. Bender, S. A. Arcone, S. Campbell, N. W. Dunbar, L. M. Chimiak, D. S. Introne, and P. A. Mayewski. Climate archives from 90 to 250 ka in horizontal and vertical ice cores from the Allan Hills Blue Ice Area, Antarctica. *Quat. res.*, 80(3):562–574, Nov. 2013. ISSN 0033-5894, 1096-0287. doi: 10.1016/j.yqres.2013.07.004.

E. J. Steig, V. Gkinis, A. J. Schauer, S. W. Schoenemann, K. Samek, J. Hoffnagle, K. J. Dennis, and S. M. Tan. Calibrated high-precision 17O-excess measurements using cavity ring-down spectroscopy with laser-current-tuned cavity resonance. *Atmos. Meas. Tech.*, 7 (8):2421–2435, Aug. 2014. ISSN 1867-8548. doi: 10.5194/amt-7-2421-2014.

E. J. Steig, T. R. Jones, A. J. Schauer, E. C. Kahle, V. A. Morris, B. H. Vaughn, L. Davidge, and J. W. White. Continuous-Flow Analysis of 17O, 18O, and D of H2O on an Ice Core from the South Pole. *Front. Earth Sci.*, 9:640292, Mar. 2021. ISSN 2296-6463. doi: 10.3389/feart.2021.640292.

B. Stenni, V. Masson-Delmotte, E. Selmo, H. Oerter, H. Meyer, R. Röthlisberger, J. Jouzel, O. Cattani, S. Falourd, H. Fischer, G. Hoffmann, P. Iacumin, S. Johnsen, B. Minster, and R. Udisti. The deuterium excess records of EPICA Dome C and Dronning Maud Land ice cores (East Antarctica). *Quaternary Science Reviews*, 29(1-2):146–159, Jan. 2010. ISSN 02773791. doi: 10.1016/j.quascirev.2009.10.009.

N. Stoll, J. Eichler, M. Hörhold, T. Erhardt, C. Jensen, and I. Weikusat. Microstructure, micro-inclusions, and mineralogy along the EGRIP ice core – Part 1: Localisation of inclusions and deformation patterns. *The Cryosphere*, 15(12):5717–5737, Dec. 2021. ISSN 1994-0424. doi: 10.5194/tc-15-5717-2021.

N. Stoll, M. Hörhold, T. Erhardt, J. Eichler, C. Jensen, and I. Weikusat. Microstructure, micro-inclusions, and mineralogy along the EGRIP (East Greenland Ice Core Project) ice core – Part 2: Implications for palaeo-mineralogy. *The Cryosphere*, 16(2):667–688, Feb. 2022. ISSN 1994-0424. doi: 10.5194/tc-16-667-2022.

R. Uemura, E. Barkan, O. Abe, and B. Luz. Triple isotope composition of oxygen in atmospheric water vapor: the ^{17} O-excess of water vapor. *Geophys. Res. Lett.*, 37(4), Feb. 2010. ISSN 00948276. doi: 10.1029/2009GL041960.

R. Uemura, V. Masson-Delmotte, J. Jouzel, A. Landais, H. Motoyama, and B. Stenni. Ranges of moisture-source temperature estimated from Antarctic ice cores stable isotope records over glacial–interglacial cycles. *Clim. Past*, 8(3):1109–1125, June 2012. ISSN 1814-9332. doi: 10.5194/cp-8-1109-2012.

R. Uemura, H. Motoyama, V. Masson-Delmotte, J. Jouzel, K. Kawamura, K. Goto-Azuma, S. Fujita, T. Kuramoto, M. Hirabayashi, T. Miyake, H. Ohno, K. Fujita, A. Abe-Ouchi, Y. Iizuka, S. Horikawa, M. Igarashi, K. Suzuki, T. Suzuki, and Y. Fujii. Asynchrony between Antarctic temperature and CO2 associated with obliquity over the past 720,000 years. *Nat Commun*, 9(1):961, Mar. 2018. ISSN 2041-1723. doi: 10.1038/s41467-018-03328-3.

F. Vimeux, V. Masson, G. Delaygue, J. Jouzel, J. R. Petit, and M. Stievenard. A 420,000 year deuterium excess record from East Antarctica: Information on past changes in the origin of precipitation at Vostok. *J. Geophys. Res.*, 106(D23):31863–31873, Dec. 2001. ISSN 0148-0227. doi: 10.1029/2001JD900076.

S. Wahl, H. C. Steen-Larsen, J. Reuder, and M. Hörhold. Quantifying the Stable Water Isotopologue Exchange Between the Snow Surface and Lower Atmosphere by Direct Flux Measurements. *JGR Atmospheres*, 126(13):e2020JD034400, July 2021. ISSN 2169-897X, 2169-8996. doi: 10.1029/2020JD034400.

O. Watanabe, K. Kamiyama, H. Motoyama, Y. Fujii, M. Igarashi, T. Furukawa, K. Goto-Azuma, T. Saito, S. Kanamori, N. Kanamori, N. Yoshida, and R. Uemura. General tendencies of stable isotopes and major chemical constituents of the Dome Fuji deep ice core. 2003.

J. W. Weatherly. Sensitivity of Antarctic Precipitation to Sea Ice Concentrations in a General Circulation Model. *J. Climate*, 17(16):3214–3223, Aug. 2004. ISSN 0894-8755, 1520-0442. doi: 10.1175/1520-0442(2004)017¡3214:SOAPTS¿2.0.CO;2.

M. Werner, P. M. Langebroek, T. Carlsen, M. Herold, and G. Lohmann. Stable water isotopes in the ECHAM5 general circulation model: Toward high-resolution isotope modeling on a global scale. *J. Geophys. Res.*, 116(D15):D15109, Aug. 2011. ISSN 0148-0227. doi: 10.1029/2011JD015681.

T. Westerhold, N. Marwan, A. J. Drury, D. Liebrand, C. Agnini, E. Anagnostou, J. S. K. Barnet, S. M. Bohaty, D. De Vleeschouwer, F. Florindo, T. Frederichs, D. A. Hodell, A. E. Holbourn, D. Kroon, V. Lauretano, K. Littler, L. J. Lourens, M. Lyle, H. Pälike, U. Röhl, J. Tian, R. H. Wilkens, P. A. Wilson, and J. C. Zachos. An astronomically dated record of Earth's climate and its predictability over the last 66 million years. *Science*, 369(6509): 1383–1387, Sept. 2020. ISSN 0036-8075, 1095-9203. doi: 10.1126/science.aba6853.

I. M. Whillans and P. M. Grootes. Isotopic diffusion in cold snow and firn. *J. Geophys. Res.*, 90(D2):3910–3918, Apr. 1985. ISSN 0148-0227. doi: 10.1029/JD090iD02p03910.

M. Willeit, A. Ganopolski, R. Calov, and V. Brovkin. Mid-Pleistocene transition in glacial cycles explained by declining CO2 and regolith removal. *SCIENCE ADVANCES*, 2019.

E. Wolff, C. Barbante, S. Becagli, M. Bigler, C. Boutron, E. Castellano, M. De Angelis, U. Federer, H. Fischer, F. Fundel, M. Hansson, M. Hutterli, U. Jonsell, T. Karlin, P. Kaufmann, F. Lambert, G. Littot, R. Mulvaney, R. Röthlisberger, U. Ruth, M. Severi, M. Siggaard-Andersen, L. Sime, J. Steffensen, T. Stocker, R. Traversi, B. Twarloh, R. Ud-

isti, D. Wagenbach, and A. Wegner. Changes in environment over the last 800,000 years from chemical analysis of the EPICA Dome C ice core. *Quaternary Science Reviews*, 29 (1-2):285–295, Jan. 2010. ISSN 02773791. doi: 10.1016/j.quascirev.2009.06.013.

Y. Yan, M. L. Bender, E. J. Brook, H. M. Clifford, P. C. Kemeny, A. V. Kurbatov, S. Mackay, P. A. Mayewski, J. Ng, J. P. Severinghaus, and J. A. Higgins. Two-million-year-old snapshots of atmospheric gases from Antarctic ice. *Nature*, 574(7780):663–666, Oct. 2019. ISSN 0028-0836, 1476-4687. doi: 10.1038/s41586-019-1692-3.

Y. Yan, N. E. Spaulding, M. L. Bender, E. J. Brook, J. A. Higgins, A. V. Kurbatov, and P. A. Mayewski. Enhanced moisture delivery into Victoria Land, East Antarctica, during the early Last Interglacial: implications for West Antarctic Ice Sheet stability. *Clim. Past*, 17(5):1841–1855, Sept. 2021. ISSN 1814-9332. doi: 10.5194/cp-17-1841-2021.

Appendix A

DETAILS ON INTER-LABORATORY COMPARISON AND WATER ISOTOPE CORRECTION

A.1 Inter-laboratory comparison

Water-isotope data used for analyses in this thesis were produced by two different laboratories: the Climate Change Institute (CCI) at the University of Maine, and the University of Washington IsoLab (IsoLab). I conducted an inter-laboratory comparison of water-isotope data, and identified a correction to adjust the offset between the two datasets; I have applied this correction to all data produced by CCI to align all measurements to the VSMOW-SLAP scale (Schoenemann et al., 2013).

Allan Hills ice cores measured prior to the establishment of the COLDEX STC were measured for water isotopes by CCI in accordance with protocols listed here: https://zenodo.org/records/11085053. Water-isotope data included in this thesis that were generated by CCI include measurements from S27 (Spaulding et al., 2013; Yan et al., 2021), ALHIC1503 (Higgins et al., 2015; Yan et al., 2019), ALHIC1502 (Yan et al., 2019), and ALHIC1901, ALHIC1902, and ALHIC1903 (Shackleton et al., submitted; Shackleton et al., in review; Carter et al., in review).

Water-isotope data generated by the COLDEX STC have been measured by the University of Washington stable isotope laboratory (IsoLab) following methods established by Schauer et al. (2016) – e.g., for 1-cm vertically resolved measurements of ALHIC1901, ALHIC1902, and for drilling chip measurements from ALHIC1902, ALHIC2201, ALHIC2301, and ALHIC2302 – and by Davidge et al. (2022) – e.g., for the CFA campaign of ALHIC2201.

An interlaboratory comparison was warranted to ensure the validity of comparisons of these datasets. An inter-laboratory comparison was conducted in 2023-2024 using drilling chip measurements of ALHIC1902 and ALHIC2201 and internal calibration standards from both laboratories.

A.1.1 Measurement of ALHIC1902 and ALHIC2201 drilling chips and internal reference waters

All drilling chip samples were shipped frozen in WhirlPak sample bags to the University of Washington, where they were processed in a -17° C freezer. Drilling chips were transferred into sealed polyethylene bottles and thawed at room temperature, and were then transferred into duplicate bottle sets: 20-ml glass vials with conical polyvinyl inserts in the cap for shipment to CCI, and 10-ml polyethylene bottles for analysis in IsoLab. In addition, three calibration standards from IsoLab were sent to CCI (i.e., WW, SPS, and VW), and three calibration standards from CCI were sent to IsoLab (i.e., ASS, LAP, and BBB).

115 samples for ALHIC2201 were measured by IsoLab, and 112 samples from ALHIC2201 were measured by CCI; the remaining three samples broke during transport. A total of 44 samples from ALHIC1902 were measured by both labs.[1] Reference waters were measured by both labs.

A.2 Data correction

Initial observations of all data indicate a consistent calibration offset, as highlighted by Table A.2 and Figure A.1. To bring the measurements into alignment with the VSMOW-SLAP scale, we measured the trio of CCI reference waters against internal IsoLab and international reference waters. Data for CCI standards LAP, ASS, and BBB are provided in Table A.2.

Low errors in independently calibrated, repeated measurements of CCI reference waters suggest a difference between the VSMOW-SLAP-calibrated values and the assigned values of CCI reference waters. We therefore apply a correction based on these measurements to align UW and CCI results. Water-isotope data are calibrated against reference waters of known isotopic composition through a two-point linear adjustment:

$$\delta_{CCI} = \delta_{uncalibrated} \times m_{CCI} + b_{CCI} \tag{A.1}$$

[1]Note that an additional 12 samples from ALHIC1902 were measured by IsoLab, but they were not included in the interlaboratory comparison and are therefore not reported in this section.

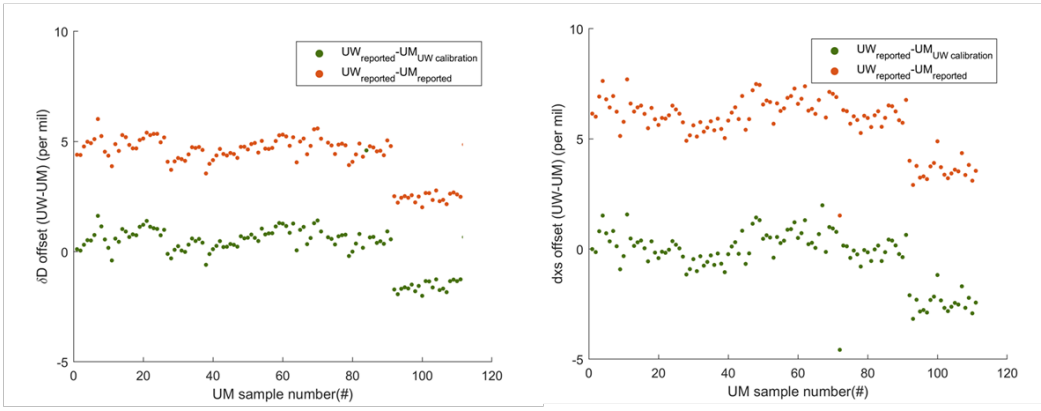

Figure A.1: CCI-Isolab water-isotope offset in ALHIC2201 drilling chips (orange). Differences are also shown after implementing an isotope correction, which is discussed in the following section (green).

Reference ID	δD (‰), CCI	δD (‰), IsoLab	δ^{18}O (‰), CCI	δ^{18}O (‰), IsoLab	d_{excess} (‰), IsoLab
LAP	-323.98	-320.22	-40.3	-40.54	4.1
ASS	-206.28	-204.28	-25.7	-25.84	2.4
BBB	-58.45	-56.34	-8.5	-8.88	14.7
SPS	-369.4	-365.01	-46.7	-46.96	10.7
WW	-271.6	-268.30	-33.5	-33.82	2.3
VW	-443.8	-439.24	-56.3	-56.61	13.7

Table A.1: Table of reference materials examined during the inter-laboratory comparison. Waters LAP, ASS, and BBB are routinely used for calibration of water-isotope measurements at CCI. SPS, WW, and VW are a subset of reference materials from IsoLab. IsoLab standards originate from South Pole snow, WAIS Divide WDC06A core meltwater, and Vostok meltwater. Note that CCI does not report d_{excess}, and it is therefore not included in this table. d_{excess} offsets between UW and CCI measurements are shown in Figure A.1.

Reference ID	mean δD (‰)	σ (‰)	mean δ^{18}O (‰)	σ (‰)	n
LAP	-319.64	0.54	-40.52	0.07	27
ASS	-204.19	0.37	-25.88	0.06	17
BBB	-56.93	0.56	-9	0.06	19

Table A.2: Mean and standard deviation for all δ^{18}O and δD measurements of CCI reference materials made in IsoLab, including data calibrated directly against IAEA and USGS standards. The number of measurements is provided in the final column.

where m_{CCI} and b_{CCI} define an analysis-specific calibration determined by the differences of uncalibrated values for LAP, ASS, and BBB and the known isotopic composition. Published δ_{CCI} data have already undergone this linear calibration, but are offset from δ_{UW} by several in δD and d_{excess} and approximately 0.3 in δ^{18}O. To "recalibrate" the published data, we determine a secondary linear adjustment to align δ_{CCI} with $\delta_{VSMOW-SLAP}$.

$$\delta_{\text{VSMOW-SLAP}} = \delta_{\text{CCI}} \times m + b \tag{A.2}$$

for either δ^{18}O or δD.

The slope and intercept ($\pm$ standard error) from all standards measured for the inter-laboratory comparison are m=0.9991$\pm$0.002 and b=-0.31$\pm$0.17 for δ^{18}O, and m=0.9925$\pm$0.002 and b=1.26$\pm$0.49 for δD. However, because the initial calibrated values of all reported δ_{CCI} data are calibrated only to LAP, ASS, and/or BBB, a linear regression of all data is biased towards m_{CCI} and b_{CCI} used for the conversion of raw to reported values and the values above are somewhat misleading. A better correction is derived from only the standards used to determine m_{CCI} and b_{CCI} for the original calibration of $\delta_{uncalibrated}$. Therefore, we provide a linear correction based only on LAP and BBB (i.e., the isotopically most negative and least negative CCI reference waters). The corrections become:

$$\delta D_{VSMOW-SLAP} = \delta D_{CCI} \times 0.9894 + 0.90 \tag{A.3}$$

and

$$\delta^{18}O_{VSMOW-SLAP} = \delta^{18}O_{CCI} \times 0.9912 - 0.57 \tag{A.4}$$

These corrections are applied to all CCI data discussed by this thesis. Additionally, we calculate d_{excess} from published data as

$$d_{excess} = \delta D_{VSMOW-SLAP} - 8 \times \delta D \tag{A.5}$$

A.3 Error estimation

Errors in the water-isotope measurement are typically estimated by determining the error of an additional reference water. However, calibration data are not available for published measurements of δ_{CCI}. Therefore, we determine the external error of δ_{CCI} as the root-mean-squared error between δ_{UW} and δ_{CCI} for all data used in the interlaboratory comparison. The correction reduces the RMSE for all isotopes, and is particularly important for δD and d_{excess}.

Measurement	**RMSE$_{UW-CCI}$ (uncorrected CCI)**	**RMSE$_{UW-CCI}$ (corrected CCI)**
δ D (‰)	5.0	1.4
δ^{18}O (‰)	0.3	0.2
d_{excess} (‰)	6.4	1.5

Updated calibration protocols at CCI reduce this error in reported values of δD since April of 2024 (see https://zenodo.org/records/11085053).

Appendix B

SUPPORTING INFORMATION FOR CHAPTER 3

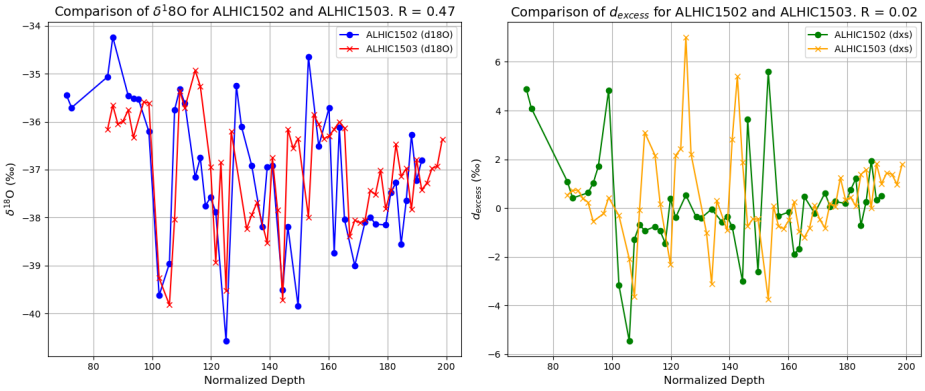

Figure B.1: Comparison of binned and averaged data from ALHIC1502 and ALHIC1503 on a normalized depth scale. Data have been aligned to maximize the correlation of δ^{18}O.

This appendix contains cross-correlated δ^{18}O and d_{excess} profiles for each correlated pair of ice cores along the flow-line transect described in Chapter 3. All profiles have been scaled and aligned by δ^{18}O. Because only the bottom 25 m of ALHIC1901 were analyzed and because ALHIC1502 was likely not drilled to the bed, there is minimal overlapping information between ALHIC1502 and ALHIC1901 and this pair is consequently not included.

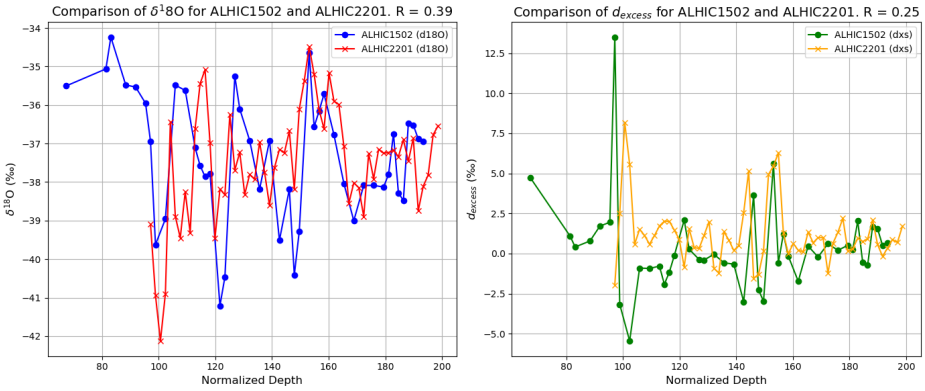

Figure B.2: Comparison of binned and averaged data from ALHIC1502 and ALHIC2201 on a normalized depth scale. Data have been aligned to maximize the correlation of δ^{18}O.

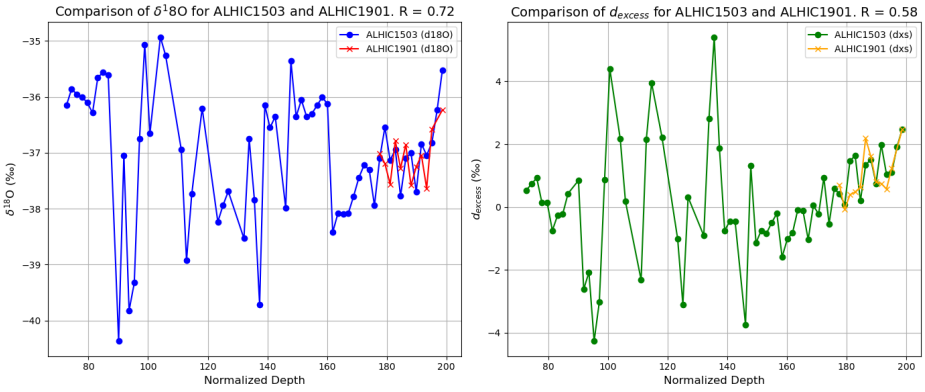

Figure B.3: Comparison of binned and averaged data from ALHIC1503 and ALHIC1901 on a normalized depth scale. Data have been aligned to maximize the correlation of δ^{18}O.

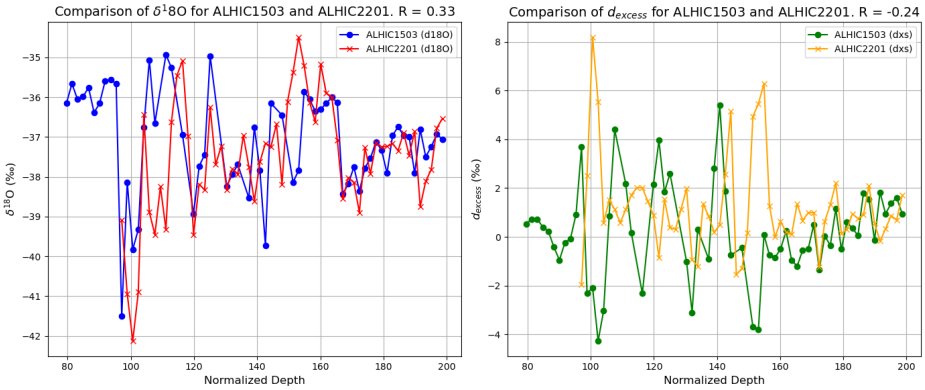

Figure B.4: Comparison of binned and averaged data from ALHIC1503 and ALHIC2201 on a normalized depth scale. Data have been aligned to maximize the correlation of δ^{18}O.

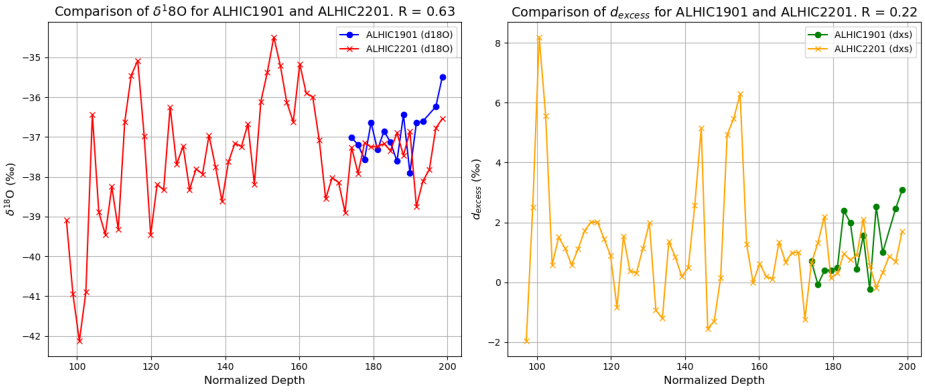

Figure B.5: Comparison of binned and averaged data from ALHIC1901 and ALHIC2201 on a normalized depth scale. Data have been aligned to maximize the correlation of δ^{18}O.

Appendix C

ISOTOPIC OBSERVATIONS OF ALLAN HILLS SURFACE SNOW

Characterizing modern surface snow in the Allan Hills is important for understanding the water-isotope system in blue ice areas. Chapter 4 suggests that the climate signal recorded in <725 ka Allan Hills ice reflects both global climate and also a linear, age-dependent change in archived Allan Hills snow. Observed differences from EDC demonstrate that Allan Hills ice is increasingly both "colder" in observed δ composition – suggesting a longer atmospheric distillation – and also more negative in d_{excess}, which is perhaps indicative of post-depositional sublimation (e.g., Hu et al., 2022). In order for both long-term trends to be sustained over >700 ky, a mechanism is required that connects these two processes for snow archived at the Allan Hills.

To examine the variability in modern snowfall, snow samples were collected over a period of two weeks during the 2022-2023 austral summer. While limited information is available about site meteorological conditions during this time, samples were categorized as "blowing snow" (collected from near the ground surface during wind events), "fresh snow" (collected from tent surfaces after precipitation events), or "ground snow" (collected from the ground in the absence of active accumulation events) (Yuzhen Yan, personal correspondence).

These samples were measured by COLDEX REU student Sara Akiba during Summer 2024 using a Picarro L2130-i and calibrated against the VSMOW-SLAP scale using internal reference waters that span the full range of isotope values. While somewhat inconclusive due to the very short study interval and limited number of samples, these observations demonstrate notable differences between wind-delivered and storm-delivered snow, both in the range of observed isotope values and in the slope of the local meteoric water line. This is consistent with a higher-plateau source for wind-blown snow, which is more distilled (i.e., more negative) than fresh snow while also exhibiting a different δ^{18}O-d_{excess} relationship, highlighting the different atmospheric pathways of these distinct types of accumulating snow.

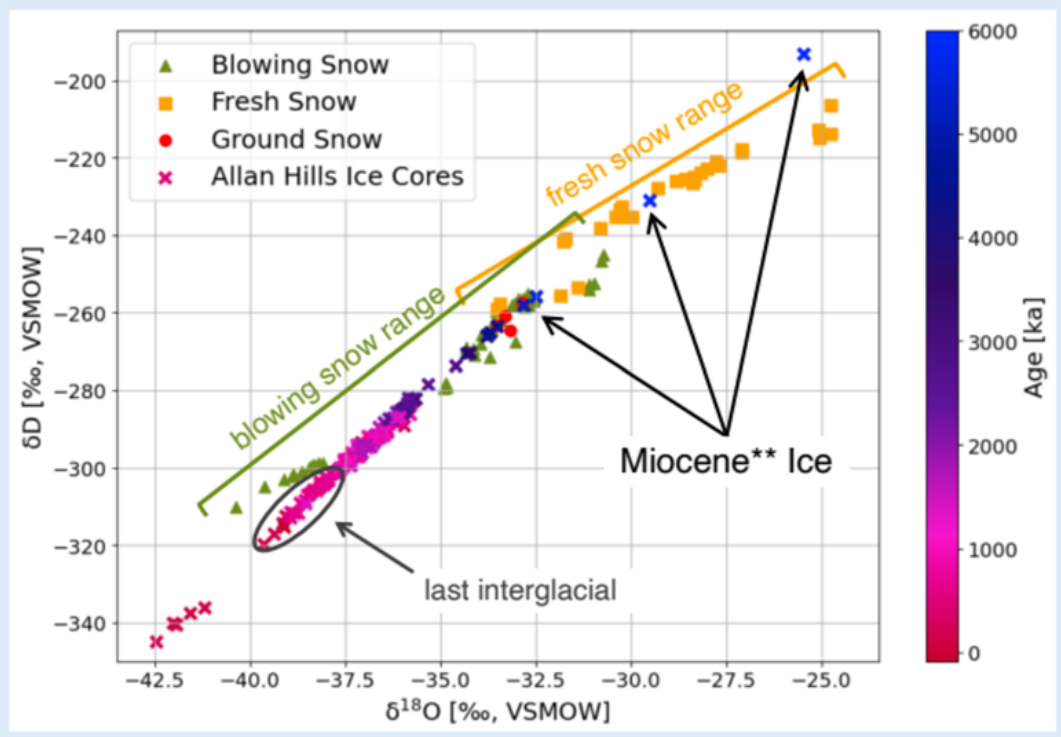

Figure C.1: Surface snow data from samples collected during the 2022-2023 austral summer, including fresh snow, blowing snow, and ground snow. Ice-core data from Shackleton et al. (submitted) are shown for context. Figure by Sara Akiba, COLDEX REU student during Summer 2024.